Species Transport Mechanisms Governing Crossover and Capacity Loss in Vanadium Redox Flow Batteries

A Thesis

Submitted to the Faculty

of

Drexel University

by

Ertan Agar

in partial fulfillment of the

requirements for the degree

of

Doctor of Philosophy

July 2014

Dedications

This thesis is dedicated to my parents, Ahmet and Gazel Agar.

Acknowledgments

First and foremost, I would like to thank my advisor, Dr. E. Caglan Kumbur for everything that he has done for me. I couldn't have asked for a better advisor for my Ph.D. study. I owe him lots of gratitude for guiding and mentoring me through all these years at Drexel.

I would also like to thank current and former members of the ECSL team, Chris, Kevin, Eric, and Reyhan. Your help and support throughout the course of this study are so important for me. I always feel privileged to work with you guys.

I am always indebted to my family: my parents, Ahmet and Gazel Agar, my brother, and sister, sister in-law, Mustafa, Mediha and Nejla Agar, for supporting me every time in my life. Without your understanding and encouragement I could not have been in this position.

I am very grateful to Dr. Michael Hickner and Dr. Dongyang Chen from Penn State, for their invaluable collaboration and guidance.

My acknowledgment would not be completed without expressing my appreciation to my friends, Utku, Reyhan, Emre, Can Sitik, Ahmet and Gozde Karacaoglu for the friendship they provided. Thank you guys for all the wonderful times we had in Philly. Without you, nothing would be so meaningful.

Table of Contents

List of Tables

List of Figures

Abstract

Species Transport Mechanisms Governing Crossover and
Capacity Loss in Vanadium Redox Flow Batteries

Ertan Agar

E. Caglan Kumbur, Ph.D., Advisor

Vanadium redox flow batteries (VRFBs) are an emerging energy storage technology that offers unique advantages for grid-scale energy storage due to their flexible design and decoupled power/energy feature. Despite their popularity, a series of technical challenges hinder their widespread implementation. Among these, capacity loss (i.e., loss of energy storage capability) due to the undesired species crossover across the membrane has been identified as the key issue limiting the longevity of these systems. This issue is primarily governed by the properties of the membrane and can be mitigated by using proper membrane architectures with desired features. Presently, identifying proper membrane architectures for VRFB systems is hampered by the lack of a fundamental understanding of the nature of species transport mechanisms and how they are related to the membrane properties and key operating conditions.

This Ph.D. study seeks to address this critical challenge by exploring the fundamental mechanisms responsible for species transport within the membrane. The overall objective of this dissertation study is to establish a fundamental understanding of the multi-ionic transport in VRFB membranes by investigating the ionic transport mechanisms responsible for crossover, and utilize this understanding to reveal the role of membrane properties and operating conditions on the capacity loss. To achieve these goals, a combined experimental and computational study was designed. An experimentally validated, 2-D, transient VRFB model that can track the vanadium

crossover and capture the related capacity loss was developed. In addition to the model, several electrochemical techniques were used to characterize different types of membrane and study the effects of various operating conditions on the species crossover. Using these computational and experimental tools, an in-depth understanding of the species transport mechanisms within the membrane and how they are related to membrane properties and operating conditions of VRFBs has been obtained. Finally, this understanding was utilized to identify effective mitigation strategies to minimize the capacity fade and improve the long-term performance of these systems.

Chapter 1. Introduction

1.1 Background

The major issue in large-scale usage of renewable energy from natural sources (i.e., solar, wind) is the availability of efficient, cost-effective energy storage systems. Recently, redox flow batteries (RFBs) have emerged as a promising energy storage technology due to their flexible design and ability to efficiently store energy. RFB is an emerging secondary battery technology that offers unique solutions for large-scale energy storage applications, enabling the widespread use of renewable energy sources. Unlike traditional batteries, the electrolytes are stored in external tanks and are circulated through a cell stack. In this cell stack, the energy conversion occurs due to electrochemical reactions between the electrode and liquid electrolyte. Two carbon electrodes and differently charged electrolyte solutions are separated by an ion-exchange membrane (Fig. 1.1). The role of the membrane is to prevent the mixing of the electrolytes while allowing for the transfer of protons between the two half-cells to maintain the electro-neutrality [1]. Once the charged electrolytes are depleted (i.e., participated in reaction), they are re-circulated back to the electrolyte tanks for recharging.

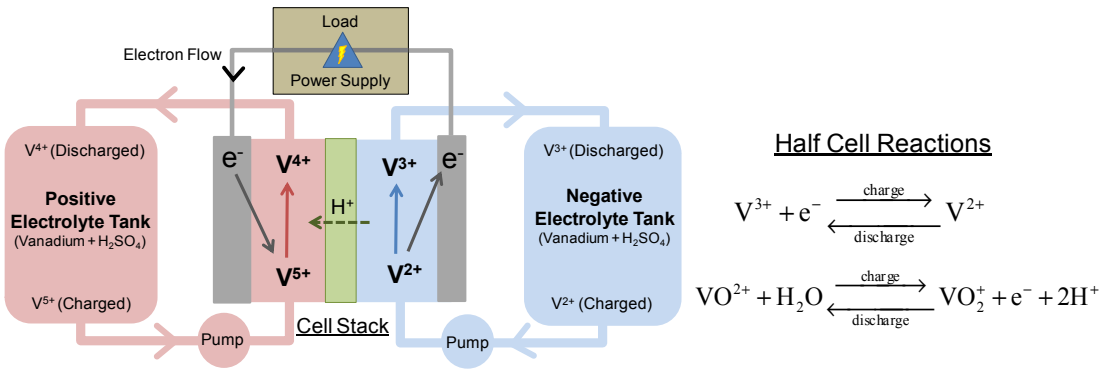

Figure 1.1 Schematic of VRFB operation and redox reactions that take place in the flow cell.

In the 1970s, NASA started research on redox flow batteries. Over the past 40 years, several redox couples have been investigated, namely: vanadium/vanadium, zinc/bromine, polysulfide/bromine, iron/chromium and cerium/zinc [2]. Several RFBs are currently available commercially including the Vanadium Redox Flow Battery (VRFB), which was invented by Skyllas-Kazacos and coworkers at University of New South Wales [3-7]. Among the different types of flow batteries, the VRFB (Fig. 1.1) distinguishes itself by employing different oxidation states of the same element, vanadium, in both half-cells. The key advantage of VRFBs is that power generation and energy storage are decoupled, such that the energy storage capacity is determined by the size of the electrolyte tanks, whereas the power rating is dictated by the size and number of redox cells [8-11]. The decoupled energy and power feature enables these systems to be scaled to different applications ranging from kW to MW scale. Utilization of the same, but differently charged, species in VRFBs eliminates most of the major problems that affect the performance and durability of other RFBs, offering a number of key advantages such as: rapid recharging, high efficiency (~85%), long cycle life (12,000+), full discharge capability and low maintenance [12-13].

1.2 Problem Description and Current Understanding

One of the major issues limiting the long-term performance of VRFBs is the undesired transport of vanadium ions through the membrane, which is known as crossover [10]. As a result of crossover, the vanadium ions from the two electrolytes, which are supposed to remain separate, come into contact with one another, resulting in side reactions which are expected to lower the output voltage, reduce the system capacity and increase operating cost [8].

In order to reduce crossover in these systems, current research has focused on synthesizing and testing different types of membrane that limit the permeability of reacting species. To date, membranes used in VRFBs are mostly selected from commercially available materials (e.g., Nafion®), which are primarily designed for different applications, such as PEM fuel cells [14-15]. Due to the difference in system chemistries, these membranes exhibit low ion selectivity, yielding high vanadium crossover and capacity loss [8]. In addition to membrane properties, key operating conditions play an important role in crossover [10]. Therefore, understanding the transport of vanadium ions in the membrane along with how it is related to the membrane properties and key operating conditions (e.g., electrolyte flow rate, and charge/discharge current) is essential to reduce the crossover and resulting capacity loss.

To date, research on VRFB membranes has centered on development of membranes that are chemically stable and perm-selective, especially to vanadium ions or alteration of commercially used membranes to minimize the crossover losses [16-19]. The most common membrane that has been subjected to investigation is Nafion® due to its high conductivity and good chemical stability [14-15]. Several surface modification or inorganic doping processes were proposed to reduce the permeability of vanadium ions [20-21]. While these modifications have been shown to be effective at reducing vanadium permeability, the major problem associated with the use of Nafion® is the cost. Studies show that the Nafion-based membranes are responsible for ~41% of the total cost of overall system [8, 22-23]. Therefore, researchers have recently started to look for alternative membranes that are inexpensive, yet show desired performance characteristics for VRFB operations. Recently, Kim et al. [8]

investigated the Radel polymer as a potential membrane candidate. The sulfonated Radel membrane (s-Radel) is shown to yield an order of magnitude lower permeability of VO^{2+} ions ($2.07\times10^{-7}cm^2/min$) as compared to Nafion® ($1.29\times10^{-6}cm^2/min$), resulting in higher efficiency and lower capacity loss [8] (Fig. 1.2). However, these membrane types show a decline in performance at around 40 cycles due to the degradation of the membrane [8,23].

Another major issue limiting the membrane studies is the conductivity-permeability trade-off. Because, increasing conductivity of the membrane results in higher crossover, which limits the long-term performance and lifetime of VRFBs. In an effort to address this issue, the transport characteristics of vanadium ions and water have been investigated by Sun et al. [10] during charge/discharge cycling and self-discharge of a VRFB. Using this framework, a mathematical model has been developed by You et al. [24] which predicts the self-discharge of a VRFB without flowing the electrolyte. Although this information is valuable when addressing VRFB cycle life and self-discharge issue, it lacks an understanding of how species transport mechanisms governing crossover affect VRFB performance.

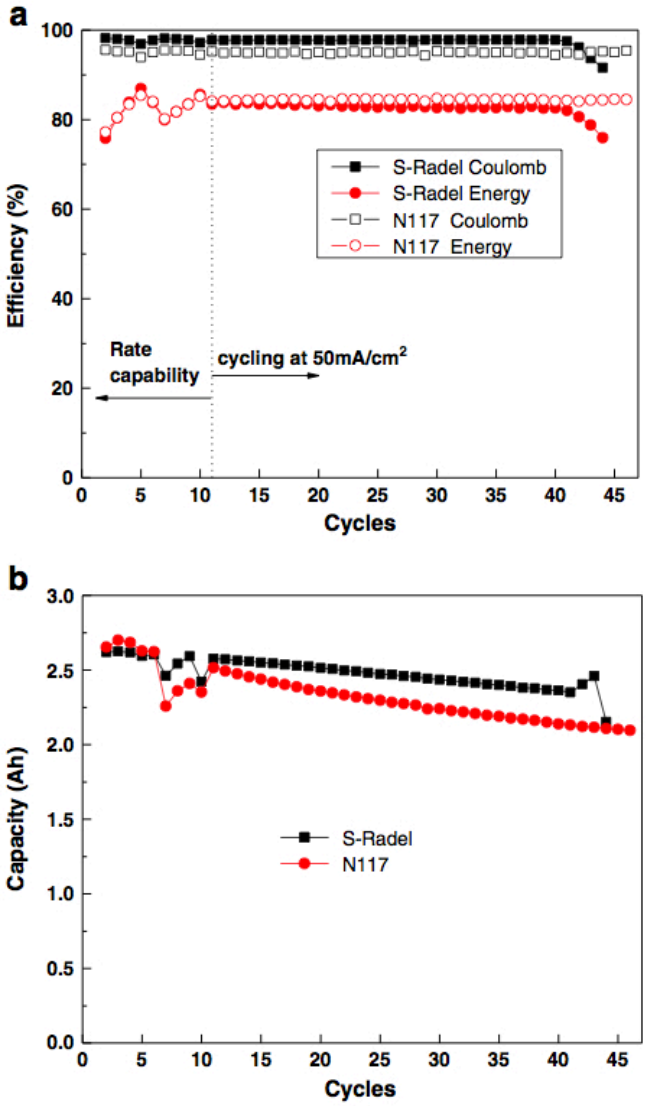

Figure 1.2 Performance comparison of VRFB with Nafion®117 and sulfonated Radel (s-Radel) membranes: a) efficiency and b) capacity [8].

Due to the lengthy time requirements of experimental studies, mathematical models have emerged recently to understand the system behavior and identify the losses in VRFBs [24-35]. A very few (less than a dozen) modeling studies have been reported so far. These models are based on the macroscopic approaches adopted from PEM fuel cell literature due to the similarity of these systems. In general, they are primarily focused on identifying the major losses in order to improve the system performance.

Although these models provide useful tools for analysis of VRFB performance, their ability to investigate the crossover phenomenon is limited. For instance, they treat the membrane as a perfectly selective membrane which allows for the transport of only hydrogen protons, ignoring the transport of vanadium ions and negatively charged species. Also, they do not account for the physics at the membrane | electrolyte interface, such as: the presence of steep gradients in species concentrations and ionic potential. These limitations result in improper treatment of species transport and poor predictions of capacity loss.

1.3 Motivation and Thesis Objective

Vanadium redox flow batteries (VRFBs) hold great promise for use in grid-scale energy storage due to their flexible design and ability to efficiently store large amounts of energy. Unlike conventional electrochemical systems (e.g., batteries, supercapacitors), VRFBs have a unique system architecture which allows them to decouple energy storage capacity from power output. Although this architecture offers a number of key advantages, one major issue that hinders the long-term performance of these systems is the loss of available capacity over time. Typically, VRFBs experience significant capacity fade during cycling due to the undesired transport of vanadium ions through the membrane (known as 'crossover'). This issue is primarily governed by properties of the membrane and can be mitigated by using proper membranes with desired features. Presently, identifying proper membrane architectures for VRFB systems is hampered by the lack of a fundamental understanding of the nature of species transport mechanisms and how they are related to the membrane properties and key operating conditions.

Despite its importance, the literature lacks a descriptive theoretical framework to better understand the nature of transport mechanisms of vanadium ions and assess their dependency on the chemical composition of the membrane and operating conditions. This Ph.D. study seeks to address this critical challenge by exploring the fundamental mechanisms responsible for species transport within the membrane. The overall objective is to establish a fundamental understanding of the multi-ionic transport in VRFB membranes by investigating the ionic transport mechanisms responsible for crossover, and utilize this understanding to reveal the role of membrane properties and operating conditions on the capacity loss. In line with this overarching goal, the specific objectives of this Ph.D. study are:

- to develop a new modeling framework that incorporates, for the first time, all species transport mechanisms governing crossover in VRFBs.
- to identify the role of membrane properties (i.e., thickness and chemical properties of the membrane) on species transport mechanisms.
- to investigate the effects of operating conditions on species transport mechanisms and related capacity loss.

To achieve the stated goals, a combined experimental and computational study was designed and performed. The details of these studies are documented in the following chapters of this thesis. Chapter 2 describes the mathematical framework of the VRFB model and presents the details of the model formulation. In Chapter 3, the experimental validation of the model along with a case study performed for Nafion® membrane is reported. Chapter 4 is devoted to the role of membrane properties (i.e., chemical structure and membrane thickness) on species crossover. The connection between the structure of the membrane and crossover is presented. Chapter 5 focuses on the effects of operating conditions on long-term performance of the VRFB. It also

documents the studies performed to identify mitigation strategies. Finally, Chapter 6 summarizes the major findings of this dissertation study along with a discussion on the future work.

Chapter 2. VRFB Model Development

As a first step of this Ph.D. study, a 2-D transient VRFB model that incorporates the transport of all species (i.e., vanadium, water, hydrogen ions and bisulfate) through the membrane was developed. This model was utilized to capture the relative contribution of each species transport mechanism (i.e., diffusion, convection, and migration) to the crossover. This chapter describes the mathematical framework of this model, along with governing equations and boundary/initial conditions.

2.1 Introduction

Among the flow battery types, the VRFB distinguishes itself by using different oxidation states of the same vanadium element in the redox reactions [36]. During charge/discharge of a VRFB, the redox reactions occur simultaneously in both half-cells as follows:

$$V^{3+} + e^{-} \underset{\text{discharge}}{\overset{\text{charge}}{\rightleftharpoons}} V^{2+} \qquad \text{(Negative)} \qquad (2.1)$$

$$VO^{2+} + H_2O \underset{\text{discharge}}{\overset{\text{charge}}{\rightleftharpoons}} VO_2^{+} + e^{-} + 2H^{+} \qquad \text{(Positive)} \qquad (2.2)$$

where VO^{2+} and VO_2^{+} represent vanadium in the V(IV) and V(V) oxidation states, respectively.

Due to the high cost and lengthy time requirements of experimental studies, performance studies have been conducted through the development of mathematical models. Only a very few (less than dozen) modeling studies [24-35] have been reported so far. In general, these models are based on the approaches adopted from

PEM fuel cell literature due to the similarity of these systems, and are primarily focused on understanding the system behavior and identifying the major losses in VRFBs. A good review of the modeling efforts is provided in [37].

The first model for VRFB systems was introduced by Li and Hikihara [25]. They developed a zero-dimensional, transient model that simulates the mechanical (pumping) and electrochemical performance of a VRFB system [25]. Soon after, Shah et al. [26] developed a transient, two-dimensional model of a single cell, which was used to predict the temporal distributions of the reactants and analyze the effects of inlet flow rates on VRFB performance. In other work by the same group, this model was expanded to include the effects of heat generation, localized temperature variations, and hydrogen/oxygen evolution [27-29]. You et al. [30] later utilized the mathematical framework developed by Shah et al. [26] to formulate a steady state model in order to predict the effects of applied current density and state-of-charge (SOC) on the performance. Vynnycky [32] proposed scaling and asymptotic methods to reduce the complexity of the model developed by Shah et al. [26] for analysis of large-scale VRFB stacks. Recently, Ma et al. [33] have utilized the same framework to develop a 3D model of a negative electrode to study the effects of electrolyte velocity on VRFB performance.

While these pioneering studies provide useful tools for rapid analysis of VRFB operation, they are based on some assumptions which may hinder their ability to predict all the physical and chemical phenomena that take place in these systems. For instance, one limitation in these models is the inaccuracy of the predicted cell voltage. A constant fitting voltage of 131 to 140 mV (~10% of the total voltage) is typically

added to the predicted voltage in order to account for unknown discrepancies with experimental data. In a recent work by Knehr et al. [38], it was suggested that this discrepancy is caused by the utilization of an incomplete version of the Nernst equation when calculating the maximum theoretical voltage – open circuit voltage (OCV) – of the system. To address this issue, a more complete version of the Nernst equation that accounts for the proton activity at the positive electrode and the Donnan potential across the membrane was proposed to provide a better means for predicting the OCV [38].

Another limiting assumption in these models is that they treat the membrane as a perfectly selective membrane which allows for the transport of only hydrogen protons; such that vanadium ions and negatively charged species are not permitted to transport through the membrane. However, in reality, the ion-exchange membranes used in these systems are not ideally perm-selective. Therefore, both negatively and positively charged species are able to transport through the membrane, which results in side reactions and capacity loss [39].

Recently, Skyllas-Kazacos and her co-workers [34-35] developed a zero-dimensional model which simulates the capacity loss of a static VRFB cell during cycling. The model was used to predict trends in capacity loss as a result of gas evolution and side reactions caused by the diffusion of vanadium through the membrane. While this model provides a useful starting point for the simulation of crossover during VRFB operation, it accounts for *only* the diffusion of vanadium ions through the membrane, and does not include the other species (e.g., water, bisulfate and hydrogen ions) and the other ion transport mechanisms (e.g., migration and convection). A good

extension of this model would be to incorporate all three mechanisms of species transport (e.g., migration, convection and diffusion), the transport of all species through the membrane, and the interfacial mass transport at the electrolyte | membrane interface, which is essential to accurately couple the species crossover in the membrane with the mass transport in the electrodes.

In order to close this critical gap in literature, in this thesis work, a 2-D, transient, isothermal model that can simulate the species crossover in the membrane is presented. The model incorporates the transport of all species (i.e., vanadium, water, hydrogen ions and bisulfate) through the membrane and accounts for the changes in the membrane potential due to the species concentrations and the semi-permselective nature of the membrane. In particular, the model incorporates all three modes of species transport across the membrane (i.e., convection, diffusion, and migration) and accounts for the transfer of water between the half-cells and the side reactions associated with the species crossover. It also utilizes a set of boundary conditions based on the conservations of flux and current at the electrolyte | membrane interfaces to account for the steep gradients in concentration and potential at these interfaces. Finally, the present model accounts for the contribution of the proton activity on the OCV at the positive electrode, which enables accurate prediction of the cell potentail without the use of a fitting voltage. In the following sections, the formulation of the model is presented along with a detailed discussion of the model capabilities and an analysis of the charge/discharge simulations performed by the model.

2.2 Method of Approach

2.2.1 Model Formulation

The present model consists of five domains, namely: the current collectors, the porous positive electrode, the porous negative electrode and the membrane (Fig. 2.1). The model is constructed based on the following assumptions:

1. All domains in the cell are considered isothermal.
2. Electrolyte flow is incompressible.
3. The mass and charge transfer properties of the electrode, electrolyte and membrane (i.e., resistivity, viscosity, diffusion coefficients, etc.) are assumed to be isotropic.
4. Hydrogen and oxygen evolution reactions are neglected.
5. The dilute solution approximation is utilized for species transport.
6. Variations in concentration, potential, and pressure in the z-direction are neglected.

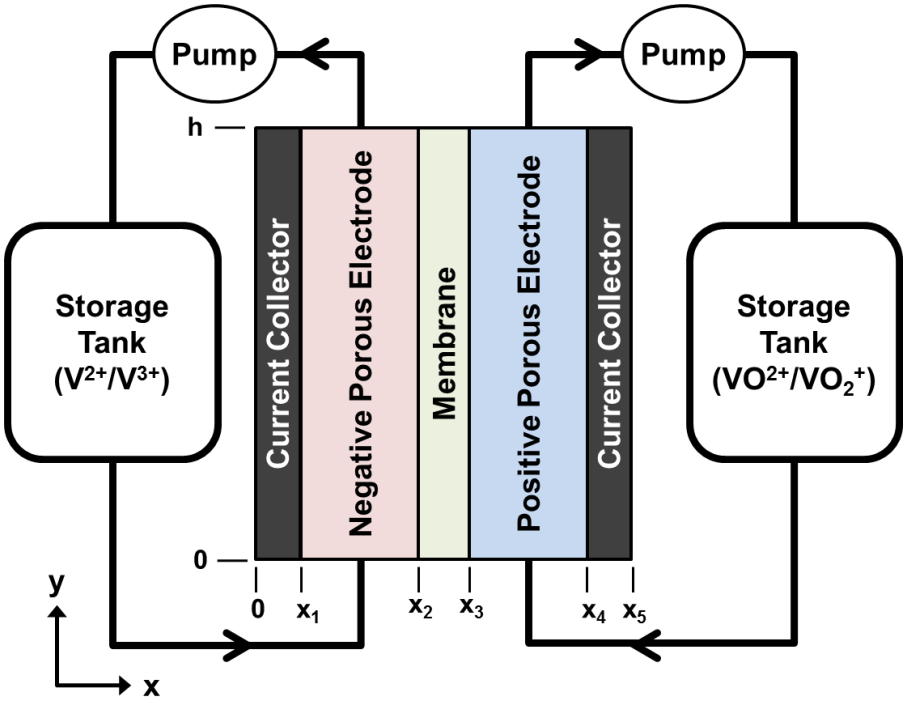

Figure 2.1 Schematic of the VRFB system and modeling domains

2.2.1.1 Porous Electrode

In each half-cell, liquid electrolytes consisting of water, sulfuric acid (i.e., H^+, HSO_4^-, and SO_4^{2-}) and charged vanadium species (i.e., V^{2+}, V^{3+}, VO^{2+}, and VO_2^+) flow through the porous carbon electrodes. The conservation of mass for each charged species is defined using the following equation:

$$\frac{\partial}{\partial t}(\varepsilon c_i^e) + \nabla \cdot \vec{N}_i^e = -S_i \tag{2.3}$$

where c_i^e is the bulk concentration of species i in the electrolyte (e), ε is the porosity of the electrode, $\vec{N}_i^e$ is the flux of the charged species in the electrolyte, and S_i denotes the source term for the species. Eq. 2.3 applies to all charged species except SO_4^{2-}, which is calculated from the condition of electroneutrality in the electrolyte as shown below:

$$\sum_i z_i c_i^e = 0 \tag{2.4}$$

where z_i is the valence for species i.

In Eq. 2.3, the source term S_i (given in Table 2.1) represents the change in concentration of species i due to the electrochemical reactions in the half-cells and the dissociation of H_2SO_4 (Eq. 2.5). It is important to note that since the electrolytes contain less than the experimentally observed limit of H_2SO_4 (40 mol kg^{-1} [26]), it is safe to assume that the first step of dissociation ($H_2SO_4 \rightarrow H^+ + HSO_4^-$) is fully complete. The second step of dissociation ($HSO_4^- \rightarrow H^+ + SO_4^{2-}$) can be described using a dissociation source term (S_d), which represents the changes in the concentrations of the species in order to maintain the correct ionic ratios, and is given as follows:

$$S_d = k_d \left(\frac{c_{H^+}^e - c_{HSO_4^-}^e}{c_{H^+}^e + c_{HSO_4^-}^e} - \beta \right) \tag{2.5}$$

where β is the degree of dissociation of HSO_4^-, which is determined experimentally [40] and is assumed to be constant in this study. The term k_d represents the dissociation reaction coefficient, which is used as a fitting parameter to model instantaneous dissociation of the acid.

Table 2.1 Mass, dissociation, and reaction source terms

Term	Description	Positive electrode	Negative electrode
S_{II}	V(II) concentration equation (mol m^{-3})	---	i/F
S_{III}	V(III) concentration equation (mol m^{-3})	---	$-i/F$
S_{IV}	V(IV) concentration equation (mol m^{-3})	i/F	---
S_{V}	V(V) concentration equation (mol m^{-3})	$-i/F$	---
S_{H^+}	Proton concentration equation (mol m^{-3})	$-S_d$	$-2i/F-S_d$
$S_{HSO_4^-}$	Bisulfate concentration equation (mol m^{-3})	S_d	S_d
S_m	Velocity continuity equation (kg m^{-3} s^{-1})	$\frac{i \cdot M_w}{F \cdot w_{cell}}$	0

The flux of each species in Eq. 2.3 is defined by the Nernst-Planck equation, which determines species movement due to diffusion, migration, and convection:

$$\vec{N}_i^e = -D_i^{eff}\nabla c_i^e - z_i u_i^e c_i^e F\nabla\phi_l^e + \vec{v}_j c_i^e \tag{2.6}$$

where ϕ_l^e is the ionic (liquid) potential, μ_i^e is the ionic mobility and $\vec{v}_j$ is the velocity of the electrolyte *j*. The term D_i^{eff} represents the effective diffusion coefficient, which is calculated using the Bruggemann correlation (Eq. 2.7).

$$D_i^{eff} = \varepsilon^{3/2} D_i \tag{2.7}$$

Under the dilute solution approximation, the ionic mobility in the electrolyte, u_i^e (see Eq. 2.6) is represented using the Nernst-Einstein equation, which is given as follows [41]:

$$u_i^e = \frac{D_i^{eff}}{RT} \tag{2.8}$$

where R is the universal gas constant and T is temperature.

The bulk velocity ($\vec{v}_j$) can be determined using the following continuity equation:

$$\nabla \cdot \left(\rho_j \vec{v}_j\right) = S_{m,j} \tag{2.9}$$

where ρ_j is the density of electrolyte j. The term $S_{m,j}$ represents the mass source term which describes the generation or depletion of water in the cell due to the electrochemical reactions and is given in Table 2.1. To account for variations in electrolyte volume, water is treated as a volume instead of a concentrated species in the model formulation. The velocity term ($\vec{v}_j$) in Eq. 2.9 is calculated using the Darcy's law:

$$\vec{v}_j = -\frac{\kappa}{\mu_j} \nabla p_j \tag{2.10}$$

where, μ_j is the dynamic viscosity of the electrolyte, p_j is the pressure, and κ is the effective permeability of the electrode, which is determined using the Kozeny-Carman equation:

$$\kappa = \frac{4r_p^2}{C_{KC}} \frac{\varepsilon^3}{\left(1-\varepsilon\right)^2} \tag{2.11}$$

The term r_p in Eq. 2.11 represents the mean radius of the electrode pores, and C_{KC} is the Kozeny-Carman constant [42]. Due to the lack of data regarding the electrolyte viscosity of a VRFB, a constant value of μ_j is used for each electrolyte, which

represents the viscosity of the electrolyte at 50% state of charge (SOC) [43]. The values of μ_j and the other electrolyte properties are listed in Table 2.2.

Table 2.2 Electrolyte properties and parameters

Symbol	Description	Value
k_d	HSO_4^- dissociation reaction rate constant (s^{-1})[a]	1 x 10^4
β	HSO_4^- degree of dissociation	0.25 [40]
μ_-	Average dynamic viscosity of negative electrolyte (Pa s)	0.001 [43]
μ_+	Average dynamic viscosity of positive electrolyte (Pa s)	0.0035 [43]
ρ_-	Average density of negative electrolyte (kg m^{-3})	1300 [43]
ρ_+	Average density of positive electrolyte (kg m^{-3})	1350 [44]
ρ_w	Density of water (kg m^{-3})	999 [45]
D_{II}	V(II) diffusion coefficient (m^2 s^{-1})	2.4 x 10^{-9} [46]
D_{III}	V(III) diffusion coefficient (m^2 s^{-1})	2.4 x 10^{-10} [46]
D_{IV}	V(IV) diffusion coefficient (m^2 s^{-1})	3.9 x 10^{-10} [46]
D_V	V(V) diffusion coefficient (m^2 s^{-1})	3..9 x 10^{-10} [46]
D_{H^+}	H^+ diffusion coefficient (m^2 s^{-1})	9.312 x 10^{-9} [48]
$D_{HSO_4^-}$	HSO_4^- diffusion coefficient (m^2 s^{-1})	1.33 x 10^{-9} [48]
$D_{SO_4^{2-}}$	SO_4^{2-} diffusion coefficient (m^2 s^{-1})	1.065 x 10^{-9} [48]

[a]Fitted parameter

The species transport, electrochemical reactions, and current in the electrode domain are coupled through the conservation of charge:

$$\nabla \cdot \vec{j}_l^{\,e} = -\nabla \cdot \vec{j}_s^{\,e} = i \tag{2.12}$$

where i is the reaction current density. $\vec{j}_l^{\,e}$ and $\vec{j}_s^{\,e}$ denote the liquid (ionic) and solid (electronic) current density in the electrode domain, respectively, and are given as follows:

$$\vec{j}_l^{\,e} = F\sum_i z_i \vec{N}_i^{\,e} \tag{2.13a}$$

$$\vec{j}_s^{\,e} = \sigma_s^e \nabla \phi_s^e \tag{2.13b}$$

where σ_s^e is the bulk conductivity of the electrode, and its value is given in Table 2.3 along with the other properties of the electrodes and current collectors.

The local reaction current density (i) is expressed by the Butler-Volmer equations, which are given in Eq. 2.14 for both the negative ('-') and positive ('+') electrodes.

$$i_- = aFk_-\left(c_{II}^e\right)^{(1-\alpha_-)}\left(c_{III}^e\right)^{\alpha_-}\left[\left(\frac{c_{II}^s}{c_{II}^e}\right)\exp\left(\frac{(1-\alpha_-)F\eta_-}{RT}\right)-\left(\frac{c_{III}^s}{c_{III}^e}\right)\exp\left(\frac{-\alpha_- F\eta_-}{RT}\right)\right] \tag{2.14a}$$

$$i_+ = aFk_+\left(c_{IV}^e\right)^{(1-\alpha_+)}\left(c_V^e\right)^{\alpha_+}\left[\left(\frac{c_{IV}^s}{c_{IV}^e}\right)\exp\left(\frac{(1-\alpha_+)F\eta_+}{RT}\right)-\left(\frac{c_V^s}{c_V^e}\right)\exp\left(\frac{-\alpha_+ F\eta_+}{RT}\right)\right] \tag{2.14b}$$

In Eq. 2.14, k represents the reaction rate constant, and α denotes the charge transfer coefficient. The term a is the specific surface area of the porous electrode, whereas η represents the overpotential and is defined as follows:

$$\eta_j = \phi_l - \phi_s - E_{0,j} \tag{2.15}$$

where $E_{0,j}$ represents the open circuit voltage (OCV) of each half-cell calculated using the Nernst equations given as follows:

$$E_{0,-} = E'_{0,-} + \frac{RT}{F}\ln\left(\frac{c^e_{III}}{c^e_{II}}\right) \qquad \text{(Negative)} \qquad (2.16a)$$

$$E_{0,+} = E'_{0,+} + \frac{RT}{F}\ln\left(\frac{c^e_{V}\cdot\left(c^e_{+,H^+}\right)^2}{c^e_{IV}}\right) \qquad \text{(Positive)} \qquad (2.16b)$$

Table 2.3 Electrode and current collector properties

Symbol	Description	Value
ε	Electrode porosity[a]	0.93
r_p	Mean pore radius (μm)[a]	50.3
a	Specific surface area (m^{-1})[a]	3.5×10^4
C_{KC}	Kozeny-Carmen Coefficient	180 [42]
h_{cell}	Electrode height (m)	0.035
w_{cell}	Electrode width (m)	0.0285
L^e	Electrode thickness (m)	0.004
L^{cc}	Current collector thickness (m)	0.06
σ_s^e	Electronic conductivity of electrode (S m^{-1})[b]	66.7
σ_s^{cc}	Electronic conductivity of current collector (S m^{-1})[c]	1000

[a]Experimentally determined (Section 2.2.2.2)
[b]Supplied by Manufacturer (SGL Carbon Group, Germany)
[c]Estimated

In Eq. 2.16, $E'_{0,-}$ and $E'_{0,+}$ represent the standard reduction potentials for the negative and positive electrodes, respectively. In the presence of an electric field, like the Galvani potentials of a VRFB, ionic bonds become stretched and weakened, leading to an increase in the dissociation of the ions. Therefore, when determining c^e_{+,H^+} in Eq. 2.16b, all protons initially bonded to SO_4^{2-} are assumed to be fully dissociated, existing as free protons [38]. The input parameters describing the reaction kinetics in Eqs. 2.14-16 are listed in Table 2.4.

Table 2.4 Kinetic parameters

Symbol	Description	Value
k_-	Reaction rate constant for negative reaction (m s^{-1})[a]	7.0 x 10^{-8}
k_+	Reaction rate constant for positive reaction (m s^{-1})[a]	2.5 x 10^{-8}
α_-	Negative charge transfer coefficient[a]	0.45
α_+	Positive charge transfer coefficient[a]	0.55
$E'_{0,-}$	Standard reduction potential at negative electrode (V)	-0.255 [27]
$E'_{0,+}$	Standard reduction potential at positive electrode (V)	1.004 [27]

[a]Fitted

In the Bulter-Volmer equations (Eq. 2.14), c_i^s denotes the surface concentration of species *i* at the liquid-solid interface of the electrode. For the negative half-cell, these concentrations are determined by solving for c_{II}^s and c_{III}^s in the following equations [29]:

$$FD_{II}\left(\frac{c_{II}^{e}-c_{II}^{s}}{r_p}\right)=Fk_{\_}\left(c_{II}^{e}\right)^{(1-\alpha_{\_})}\left(c_{III}^{e}\right)^{\alpha_{\_}}\left[\left(\frac{c_{II}^{s}}{c_{II}^{e}}\right)\exp\left(\frac{(1-\alpha_{\_})F\eta_{\_}}{RT}\right)-\left(\frac{c_{III}^{s}}{c_{III}^{e}}\right)\exp\left(\frac{-\alpha_{\_}F\eta_{\_}}{RT}\right)\right] \quad (2.17a)$$

$$FD_{III}\left(\frac{c_{III}^{e}-c_{III}^{s}}{r_p}\right)=Fk_{\_}\left(c_{II}^{e}\right)^{(1-\alpha_{\_})}\left(c_{III}^{e}\right)^{\alpha_{\_}}\left[\left(\frac{c_{III}^{s}}{c_{III}^{e}}\right)\exp\left(\frac{-\alpha_{\_}F\eta_{\_}}{RT}\right)-\left(\frac{c_{II}^{s}}{c_{II}^{e}}\right)\exp\left(\frac{(1-\alpha_{\_})F\eta_{\_}}{RT}\right)\right] \quad (2.17b)$$

where r_p (the mean pore radius of the electrode) represents the average diffusive path-length. In the positive half-cell, c_{IV}^{s} and c_{V}^{s} can be determined by developing a similar system of equations using Eq. 2.14b. For brevity, these equations are not included in this paper, but a detailed description of this formulation can be found in [26-29].

2.2.1.2 Current Collector

The current collectors are composed of impermeable solid graphite. Therefore, all current within this domain is electronic and governed by Ohm's law:

$$\vec{j}_s^{cc} = -\sigma_s^{cc}\nabla\phi_s^{cc} \quad (2.18)$$

where σ_s^{cc} is the conductivity of the current collector.

2.2.1.3 Membrane

Unlike previous models, the present model accounts for the transport of all charged species through the membrane, including: V^{2+}, V^{3+}, VO^{2+}, VO_2^{+}, H^{+}, and HSO_4^{-}. Each of the positive species (i.e., vanadium and protons) satisfies the following mass balance:

$$\frac{\partial c_i^m}{\partial t} = -\nabla \cdot \vec{N}_i^m \tag{2.19}$$

where c_i^m represents the concentration of species *i* in the membrane (*m*), and the flux, $\vec{N}_i^m$, is defined using the Nernst-Planck equation (Eq. 2.6). The concentration of the bisulfate, HSO_4^-, is calculated from the condition of electroneutrality in the membrane as shown below:

$$z_f c_f + \sum_i z_i c_i^m = 0 \tag{2.20}$$

where z_f and c_f represent the charge and concentration of the fixed sulfonic acid groups that are present in the ion-exchange membrane (e.g., Nafion®), respectively. It is important to note that SO_4^{2-} is not present in the membrane because it is assumed that the dissociation of HSO_4^- is completely suppressed by the presence of the fixed charge in the membrane [47].

For the Nernst-Planck equation (Eq. 2.6) in the membrane, the velocity ($\vec{v}^m$) is given by an alternate form of Schlogl's equation [39]:

$$\vec{v}^m = -\frac{\kappa_p}{\mu_w}\nabla p - \frac{\kappa_\phi}{\mu_w} c_f F\left(\nabla \phi_l^m + \nabla \phi_{diff}^m\right) \tag{2.21}$$

where μ_w is the viscosity of water, κ_ϕ is the electrokinetic permeability and κ_p is the hydraulic permeability. The first term represents the osmosis of water through the membrane as a result of pressure differences between the half-cells. The second term represents the electro-osmotic convection caused by the viscous interactions between the fluid and the mobile ions, where $F\left(\nabla \phi_l^m + \nabla \phi_{diff}^m\right)$ represents the body force acting on the mobile ions. The term $\nabla \phi_l^m$ accounts for the liquid potential difference across

the membrane, and $\nabla\phi_{diff}^{m}$ is the effective diffusion potential, which accounts for the viscous drag as a result of ion diffusion and is calculated as follows [48]:

$$\nabla\phi_{diff}^{m} = \frac{F\sum z_i D_i^m \nabla c_i^m}{\sigma_{eff}^{m}} \tag{2.22}$$

where σ_{eff}^{m} is the effective conductivity of the membrane:

$$\sigma_{eff}^{m} = \frac{F^2}{RT}\sum_i z_i^2 D_i^m c_i^m \tag{2.23}$$

In the membrane, only ionic current exists ($\nabla\vec{j}_l = 0$) and similar to the porous electrode, it is proportional to the flux of all the species and is calculated using Eq. 2.13a $\left(\vec{j}_l^{\,m} = F\sum_i z_i \vec{N}_i^{\,m}\right)$. The properties used for the membrane are provided in Table 2.5.

Table 2.5 Membrane properties and parameters

Symbol	Description	Value
L^m	Membrane thickness (μm)	203 [49]
c_f	Fixed acid concentration (mol m^{-3})	1990 [49]
z_f	Fixed acid charge	-1
κ_ϕ	Electrokinetic permeability (m^2)[a]	1.13 x 10^{-20}
κ_p	Hydraulic permeability (m^2)	1.58 x 10^{-18} [50]
K_ϕ	Interfacial potential fitting parameter[a]	0.25
D_{II}^m	V(II) membrane diffusion coefficient (m^2 s^{-1})[a]	3.125 x 10^{-12}
D_{III}^m	V(III) membrane diffusion coefficient (m^2 s^{-1})	5.93 x 10^{-12} [51]
D_{IV}^m	V(IV) membrane diffusion coefficient (m^2 s^{-1})	5.0 x 10^{-12} [51]
D_V^m	V(V) membrane diffusion coefficient (m^2 s^{-1})	1.17 x 10^{-12} [51]
$D_{H^+}^m$	H^+ membrane diffusion coefficient (m^2 s^{-1})	3.35 x 10^{-9} [47]
$D_{HSO_4^-}^m$	HSO_4^- membrane diffusion coefficient (m^2 s^{-1})	4 x 10^{-11} [52]

[a]Fitted parameter

2.2.1.4 Membrane | Electrolyte Interface

At the membrane | electrolyte interface, current and species flux are continuous; however, the potential and species concentrations are discontinuous due to the perm-selective nature of the membrane [39]. In order to simulate this interfacial region and

account for these discontinuities, the membrane | electrolyte interface is modeled as a region with finite thickness. A set of boundary conditions have been developed to describe the mass transport at the interface, and the derivation of these equations is explained below.

The membrane | electrolyte interface is composed of a membrane region with a thickness of δ^m and an electrolyte region with a thickness of δ^e (Fig. 2.2). When compared, the membrane | electrolyte interface in a VRFB resembles the interface that can be seen at the surface of a flow-by electrode, where a flow-by electrode is defined as an electrode with a liquid electrolyte flowing over its surface (e.g., those found in electrochemical cells where the liquid is displaced due to stirring or pumping, e.g., a rotating disc electrode). Therefore, it is reasonable to assume that δ^e is equivalent to the diffusion boundary layer that exists at the surface of a flow-by electrode, where the thickness of this layer can be calculated as follows:

$$\delta^e = \delta_{momentum}\left(\frac{D_{avg}^{eff}\rho_j}{\mu_j}\right)^{1/3} \tag{2.24}$$

In Eq. 2.24, D_{avg}^{eff} represents the average effective diffusion coefficient of the species, and $\delta_{momentum}$ is the thickness of the hydrodynamic momentum boundary layer (Fig. 2.2), which is the zone next to the electrode where the velocity changes from zero to the bulk velocity. The value of $\delta_{momentum}$ can be determined for a fully developed laminar flow through a porous media (in this case, the electrode) in contact with a flat plate (in this case, rigid polymer membrane) as follows [53]:

$$\delta_{momentum} = \sqrt{\frac{\kappa}{\varepsilon}} \tag{2.25}$$

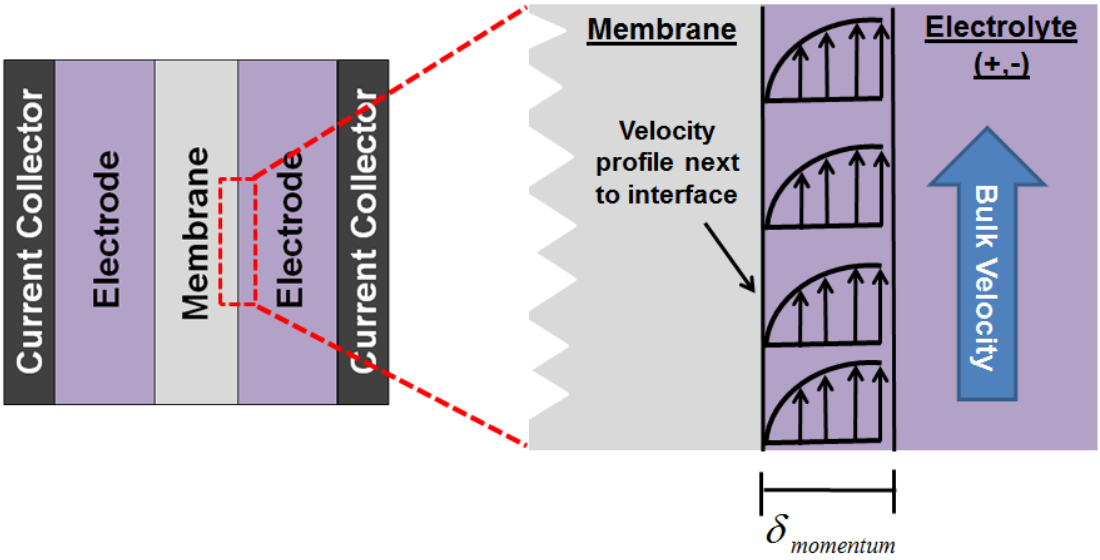

Figure 2.2 Schematic of the momentum boundary layer at the membrane | electrolyte interface under no slip conditions for laminar flow. $(\delta_{momentrum} \approx 100\mu m)$

In terms of the thickness of the membrane region at the interface (δ^m), there is no established theoretical method for calculating δ^m. In the present model, we assume that δ^m is equivalent to δ^e for simplicity. Since δ^e is typically less than 1% of the membrane thickness (~200 μm), it is reasonable to assume linear variations in concentration and potential over these small regions. Furthermore, because the steep concentration and potential gradients at the interface cause large diffusion and migration fluxes, the contribution of convection to the total species flux can be assumed negligible. Using these two assumptions, one can determine the flux of each species in the electrolyte (δ^e) and membrane (δ^m) regions at the membranelelectrolyte interface by discretizing the diffusion and migration terms in the Nernst-Plank equation (Eq. 2.6) as follows:

$$N_i^{er} = -D_i^{eff} \frac{\left(c_i^e - c_i^{junc}\right)}{\delta^e} - z_i u_i^e F \frac{\left(c_i^e + c_i^{junc}\right)}{2} \frac{K_\phi \left(\phi_l^e - \phi_l^m\right)}{\delta^e} \tag{2.26a}$$

$$N_i^{mr} = -D_i^m \frac{\left(c_i^{junc} - c_i^m\right)}{\delta^m} - z_i u_i^m F \frac{\left(c_i^{junc} + c_i^m\right)}{2} \frac{\left(1 - K_\phi\right)\left(\phi_l^e - \phi_l^m\right)}{\delta^m} \tag{2.26b}$$

where N_i^{er} and N_i^{mr} are the fluxes of species *i* in the electrolyte interface region and membrane interface region, respectively. The term c_i^{junc} represents the concentration of species *i* at the membrane | electrolyte junction (Fig. 2.3a), and K_ϕ is a fitting parameter that represents the percentage of the total potential jump $\left(\phi_l^e - \phi_l^m\right)$ occurring in the electrolyte interface region (Fig. 2.3c).

The concentration of each species at the membranelelectrolyte interface (c_i^{junc}) can be calculated by setting the fluxes at the interface equal ($N_i^{er} = N_i^{mr}$) and solving for c_i^{junc}. This procedure is valid for all membrane species except HSO_4^-, which is assumed to be discontinuous at the junction due to the fixed charge in the membrane. In order for the electrolyte and membrane regions to remain electrically neutral, the HSO_4^- concentration at the junction must satisfy the following condition of electroneutrality (Fig. 2. 3b):

$$c_{HSO_4^-}^{junc,m} = c_{HSO_4^-}^{junc,e} - c_f \tag{2.27}$$

The concentration of the bisulfate at the electrolyte side of the interface ($c_{HSO_4^-}^{junc,e}$) can be calculated by *i)* replacing the term c_i^{junc} in Eqs. 2.26a and 2.26b with $c_{HSO_4^-}^{junc,e}$ and

($c_{HSO_4^-}^{junc,e} - c_f$), respectively, *ii)* setting the fluxes at the interface equal ($N_{HSO_4^-}^{er} = N_{HSO_4^-}^{mr}$), and *iii)* solving for $c_{HSO_4^-}^{junc,e}$.

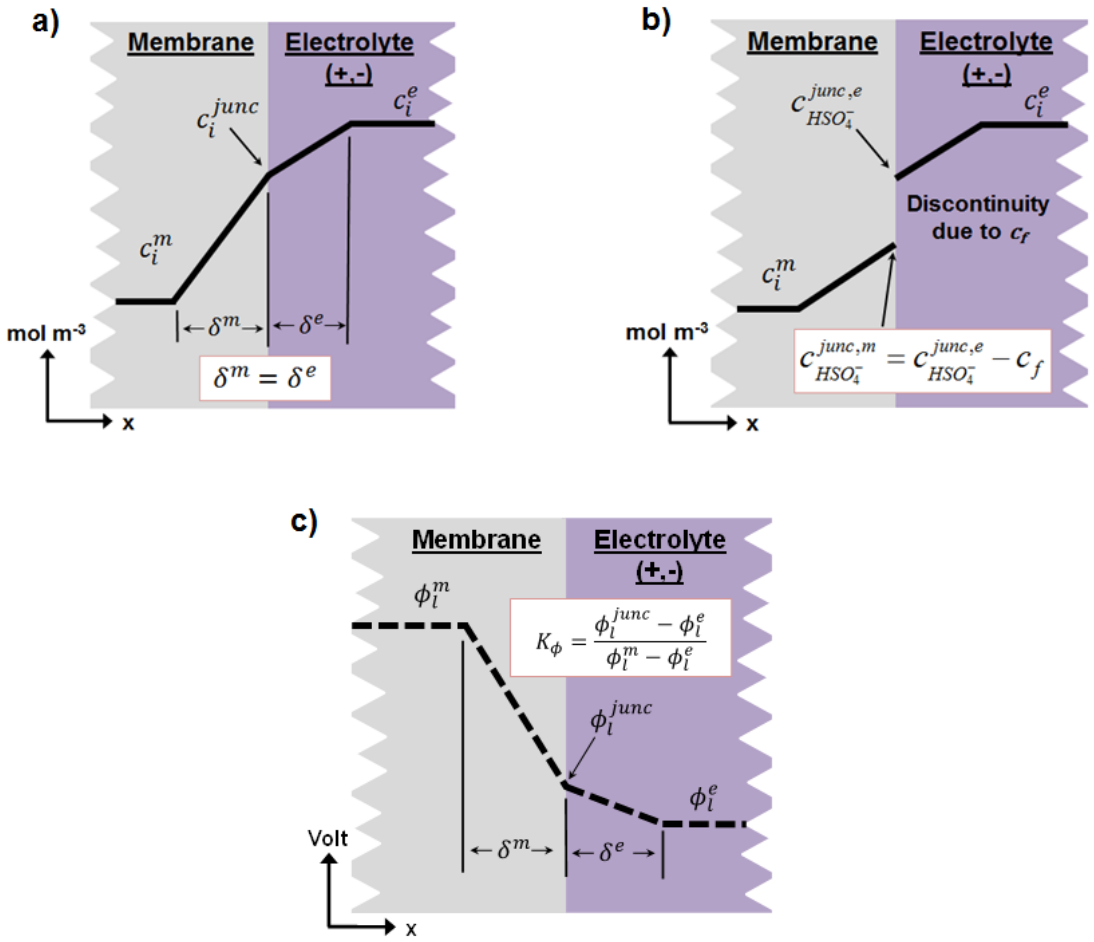

Figure 2.3 Schematic of the a) generalized species concentration distribution, b) HSO_4^- concentration distribution and c) potential distribution at the electrolyte | membrane interface, which illustrates the concept of an electrolyte and membrane interfacial region. $(\delta^e = \delta^m \approx 1\mu m)$

Using the equations developed for the species flux, the membrane interfacial region can be incorporated into the model by applying the following boundary condition on the charged species at the membranelelectrolyte interface:

$$-\vec{n} \cdot \vec{N}_i^m = -N_i^{mr} \quad \text{at } x = x_2 \text{ and } x = x_3 \tag{2.28}$$

where $\vec{n}$ denotes the outward normal unit vector and x_2 and x_3 refer to the membranelelectrolyte interface at the '-' and '+' half-cells, respectively (see Fig. 2.1). At the electrolyte interfacial region, the side reactions due to crossover must be incorporated into the boundary conditions. It is reported that the vanadium crossover through the membrane will result in the following side reactions in the electrolytes [10]:

Negative electrolyte:

$$VO^{2+} + V^{2+} + 2H^{+} \rightarrow 2V^{3+} + H_2O \tag{2.29a}$$

$$VO_2^{+} + 2V^{2+} + 4H^{+} \rightarrow 3V^{3+} + 2H_2O \tag{2.29b}$$

Positive electrolyte:

$$V^{2+} + 2VO_2^{+} + 2H^{+} \rightarrow 3VO^{2+} + H_2O \tag{2.30a}$$

$$V^{3+} + VO_2^{+} \rightarrow 2VO^{2+} \tag{2.30b}$$

These reactions were observed during a self-discharge study with no net current exchange between the graphite felt electrodes and electrolyte. Therefore, it is safe to assume that these reactions are chemical in nature (as opposed to electrochemical) and are not hindered by the slow kinetics of the un-catalyzed graphite felt. Moreover, assuming that the rate of the chemical reactions is much quicker than the species flux and all side reactions instantaneously occur upon entrance into the electrolyte region, the flux of the vanadium and hydrogen species at the electrolyte interfacial region can be represented by the following boundary conditions:

Negative membranelelectrolyte interface (x = x_2, see Fig. 2.1):

$$-\vec{n}\cdot\vec{N}^{e}_{H^+} = N^{er}_{H^+} - 2N^{er}_{IV} - 4N^{er}_{V} \tag{2.31a}$$

$$-\vec{n}\cdot\vec{N}^{e}_{II} = N^{er}_{II} - N^{er}_{IV} - 2N^{er}_{V} \tag{2.31b}$$

$$-\vec{n}\cdot\vec{N}^{e}_{III} = N^{er}_{III} + 2N^{er}_{IV} + 3N^{er}_{V} \tag{2.31c}$$

Positive membranelelectrolyte interface (x = x_3, see Fig. 2.1):

$$-\vec{n}\cdot\vec{N}^{e}_{H^+} = N^{er}_{H^+} - 2N^{er}_{II} \tag{2.32a}$$

$$-\vec{n}\cdot\vec{N}^{e}_{IV} = N^{er}_{IV} + 3N^{er}_{II} + 2N^{er}_{III} \tag{2.32b}$$

$$-\vec{n}\cdot\vec{N}^{e}_{V} = N^{er}_{V} - 2N^{er}_{II} - N^{er}_{III} \tag{2.32c}$$

Both interfaces (x = x_2 and x = x_3, see Fig. 2.1):

$$-\vec{n}\cdot\vec{N}^{e}_{HSO_4^-} = N^{er}_{HSO_4^-} \tag{2.33}$$

A case study has been performed to compare and validate the concentration and potential jumps predicted at the membranelelectrolyte interface and can be found in Section 3.1.1.1.

2.2.1.5 Boundary Conditions

In the following section, the locations of the boundary conditions are specified in accordance to the *x* and *y* coordinates shown in Fig. 2.1. At the electrode | current collector interface ($x = x_1$ and $x = x_4$) and along the top (y = h_{cell}) and bottom (y = 0) of the membrane, zero species flux conditions are assumed.

$$0 = \begin{cases} -\vec{n} \cdot \vec{N}_i^e & x = x_2 \quad \text{and} \quad x = x_3 \\ -\vec{n} \cdot \vec{N}_i^m & y = 0 \quad \text{and} \quad y = h_{cell} \end{cases} \tag{2.34}$$

At the inlets at the bottom of the electrode domains (y = 0), the inward flux of the species can be determined from the velocity of the electrolyte and the concentrations of the species:

$$\left.\begin{aligned} -\vec{n} \cdot \vec{v} &= \frac{\omega}{\varepsilon w_{cell} L_e} \\ c_i^e &= c_i^{in}(t) \end{aligned}\right\} \quad y = 0 \text{ (inlets)} \tag{2.35}$$

where w_{cell} is the cell width, L_e is the thickness of the electrode, and ω is the volumetric flow rate. At the outlets at the top of the electrode domains (y = h_{cell}), the pressure is set constant, and the diffusion driven flux of the species is assumed to be zero:

$$\left.\begin{aligned} p &= p_{out} \\ -\vec{n} \cdot D_i^{eff} \nabla c_i^e &= 0 \end{aligned}\right\} \quad y = h_{cell} \text{ (outlet)} \tag{2.36}$$

At the membrane|electrolyte interface ($x = x_2$ and $x = x_3$, see Fig. 2.1), the water transfer between the half-cells is incorporated by setting the pressure in the membrane equal to the pressure in the electrode. In addition, the "inlet" velocity into the electrode is taken as equal to the sum of the membrane velocity and the flux of water associated with the crossover side reactions (see Eqs. 2.29 and 2.30):

$$p^m = p^e \quad x = x_2 \text{ and } x = x_3 \tag{2.37a}$$

$$-\vec{n}\cdot\vec{v}_j^{\,e}=\begin{cases}\vec{n}\cdot\vec{v}^{\,m}+\dfrac{M_w}{\rho_w}\left(N_{IV}^{er}+2N_V^{er}\right) & x=x_2\\ \vec{n}\cdot\vec{v}^{\,m}+\dfrac{M_w}{\rho_w}N_{II}^{er} & x=x_3\end{cases} \tag{2.37b}$$

Constant pressure is maintained at the electrode|current collector interfaces in the electrode domain ($x=x_1$ and $x=x_4$, see Fig. 2.1), which creates a no-slip boundary condition for the velocity:

$$-\vec{n}\cdot\nabla p=0 \quad x=x_1 \text{ and } x=x_4 \tag{2.38}$$

The cell is simulated under constant current density, and the following boundary conditions are applied to the current collectors ($x=0$ and $x=x_5$, see Fig. 2.1) during charging:

$$-\vec{n}\cdot\vec{j}_s^{\,cc}=\begin{cases}-\dfrac{I}{h_{cell}w_{cell}} & x=0\\ \dfrac{I}{h_{cell}w_{cell}} & x=x_5\end{cases} \tag{2.39}$$

where I is the current, and the signs are reversed during discharging. Consequently, the rest of the cell (top and bottom of the electrode and membrane domains) is taken to be electrically insulated:

$$-\vec{n}\cdot\vec{j}_s^{\,cc}=-\vec{n}\cdot\vec{j}_s^{\,e}=-\vec{n}\cdot\vec{j}_l^{\,m}=-\vec{n}\cdot\vec{j}_l^{\,e}=0 \quad y=0 \text{ and } y=h_{cell} \tag{2.40}$$

The solid potential at the '-' current collector boundary is set to zero and is used as a reference potential for the remainder of the cell:

$$\phi_s^{cc} = 0 \qquad x = 0 \tag{2.41}$$

2.2.1.6 Inlet Concentration, Electrolyte Tanks, and Initial Values

During the operation of a VRFB, the concentrations of the species in the electrolyte tanks and the volumes of the electrolytes are constantly changing due to the electrochemical reactions and species crossover in the cell. To account for the changes in species concentrations, the inlet concentration for each species is simulated using the conservation of mass as follows:

$$\frac{\partial c_i^{in}}{\partial t} = \frac{\varepsilon w_{cell}}{V_j}\left(\int v_j^{out} c_i^{out} dl - \int v_j^{in} c_i^{in} dl\right) \qquad c_i^{in}(0) = c_i^0 \tag{2.42}$$

where V_j is the tank volume of half-cell *j*. The superscripts *in* and *out* refer to the value at the inlet or outlet of the electrode. Likewise, the changes in electrolyte volume can be calculated using the following differential equation:

$$\frac{\partial V_j}{\partial t} = \varepsilon w_{cell} L_e \left(v_j^{out} - v_j^{in}\right) \qquad V_j(0) = V_T^0 \tag{2.43}$$

The range of initial tank volumes, V_T^0, used in this study is given in Table 2.6 along with the operating conditions used in the simulations. It is important to note that the total electrolyte volume of each half-cell is taken as the sum of the tank volume (V_T^0) and the volume in the cell, whereas the electrolyte in the pumps and tubes is neglected.

The initial concentrations for the simulations are given in Table 2.7. The initial concentrations in the electrolytes represent a VRFB at 15% state of charge (SOC), where SOC is defined as follows:

Negative Electrolyte: $$SOC = \frac{c_{II}}{c_{II} + c_{III}} \quad (2.44a)$$

Positive Electrolyte: $$SOC = \frac{c_{V}}{c_{IV} + c_{V}} \quad (2.44b)$$

Total Cell: $$SOC = \frac{c_{II} + c_{V}}{c_{II} + c_{III} + c_{IV} + c_{V}} \quad (2.44c)$$

The concentrations of the sulfuric acid species (H^+, HSO_4^-, and SO_4^{2-}) in Table 2.7 were determined based on the electrolyte preparation method [24] and the degree of dissociation (β).

Table 2.6 Operating conditions and parameters

Symbol	Description	Value
V_T	Electrolyte volume in half-cell tank (ml)	21 - 56
T	Operating temperature (K)	300
I	Current (A)	0.4-0.5
ω	Inlet volumetric flow rate (ml min^{-1})	20-30
P_{out}	Outlet pressure (kPa)	100

2.2.1.7 Numerical Methods

The system of equations formulated above was solved using COMSOL Multiphysics software and the built-in tertiary current distribution, Darcy's Law, and ODE options. A mesh size of 380 elements was utilized, and the relative tolerance was set to 2.5 x 10^{-6}.

Table 2.7 Initial species concentrations

Symbol	Description	Value
c_{II}^{0}	V(II) initial concentration in negative electrolyte (mol m^{-3})	156
c_{III}^{0}	V(III) initial concentration in negative electrolyte (mol m^{-3})	884
c_{IV}^{0}	V(IV) initial concentration in positive electrolyte (mol m^{-3})	884
c_{V}^{0}	V(V) initial concentration in positive electrolyte (mol m^{-3})	156
c_{-,H^+}^{0}	H^+ initial negative concentration in negative electrolyte (mol m^{-3})	4447.5
c_{+,H^+}^{0}	H^+ initial positive concentration in positive electrolyte (mol m^{-3})	5097.5
$c_{-,HSO_4^-}^{0}$	HSO_4^- initial negative concentration in negative electrolyte (mol m^{-3})	2668.5
$c_{+,HSO_4^-}^{0}$	HSO_4^- initial positive concentration in positive electrolyte (mol m^{-3})	3058.5
$c_{Vanadium}^{0,m}$	Initial concentration of all vanadium species in membrane (mol m^{-3})	0
$c_{H^+}^{0,m}$	H^+ initial concentration in membrane (mol m^{-3})	1990

2.2.2 Experimental

2.2.2.1 Charge/Discharge Cycling

To provide data for model validation, performance tests were conducted using a vanadium flow cell with an active surface area of 10 cm^2. The cell contained two composite graphite current collectors and two GFA5 (SGL Carbon Group, Germany) carbon felt electrodes, which were separated by a Nafion® 117 membrane. The electrodes were heat-treated at 400 °C for 6 hours in air to functionalize their surface

[54]. To pretreat the Nafion®, the membrane was submerged in H_2O_2 for 30 min at 80 °C, then in boiling water for 30 min. Next, it was soaked in 0.5 M H_2SO_4 at 80 °C for 30 min, and finally cleansed in boiling water [8]. Two peristaltic pumps were used to circulate the '+' and '-' electrolytes between the cell and storage reservoirs, which were continuously purged with nitrogen gas. In the experiment, each half-cell contained 60 ml of electrolyte. The electrolytes were prepared by filling each half-cell with an initial 60 ml solution of 1040 mol m^{-3} $VOSO_4$ (VO^{2+}) in 4000 mol m^{-3} H_2SO_4 and charging the solutions at 1.7 V to produce '-' and '+' half-cell solutions consisting of V^{3+} and VO_2^+, respectively [55]. The '+' half-cell electrolyte was then replaced by 60 ml of the initial solution, resulting in final electrolyte solutions that consist of 1040 mol m^{-3} V^{3+} in 3480 mol m^{-3} H_2SO_4 in the '-' half-cell and 1040 mol m^{-3} VO^{2+} and 4000 mol m^{-3} H_2SO_4 in the '+' half-cell [38].

Charge/discharge testing of the VRFB was performed at a constant current of 0.4 A, and the electrolytes were maintained at a constant flow rate of 30 ml/min. The cell was charged to a maximum potential of 1.7 V and discharged to a minimum potential of 0.8 V. Open circuit measurements were performed after each galvanostatic charge/discharge step in order to determine the SOC of the system.

2.2.2.2 Electrode Properties

It is anticipated that the predictions of a VRFB model would be very sensitive to the input parameters used for the transport properties of the porous electrodes (i.e. porosity, specific surface area, and fiber diameter) [56-58]. Therefore, to further improve the accuracy of the model, the key structural properties (e.g., specific surface area, porosity and pore radius) of GFA5 graphite felt used in the experiments were

obtained using a suite of validated microstructure characterization algorithms described in the literature [56-58]. To summarize, the electrode material was initially imaged using a SkyScan 1172 x-ray tomograph. A binary segmentation was performed on the resulting tomogram to differentiate the solid and pore phases, and then the tomogram was assembled into a 3D virtual volume. A suite of microstructural analysis algorithms was applied to determine the porosity, mean pore diameter, and specific surface area of the material. The porosity was evaluated by discretely counting the number of voxels belonging to the pore phase versus the total number of voxels in the dataset, whereas the surface area was obtained by counting the number of voxel faces occurring at the interface between a pore voxel and a solid voxel. Iterative morphological image operations were used to determine the mean pore diameters. More detailed information regarding the algorithms can be found in [56-58]. These properties were used as input parameters for the electrode domain and are presented in Table 2.3.

Chapter 3. Validation and Case Study for Nafion® Membrane

Once the model was developed, the next step was to validate the model against experimental data. In the first part of this chapter, the model validation is presented. In the second part, a case study (using a Nafion® membrane) that has been performed to investigate the relative contribution of each species transport mechanisms (diffusion, convection, and migration) to the vanadium crossover and resulting capacity loss is presented.

3.1 Model Validation

3.1.1 Membrane | Electrolyte Interface

The first step in the model validation is to determine if the model properly predicts the concentration and potential jumps at the membrane | electrolyte interfaces. Due to the experimental limitations, it is very challenging to obtain in-situ data at these interfaces, which can be used for comparison against the predicted values. Therefore, to validate the interface model, the model predictions were compared against the values predicted by the Donnan potential ($\Delta\phi$), which represents the potential jump at the membrane | electrolyte interface for a system in equilibrium. In particular, the potential jump ($\Delta\phi$) and concentrations (c_c^e and c_c^m) at the interface predicted by the model were compared against the values computed by the Donnan potential given in Eq. 3.1 [59]:

$$\Delta\phi = \frac{RT}{F}\ln\left(\frac{c_c^e}{c_c^m}\right) \tag{3.1}$$

where the subscript c denotes the cation species.

Equation 3.1 is valid for a single cation electrolyte which is in equilibrium with a semi-permeable membrane (i.e., when no net charge transfer occurs across the membrane | electrolyte interface). However, the present model does not meet these requirements, as it has multiple cations and a net current. Therefore, in order to compare the results of the mass and charge transport equations (Eq. 2.24-27) against the Donnan potential, a simplified model that simulates a static flow cell in *equilibrium* was developed based on the formulation outlined in Section 2.2.1. In this model, the cell was assumed to be static $(\omega = 0)$ and there was no reaction current or net current density $(i = j = 0)$. All other initial values, parameters, and physics remained the same (Fig. 3.1a). Using the same numerical methods described in Section 2.2.1.8, the time dependent problem was solved until $\frac{\partial E_{cell}}{\partial t} \approx 0$, which indicates that the species within the electrolyte reached equilibrium. Figures 3.1b and 3.1c depict the predicted distributions of c_{H^+} and ϕ_l at the interfacial regions of the membrane during equilibrium. The transition from electrolyte to membrane occurs at x = 1.0 cm ('-' electrode interface) and x = 1.02 cm ('+' electrode interface). To compare the predictions, the c_{H^+} values captured from Figure 3.1b were incorporated into Eq. 3.1, and the theoretical Donnan potentials were calculated at the two interfaces. When these results were compared to the predicted potential jumps (Fig. 3.1c), an average error of 0.42% was observed, indicating that the present model can accurately capture the potential and concentration jumps at the membrane|electrolyte interfaces.

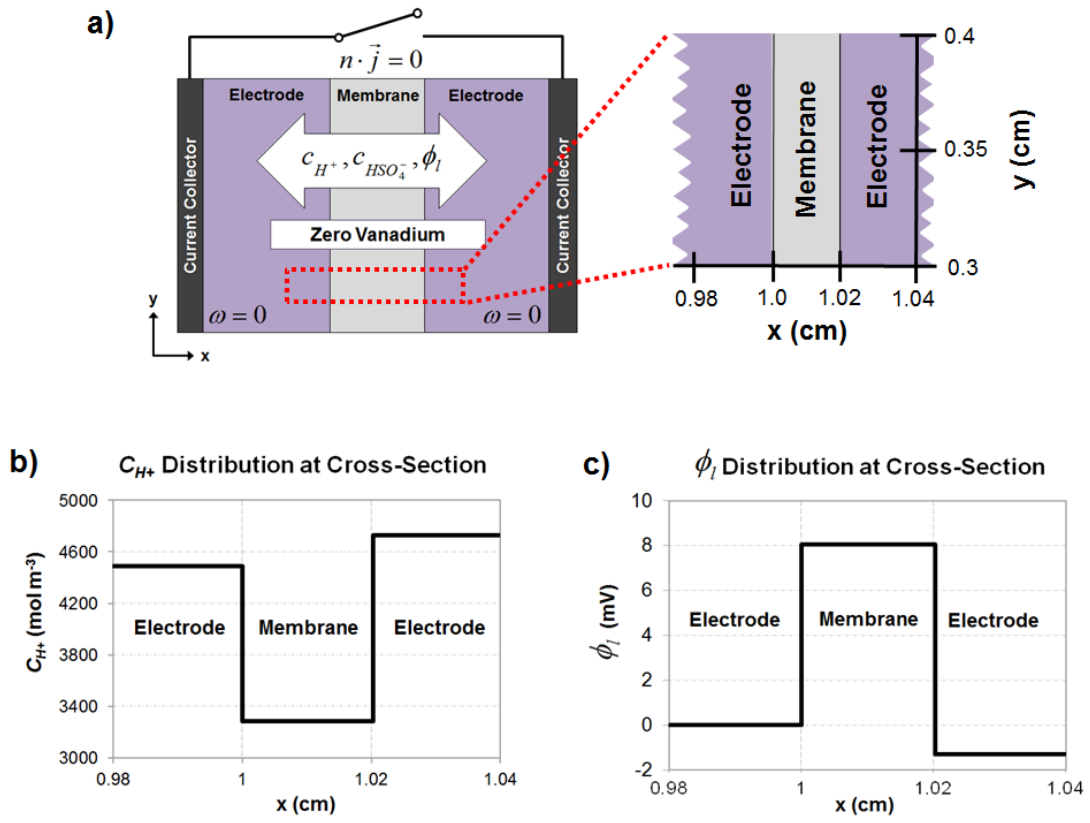

Figure 3.1 a) Schematic and parameters of simplified model used for interfacial physics validation; b) distribution of hydrogen proton concentration and c) distribution of electrolyte potentials across the membrane (electrode | membrane interfaces occur at x = 1 and x = 1.02 cm). All values in the distributions are taken at the y = 0.35 cm cross-section.

3.1.2 Performance and Capacity Loss Validation

The second step in the model validation is to compare the performance predictions of the model (i.e., voltage and capacity loss) with experimental data. First, a single-cycle was simulated to match the experimental operating conditions described in Section 2.2.2.1. The simulation was conducted as follows: *i)* charging was started at an initial SOC of 15%, *ii)* charging continued until the cell voltage reached 1.7 V, and *iii)* the cell was discharged until the SOC was 15%. The starting and ending SOC's of the simulation were selected to match the starting and ending experimental SOC data.

Figure 3.2a shows the comparison between the simulated results and experimental data. A very good agreement in voltage (less than 2% average error) was observed. This accuracy is a result of three main factors: *i)* the inclusion of the contribution of the hydrogen protons at the '+' electrode in the Nernst equation, *ii)* the incorporation of additional potential jumps at the membrane|electrolyte interfaces, and *iii)* the fact that both the '–' and '+' reaction rate constants (k_- and k_+) and charge transfer coefficients (α_- and α_+) were taken as fitted parameters. The values of k and α have not been reported in the literature for the graphite felt used in the experimental set-up. It is also important to note that along with k and α, the diffusion coefficient of V(II) in the membrane (3.125 x 10^{-12} m^2 s^{-1}) and the electrokinetic permeability (1.13 x 10^{-20} m^2) of the membrane were also taken as fitted parameters due to the lack of data for Nafion® 117 in literature, and to match the coulombic efficiency of the experimental data (97%).

A second validation was performed to compare the capacity loss predicted by the model after 45 cycles against experimental data published by Kim et al. [8]. The tests in [8] were conducted at the following conditions: 50 ml of electrolyte per half-cell, electrolyte concentrations of 2000 mol m^{-3} vanadium and 5000 mol m^{-3} total sulfate, electrode surface area of 10 cm^2, a constant flow rate of 20 ml min^{-1}, and a constant current of 0.5 A. The model was simulated under similar conditions, however the electrolyte volume and vanadium concentration were reduced to 25 ml and 1040 mol m^{-3}, respectively to reduce the computing time. During the simulation, the cell was charged to a maximum voltage of 1.7 V and discharged to a minimum voltage of 1.1 V, which is equivalent to ~95% and ~10% SOC, respectively. The capacity for each simulated cycle was calculated in reference to the discharge time of the first cycle:

$$capacity = \left(\frac{t_{dis,n}}{t_{dis,1}} \right) \times 100\% \tag{3.2}$$

where, $t_{dis,n}$ is the discharge time of the n^{th} cycle. A comparison between the simulated results and the experimental data is shown in Fig. 3.2b. Over the 45 cycles, an average error of 4.2% (consistent throughout the cycles) is observed between the simulated and experimental results. It is anticipated that this slight discrepancy is due to the fact that crossover is the only source of capacity loss in the model. Other factors such as gas evolution, shunt currents, and electrolyte leakage that may affect the capacity loss in the experiments are assumed negligible.

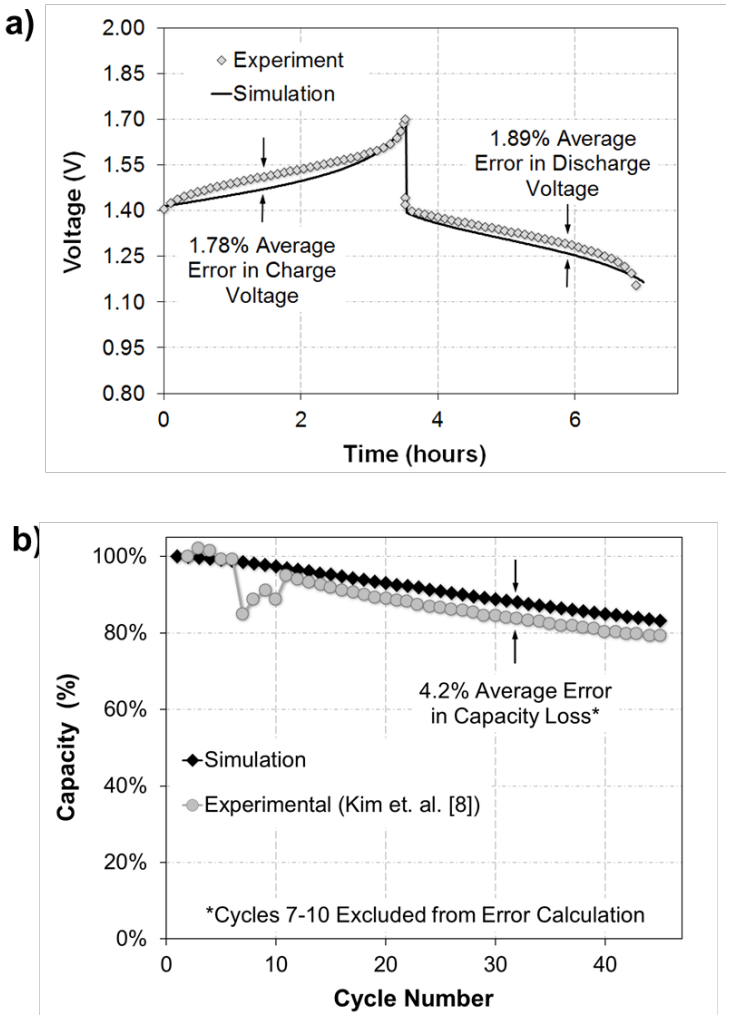

Figure 3.2 a) Comparison of simulated results with experimental data for a 10 cm^2 VRFB with a half-cell electrolyte volume of 60 ml and a concentration of 1040 mol m^{-3} vanadium and 5000 mol m^{-3} sulfate. The cell was operated at a 30 ml min^{-1} electrolyte flow rate and a 40 mA cm^{-2} constant current density. b) Comparison of the change in cell capacity (discharge time) after 45 cycles between the simulation and experimental data published in [8] for a 10 cm^2 VRFB cell operated at a 20 ml min^{-1} electrolyte flow rate and a 50 mA cm^{-2} constant current density.

3.2 Concentration and Current Distributions in Electrodes

Once validated, the simulations were performed to assess the model capabilities. Figure 3.3a depicts the concentration distribution in the '+' and '-' electrodes at 50% SOC during charging of the cell. These results were obtained for the single cycle

simulation. The simulation results indicate that both the '+' and '-' electrolytes show an increase in proton concentration along the y-axis. The concentration increase in the '+' electrolyte can be attributed to the redox reaction at the electrode surface, whereas the increase in the '-' electrolyte can be attributed to the transport of hydrogen protons across the membrane (from '+' to '-' electrode) to maintain electroneutrality. In addition, Fig. 3.3a shows a disparity in concentration between the two half-cells, which is believed to be caused by the electrolyte preparation method [59].

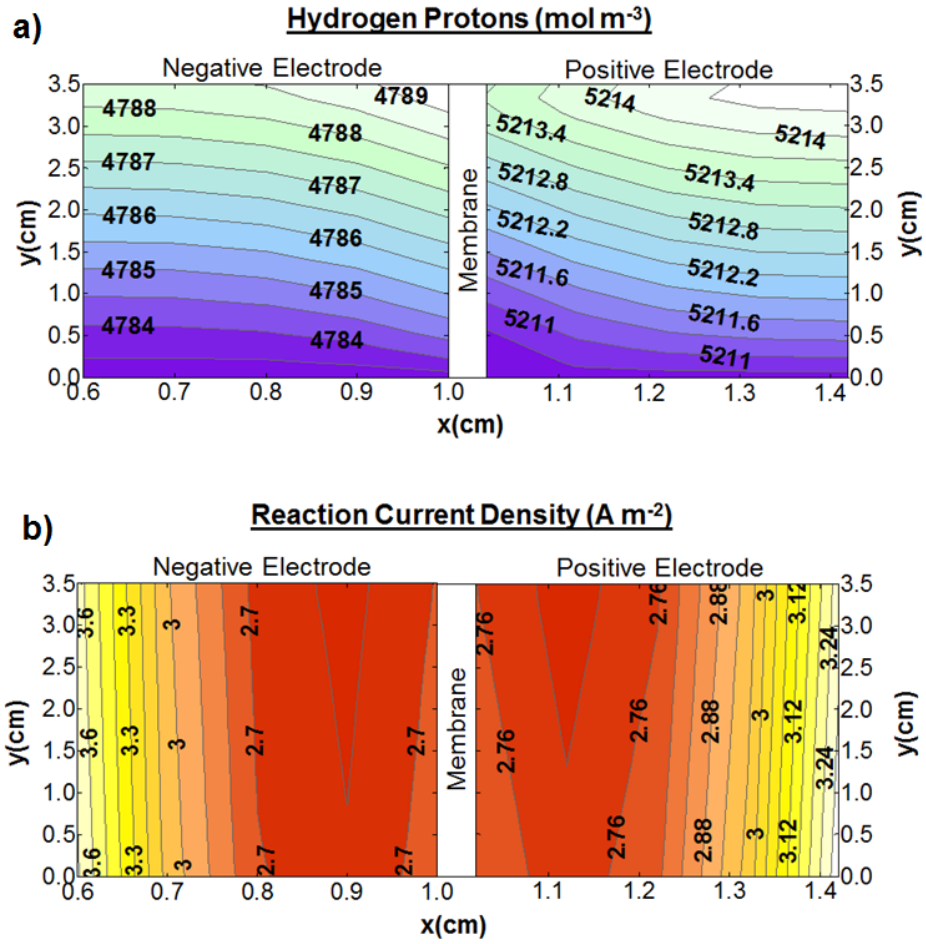

Figure 3.3 Distributions of a) hydrogen proton concentration and b) magnitude of reaction current density during charging at 50% SOC. Data taken from the single cycle simulation (10 cm^2 cell, 30 ml min^{-1} electrolyte flow rate, and 40 mA cm^{-2} constant current density).

Figure 3.3a also shows a slight increase in the proton concentration near the '+' current collector (x = 1.42 cm). It appears that this increase in concentration can be caused by the high reaction current near the current collector (Fig. 3.3b), which corresponds to a higher production of hydrogen protons. The observed increase of the reactions in the vicinity of the current collectors can be attributed to the fact that the conductivity of the solid electrode (σ_s^e) is lower than the conductivity of the liquid electrolyte (σ_l^{eff}). In other words, the ionic current is expected to be more favorable than the electronic current because the electrolyte region is less resistive than the electrode region. In order to minimize the electronic and maximize the ionic current, a large amount of reactions is expected to occur close to the current collector.

For this simulation, the conductivity of the solid electrode is taken as 66.7 S m^{-1} (reported by manufacturer) and the average effective conductivity of the electrolyte is 200 S m^{-1} (found from Eq. 2.23). The low conductivity in the electrode and high conductivity in the electrolyte is most likely due to the high porosity ($\varepsilon = 0.93$) of the carbon felt. The high porosity corresponds to a low quantity of connected fibers (high resistance) for electron transport and a large amount of void space (less resistance) for ion transport. These predictions highlight the importance of analyzing the tradeoffs between electronic and ionic conductivity when designing a high performance electrode material.

3.3 Simulated Performance for 45 Cycles

The model was also utilized to investigate the trends in performance over 45 cycles. The voltage curves for the first 5 and last 5 charge/discharge cycles are provided in Fig. 3.4a, and the charge time, discharge time, and percent capacity loss for each

cycle are given in Fig. 3.4b. Overall, a 16.9% decrease in discharge time is predicted after ~100 hours of operation, which corresponds to a reduction in discharge time from 72.6 to 60.3 minutes. As anticipated, the model results also suggest that the vanadium transport through the membrane significantly reduces the lifetime of a VRFB.

Figure 3.5a shows the voltage, coulombic, and energy efficiencies for all 45 cycles, which have average values of 83%, 97%, and 80.5%, respectively. The simulations show that there is no significant change in the efficiencies after 45 cycles, suggesting that the loss in capacity has a minimal effect on the cell efficiencies. The same behavior was also reported by Kim et. al. [8] for 45 experimental charge/discharge cycles. Figure 8b shows the SOC of the '+' half-cell, '-' half-cell, and whole cell at the maximum charging cut-off voltage of 1.7 V for each cycle. From Fig. 3.5b, it appears that the loss in charge/discharge capacity occurs due to a decrease in the maximum SOC of the whole cell, which indicates that the amount of vanadium reacting during charging is decreasing over time. This behavior suggests that there may be a net transfer of vanadium from one half-cell to the other. To clarify, if one half-cell is becoming depleted and the other enriched with vanadium, the charging time will be limited by the amount of vanadium in the depleted half-cell. All of the vanadium in the depleted half-cell is expected to react during charging, which will cause the cell to reach the cut-off voltage before all the vanadium in the enriched half-cell can react. This will result in the depleted half-cell maintaining a high SOC at the end of charging while the SOC of the enriched half-cell decreases for each cycle.

a)

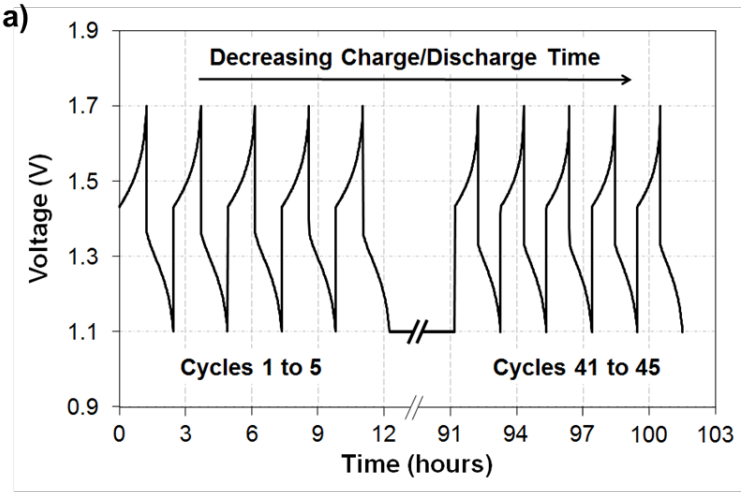

b)

Cycle	Charge Time (seconds)	Discharge Time (seconds)	Capacity (%)
1	4512	4356	100.0%
2	4490	4349	99.8%
3	4479	4341	99.7%
4	4468	4329	99.4%
5	4455	4317	99.1%
⋮	⋮	⋮	⋮
41	3793	3685	84.6%
42	3776	3668	84.2%
43	3761	3653	83.9%
44	3745	3637	83.5%
45	3730	3621	83.1%

Figure 3.4 a) Charge/discharge performance of cycles 1 to 5 and 41 to 45 for the extended charge/discharge simulation (10 cm^2 cell, 20 ml min^{-1} electrolyte flow rate, and 50 mA cm^{-2} constant current density). b) Tabulated data of the charge/discharge times and percent of initial capacity for the cycles shown in part (a).

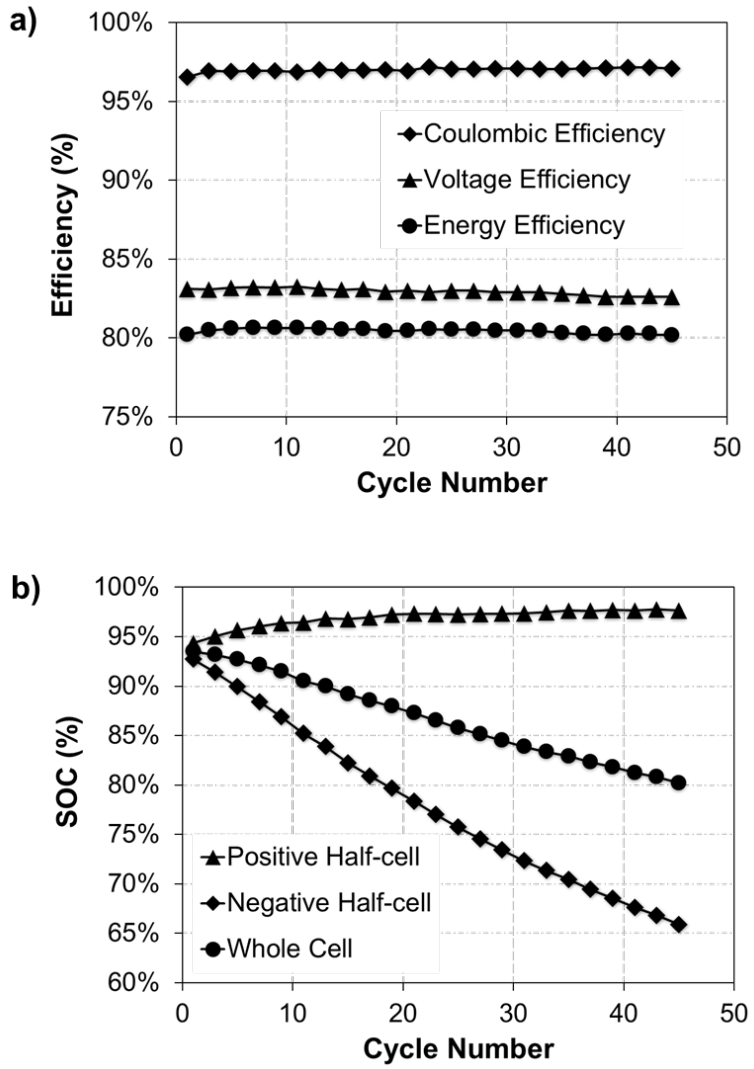

Figure 3.5 a) Efficiencies and b) maximum state of charge (SOC) for the extended charge/discharge simulation (10 cm^2 cell, 20 ml min^{-1} electrolyte flow rate, and 50 mA cm^{-2} constant current density). Maximum SOC was determined at the cut-off voltage of 1.7 V.

Based on the simulation results shown in Fig. 3.5b, it appears that the '+' half-cell has a consistently high SOC (greater than 94%) at the end of charging, while the SOC in the '-' half-cell is steadily declining. This trend suggests that the '+' half-cell SOC is being depleted of vanadium while the '-' half-cell is becoming enriched. In other words, the simulation indicates that a net vanadium transfer from the '+' to '-' half-cell may be responsible for the decrease in the maximum SOC of the cell, and hence, the capacity of the system.

3.3.1 Trends in Vanadium Crossover

Figure 3.6a plots the total amount of vanadium in each half-cell (electrode + tank) at the end of each cycle, where cycle "0" represents the initial conditions. As expected from the observed trends in SOC, the simulation indicates a net transfer of vanadium from the '+' to '-' half-cell. Previous studies have predicted [34-35] that the net rate of vanadium crossover occurs from the '-' to '+' half-cell due to the higher average diffusion coefficients of V^{2+} and V^{3+} as compared to VO^{2+} and VO_2^+. However, the simulations herein show the opposite trend, which might be due to the fact that diffusion may not be the dominating mechanism of species transport in the membrane for the operating conditions and input parameters tested in this study. Depending upon the operating conditions (e.g., constant flow rate, constant pressure, etc.), the contribution of convection and migration on the species transport can be more significant as compared to diffusion, which may result in a different trend in vanadium transfer. For instance, a constant flow rate operation can cause pressure gradients across the membrane due to the difference in viscosities of the electrolyte in + and – half cells, which can promote the convective transport of vanadium ions. It is important to note that the predicted trends also depend strongly on the values used for the electrolyte viscosities, as they indicate the direction of the pressure drop across the membrane. Therefore, along with the membrane properties, the effects of operating conditions and electrolyte properties on the crossover should be carefully analyzed to better understand the mechanisms responsible for the crossover and capacity losses.

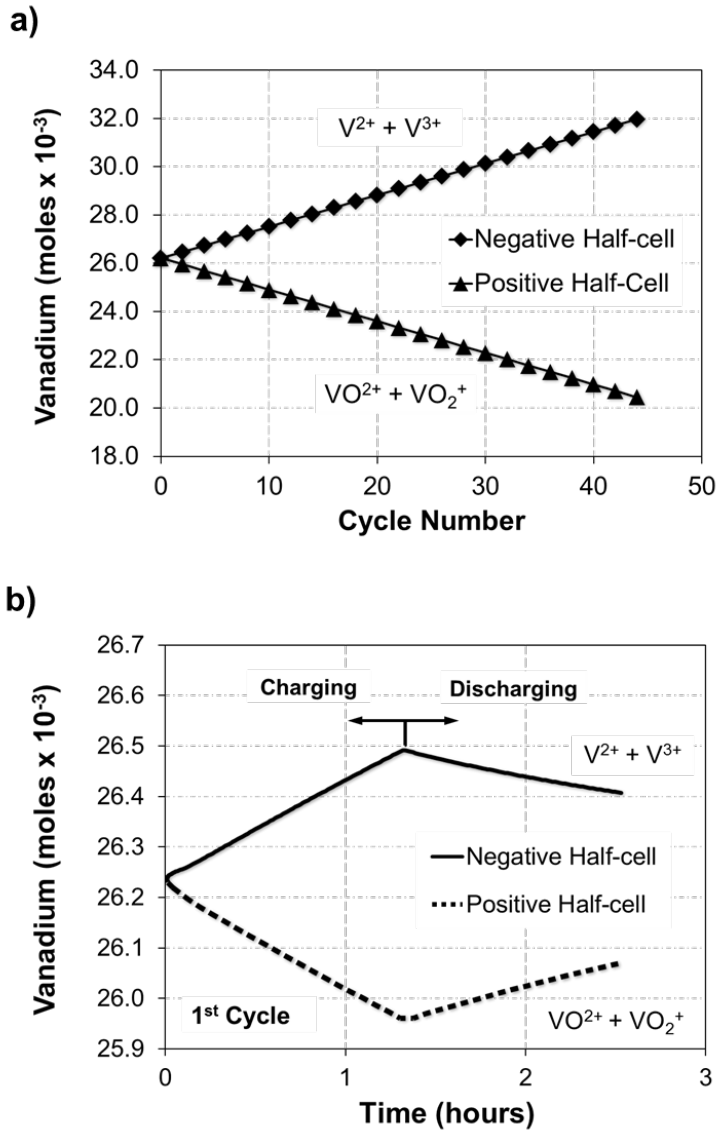

Figure 3.6 Quantity of vanadium in each half-cell a) at the end of each cycle and b) during the first charge/discharge cycle of the extended simulation (10 cm^2 cell, 20 ml min^{-1} electrolyte flow rate, and 50 mA cm^{-2} constant current density).

Similarly, Fig. 3.6b shows the total amount of vanadium in each half-cell during the first charge/discharge cycle. According to the simulation, the net vanadium crossover in the cell is always in the same direction as the cell current. During charging, the net vanadium crossover is from the '+' to '-' half-cell and vice versa for discharging. The observed trends are believed to be caused by the contributions of migration and

electro-osmotic convection towards the total vanadium flux. Figure 3.6b also shows that the amount of vanadium in each half-cell remains unbalanced at the end of the cycle, which is due to the fact that the net amount of crossover from the '+' to '-' half-cell during charging exceeds the net amount of crossover from the '-' to '+' half-cell during discharging. This data also verifies the exchange in total vanadium between the half-cells observed over the 45 cycles.

3.4 Species Distribution in the Membrane

3.4.1 Hydrogen Protons, Bisulfate, and Potential

The model was also solved to predict the species and potential distribution in the membrane during operation. Figure 3.7 shows spatial distributions of hydrogen protons, bisulfate ions (HSO_4^-), and potential in the membrane during charging at 50% SOC. This data was taken from the 45th cycle of the extended charge/discharge simulation. The model predictions suggest that there exist significant amount of sulfuric acid (protons and bisulfate) in the membrane, which varies within the membrane. In addition, a small ohmic drop of ~2.5 mV is predicted across the membrane, indicating a low membrane resistance, which is most likely as a result of the high proton conductivity of Nafion® 117.

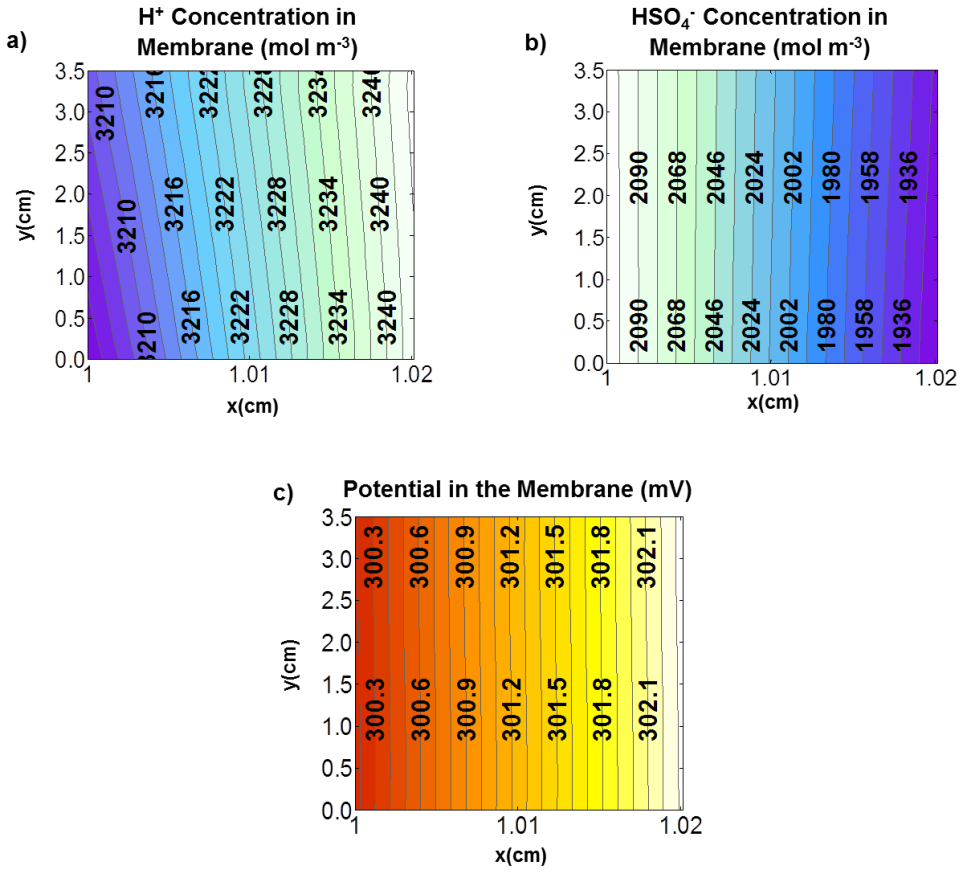

Figure 3.7 Distributions of a) hydrogen proton concentration, b) bisulfate concentration, and c) potential in the membrane during charging at 50% SOC. Data taken from the 45th cycle of the extended charge/discharge simulation (10 cm^2 cell, 20 ml min^{-1} electrolyte flow rate, and 50 mA cm^{-2} constant current density).

3.4.2 Vanadium Concentration and Flux

Figure 3.8 shows the concentration distributions and fluxes of V^{3+} in the membrane at 50% SOC for the 45th cycle of the charge/discharge simulation. The results indicate that convection and migration have significant contributions to the total flux across the membrane. Figure 3.8d shows that convection and migration account for 29% of the total flux across the membrane during discharging, suggesting that the directions of these two transport mechanisms may be responsible for a significant decrease (~80%) in the net flux of V^{3+} during charging as compared to discharging. This behavior can be attributed to the fact that convection and migration occur in the same

direction as current. For instance, during charging, the net flux is reduced because convection and migration occur in the opposite direction of diffusion. Consequently, during discharging, all three transport mechanisms are in the same direction and a higher rate of crossover is observed.

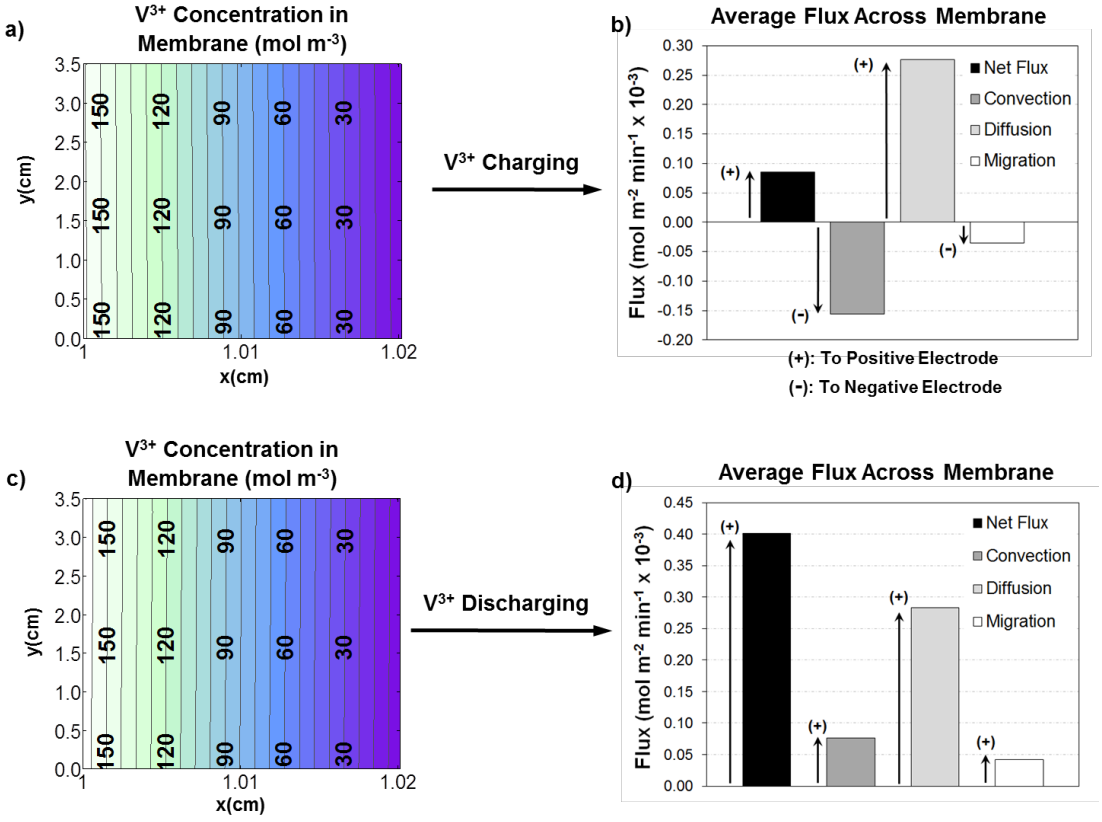

Figure 3.8 Concentration distributions (a, c) and average fluxes (b, d) of V^{3+} in the membrane during charging (a, b) and discharging (c, d). Data obtained at 50% SOC during the 45th cycle of the extended charge/discharge simulation (10 cm^2 cell, 20 ml min^{-1} electrolyte flow rate, and 50 mA cm^{-2} constant current density).

Figure 3.9 shows the concentration distributions and fluxes of VO^{2+} in the membrane at 50% SOC. Similar to V^{3+}, Fig. 3.9 also suggest that convection and migration have a significant impact on the net crossover of VO^{2+}. For instance, Fig 3.9b shows that these two transport mechanisms account for 44% of the total flux across the membrane during charging. Accordingly, the direction of convection and migration

can cause a significant decrease (~65%) in the net flux of VO^{2+} during discharging as compared to charging. In fact, when analyzed with the trends observed for the V^{3+} flux, this data suggest that during charging, convection and migration cause a net vanadium crossover from the '+' to '–' half-cell and vice versa for discharging. As expected, these trends in flux support the observed changes in vanadium over a single charge/discharge cycle; such that the total amount of vanadium increases in the '–' half-cell and decreases in the '+' half-cell during charging, and vice versa for discharging.

3.5 Conclusions

A new mathematical framework for a 2-D, transient, isothermal VRFB model which incorporates the transport of all charged species (i.e. vanadium ions, protons, and bisulfate) across the membrane due to convection, diffusion, and migration was developed. The model accounts for the changes in the membrane potential due to the species concentrations and the semi-perm-selective nature of the membrane, and includes variations in the electrolyte volumes as a result of convection across the membrane. In addition, the model captures the discontinuities in the potential and species concentrations at the membrane | electrolyte interfaces and incorporates the effects of side reactions as a result of vanadium crossover.

Based on the input parameters used, the model predictions suggest that the electrode and electrolyte conductivities determine the location of the reactions, and for this study, the majority of the reactions is found to occur in the vicinity of the current collectors due to the lower conductivity of the solid electrode as compared to the liquid electrolyte. The 45 cycle simulations indicate that the loss in capacity may have

a minimal effect on the cell efficiencies and that a net transfer of vanadium from the '+' to '-' half-cell is responsible for the loss in capacity. The analysis of the mathematical formulation suggests that the predicted trends are highly dependent on the operating conditions and input parameters (especially flow rates and viscosities) used in the simulation. Additionally, the ohmic loss is found to be relatively small across the membrane (~2.5 mV) due to the high proton conductivity of Nafion® 117. Finally, the predicted trends of vanadium concentration and flux in the membrane suggest that depending upon the operating conditions, along with diffusion, convection and migration can significantly impact the rate and direction of crossover during VRFB operation.

An in-depth study that includes the analysis of different membrane materials and varying operating conditions is given in the following chapters to better understand the driving mechanisms responsible for the crossover, capacity loss, and related performance loss (i.e., efficiencies and power output).

Chapter 4. Role of Membrane Properties on Capacity Loss and Performance of a VRFB

This chapter focuses on the influence of membrane properties (i.e., thickness and chemical properties of the membrane) on the VRFB cell performance. In the first part, the analysis on the crossover characteristics of proton and anion exchange membranes is presented. In the second part, the relation between membrane thickness and the VRFB performance for proton exchange membranes is presented to provide an understanding of crossover/resistance trade-off in these systems.

4.1 Membrane Type

The objective of this section is to investigate the species transport mechanisms governing crossover in different types of membrane. More specifically, the contribution of each transport mechanism to the vanadium transfer across different types of membrane is analyzed during cycling. This section also demonstrates how chemical structure of the membrane can be used to mitigate crossover and improve the long-term performance of a VRFB.

4.1.1 Proton Exchange Membranes (PEMs)

4.1.1.1 Introduction

The rate of species transport across the membrane is primarily governed by the chemical composition and properties of the membrane. Ideally, the membranes used in VRFBs should have good chemical stability and mechanical durability for longevity, high proton conductivity for low ionic resistance and desired permselectivity for low vanadium crossover and capacity fade [36]. To date, research on membranes for VRFBs has centered on the development of new materials or

alteration of commercially available membranes [16-19], which are primarily designed for other applications such as fuel cells. Significant effort has been placed on development of proton exchange membranes (PEMs) [60-61], anion exchange membranes [62-64], nanoporous membranes [65] and amphoteric membranes [17,66] that are applicable to VRFB operation. While each of these membranes has its own advantages and disadvantages, PEMs constitute the majority of the separators studied in the literature because of their well-known characteristics, high proton conductivity and good chemical stability [8,67].

Among PEMs, Nafion® developed by DuPont in the 1960's has been widely studied and tested in VRFB applications due to its good proton conductivity and excellent chemical stability [68]. One major issue with the use of Nafion® is that it has low vanadium ion selectivity; as such it suffers from high vanadium permeation which leads to significant capacity fade with cycling [16]. Another concern with Nafion® is that it is currently very expensive (~41% of the total cost of a VRFB), which makes this type of membrane prohibitive for use in grid-scale electrical energy storage devices, such as VRFBs [22-23,69]. To enhance the ion selectivity of Nafion®, several surface modification or inorganic doping processes were proposed and evaluated [20-21]. While these modifications have shown to be effective at reducing vanadium permeability to some extent, the cost issue associated with the use of Nafion® still remains a major challenge. As a result, recent efforts have been placed on investigation of alternative proton exchange membranes that are inexpensive, yet possess desired performance and durability characteristics required for long-term VRFB operation.

Among alternatives to Nafion®, a number of sulfonated aromatic polymers such as poly(phthalazinone ether)s [70], poly(arylene ether ketone)s [71-73], poly(imide)s [74] and poly(arylene sulfone)s [75-76] have been studied to explore their performance and suitability for use in VRFBs. These low-cost aromatic polymers have been shown to provide reasonable proton conductivity, low vanadium ion permeability, good oxidative stability and reasonable mechanical stability, which make them very promising candidates for use in VRFBs [15]. Recently, Hickner and coworkers [8, 69] functionalized a commercially available polyphenylsulfone resin - Radel (Solvay Plastics, Alpharetta, GA) - with sulfonic acid groups, and investigated the performance of the sulfonated Radel membrane (s-Radel) in a VRFB operation [8]. They demonstrated high coulombic efficiency, low capacity fade rate (almost half that of Nafion® with comparable energy efficiency) and long open circuit voltage retention time [8]. While s-Radel membranes have been shown to possess superior ion selectivity, one major issue with this type of membrane is its low proton conductivity and mechanical durability during VRFB cycling [69]. Increasing the ion exchange capacity (IEC) of these polymers can easily improve their proton conductivity; however the increase in IEC often results in an increase in vanadium permeability, increased water uptake and loss of mechanical integrity of these membranes [77]. To date, the performance tradeoff between vanadium permeability and ion conductivity in this class of membranes during device operation is not well understood, and thus represents a major challenge to the design of new materials of this type. Currently there is little understanding of the ion transport mechanisms governing species crossover during device operation and how the transport properties under operational environments are related with the membrane composition/properties. If the transport relationships during device operation could be better understood, studies properly

accounting for these effects could be performed and optimized materials could be designed.

In this section, the model explained in Chapter 2 was used to investigate and compare the ion transport mechanisms governing species crossover in Nafion® and s-Radel membranes to provide insight into the connection between the ion conductivity, vanadium crossover and battery performance characteristics of these membranes. Simulations were performed for extended charge/discharge cycles to quantify the nature of transport mechanisms of vanadium ions in these membranes (such as relative contribution of diffusion, migration, osmotic convection and electro-osmotic convection on vanadium crossover) with respect to their compositions/basic properties, and to link this understanding to the observed performance differences reported in experimental studies.

4.1.1.2 Simulated Case Studies

Two case studies were conducted to predict the performance of a VRFB: one for Nafion® 117 and the other one for s-Radel membrane. For both cases, the same parameters for the electrode and the current collector were used, while the membrane properties were varied based on the membrane material. The properties for the Nafion® 117 and s-Radel membrane used in these simulations are listed in Table 4.1. The properties of Nafion® 117 were obtained from the literature, whereas the key transport properties of s-Radel, including the conductivity and the vanadium permeability were taken from a previous study in the literature where these properties were measured experimentally [8].

Simulations for Nafion® and s-Radel were conducted for a cell with a 10 cm^2 active area. The model was run to simulate the charging and discharging for 45 cycles at a current density of 50 mA cm^{-2} with an electrolyte flow rate of 20 ml min^{-1}. The cutoff voltage for each cycle was set at 1.1 and 1.7 V for discharge and charge, which corresponds to ~10% and ~95% SOC, respectively. The complete set of operating conditions used in simulations is provided in Table 4.2.

Table 4.1 Membrane properties and parameters used in the model

Symbol	Description	Nafion® 117	S-Radel
L^m	Membrane thickness (μm)	203 [49]	115
c_f	Fixed acid concentration (mol m^{-3})	1432 [49]	2800
κ_ϕ	Electrokinetic permeability (m^2)[a]	1.13 x 10^{-20}	7.533 x 10^{-21}
κ_p	Hydraulic permeability (m^2)	1.58 x 10^{-18} [50]	5.27 x 10^{-19}
D_{II}^m	V(II) membrane diffusion coefficient (m^2 s^{-1})[a]	3.125 x 10^{-12}	2.0 x 10^{-13}
D_{III}^m	V(III) membrane diffusion coefficient (m^2 s^{-1})	5.93 x 10^{-12} [51]	3.80 x 10^{-13}
D_{IV}^m	V(IV) membrane diffusion coefficient (m^2 s^{-1})	5.0 x 10^{-12} [51]	3.21 x 10^{-13}
D_V^m	V(V) membrane diffusion coefficient (m^2 s^{-1})	1.17 x 10^{-12} [51]	7.5 x 10^{-14}
$D_{H^+}^m$	H^+ membrane diffusion coefficient (m^2 s^{-1})	3.35 x 10^{-9} [47]	2.68 x 10^{-9}
$D_{HSO_4^-}^m$	HSO_4^- membrane diffusion coefficient (m^2 s^{-1})	4 x 10^{-11} [52]	2 x 10^{-11}

[a] Fitted parameter

Table 4.2 Operating conditions and parameters

Symbol	Description	Value
V	Electrolyte volume in half-cell (ml)	25
T	Operating temperature (K)	300
I	Applied current (mA)	500
A	Electrode area (cm^2)	10
ω	Inlet volumetric flow rate (ml min^{-1})	20
μ_+	Positive electrolyte viscosity (Pa s)	2.5 x 10^{-3}
μ_-	Negative electrolyte viscosity (Pa s)	12.5 x 10^{-3}
c_v^0	Initial vanadium concentration (mol m^{-3})	1040
$c_{XSO_4^{2-}}$	Total sulfate concentration (mol m^{-3})	5040

4.1.1.3 Results and Discussions

4.1.1.3.1 Changes in Amount of Vanadium with Cycling

As a first step to investigate the differences in vanadium transport across these membranes, % change in the amount of vanadium in each half-cell was analyzed. Fig. 4.1 shows the change in the amount of vanadium in the half-cells at the end of each cycle for both membranes. It is observed that for both Nafion® and s-Radel, the amount of vanadium in the positive half-cell increases at the end of each cycle, indicating that the net vanadium transfer occurs from negative to positive half-cell. Fig. 4.1 also shows that the amount of net vanadium crossover per cycle through s-Radel is almost half of that of the Nafion®. This suggests that s-Radel experiences less imbalance of electrolyte composition between half-cells and there is less

vanadium transfer from negative to positive half-cell. Therefore, s-Radel retains higher capacity at the end of each cycle, which agrees with the experimental study by Kim et al [8].

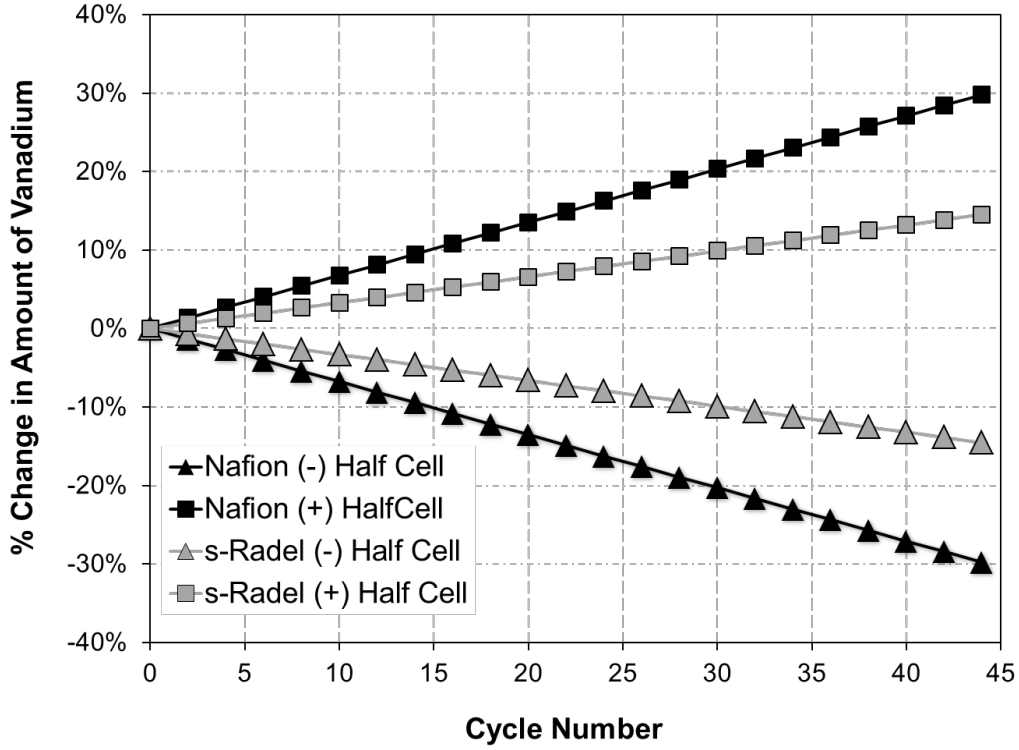

Figure 4.1 Predicted % change in amount of vanadium at positive and negative half-cells at the end of each cycle for Nafion® 117 and s-Radel.

To further investigate the trends in vanadium crossover, the change in the amount of vanadium in each half-cell during charge and discharge was analyzed separately for each cycle and a representative analysis for the 10th cycle is shown in Fig 4.2. It is observed that the net rate of vanadium crossover is greater during "discharging" than "charging" for both membranes. For instance, at the 10th cycle for Nafion®, the percentage change in total vanadium between half-cells is found to be ~ 0.15% during charge and ~ 0.60% during discharge. Similarly, a ~ 0.25% and ~ 0.50% change is observed for s-Radel during charge and discharge, respectively. Another interesting observation is that for Nafion®, the net vanadium transfer is found to be always in the

same direction (i.e., towards the positive half-cell) during charging and discharging, but changes in magnitude from charge to discharge (i.e., the net vanadium transfer during discharge is almost twice than that of during charge). On the other hand, the net vanadium transfer in s-Radel appears to change direction (i.e., towards the negative half-cell during charging and towards the positive half-cell during discharge). These different trends in the direction of vanadium transport during charge and discharge for the two membranes suggests that the vanadium crossover is dominated by different transport mechanisms in these membranes due to the differences in material properties, which requires further investigation of contribution of each transport mode (i.e., diffusion, convection and migration) on vanadium crossover.

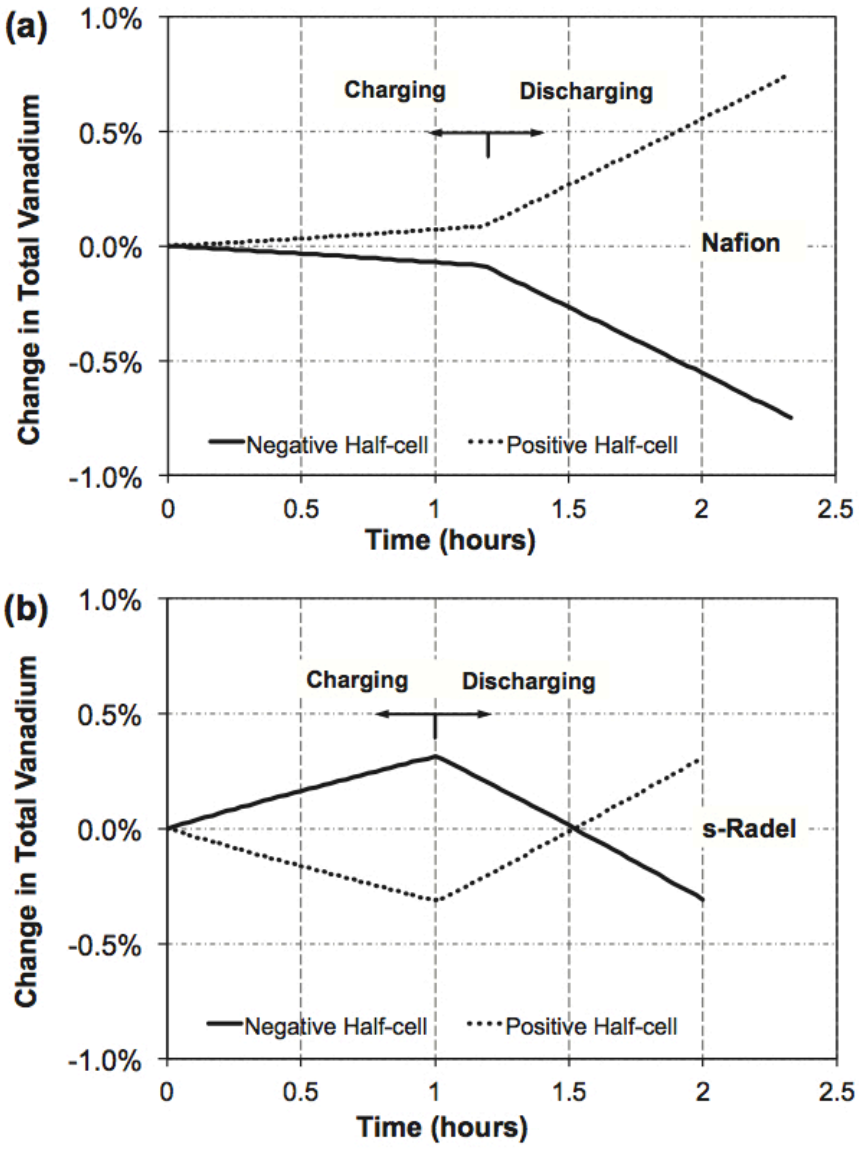

Figure 4.2 Predicted change in vanadium during charge and discharge at both half-cells at the 10th cycle (a) for Nafion® 117 and (b) for s-Radel membrane.

4.1.1.3.2 Crossover Transport Mechanisms for Each Species

To identify the dominant transport mechanism responsible for vanadium crossover in Nafion® and s-Radel, the contribution of each transport mode (i.e., diffusion, convection and migration) to the net vanadium transfer was analyzed for all vanadium species (i.e., V^{2+}, V^{3+}, V^{4+}, and V^{5+}). Figs. 4.3 and 4.4 show the computed mass fluxes of $V^{2+}|V^{3+}$ (negative half-cell) and $V^{4+}|V^{5+}$ (positive half-cell) through Nafion® and s-Radel during the 40th cycle. In these figures, positive (+) flux indicates species

transport towards the positive electrode, and negative (-) flux indicates species transport towards the negative electrode.

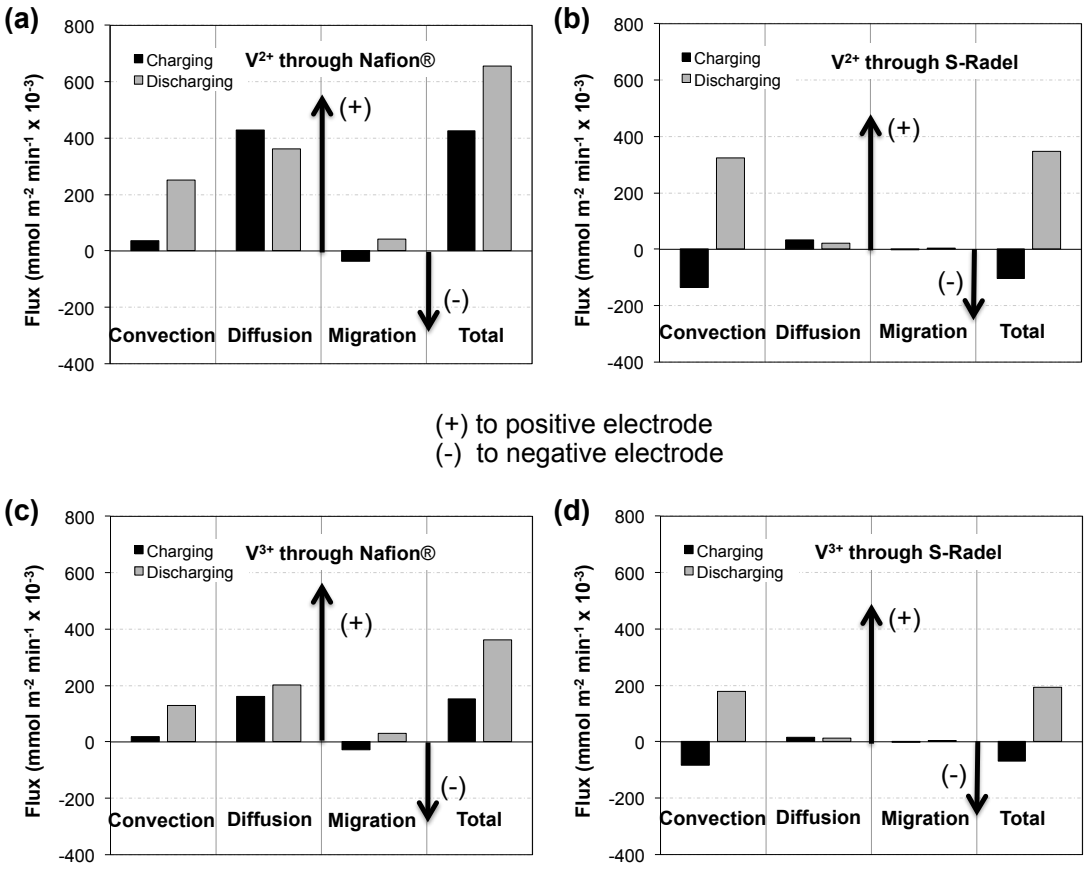

Figure 4.3 Mass fluxes of vanadium species via convection, diffusion, and migration at 50 % SOC of 40th cycle during charging and discharging: (a) V^{2+} through Nafion® 117, (b) V^{2+} through s-Radel, (c) V^{3+} through Nafion® 117, and (d) V^{3+} through s-Radel.

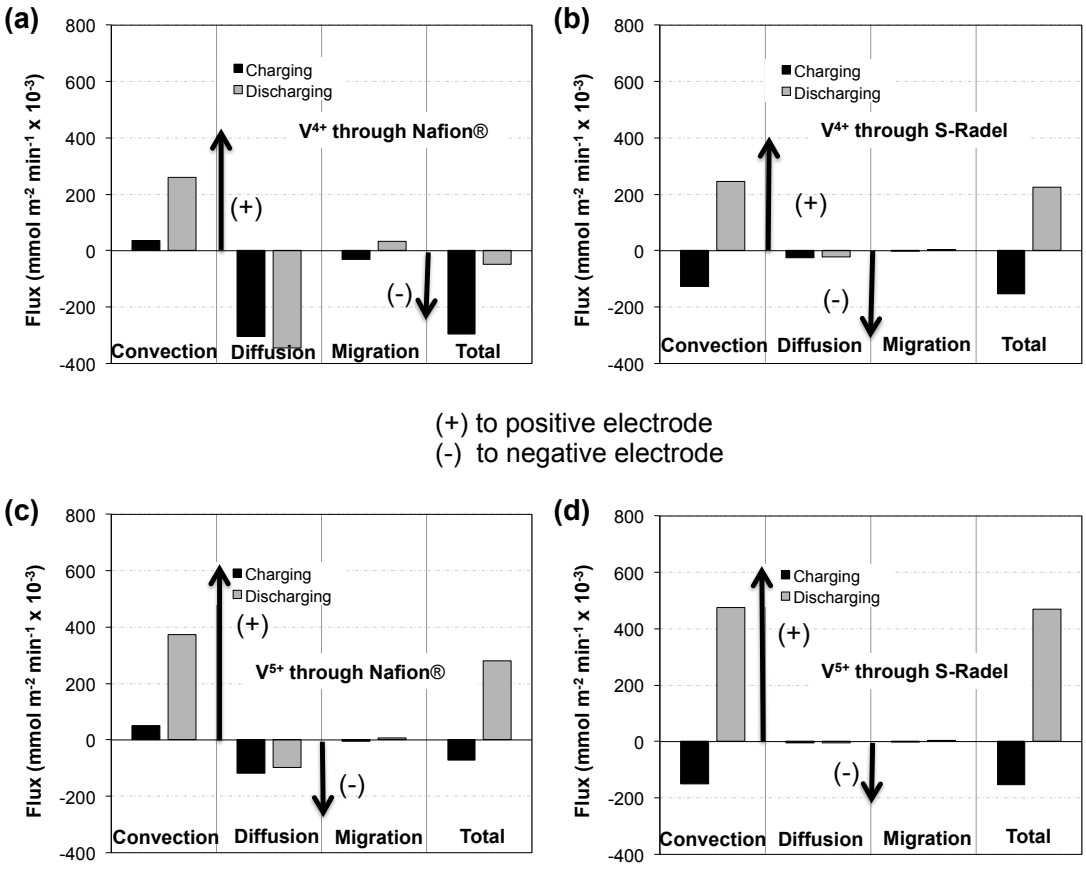

Figure 4.4 Mass fluxes of vanadium species via convection, diffusion, and, migration at 50 % state of charge of 40th cycle during both charging and discharging (a) V^{4+} through Nafion® 117, (b) V^{4+} through S-Radel, (c) V^{5+} through Nafion® 117, (d) V^{5+} through S-Radel.

Trends in Nafion® 117*:* It is apparent from Figs. 4.3 and 4.4 that diffusion is the dominating transport mechanism responsible for vanadium crossover in Nafion®. For each species, diffusion occurs in the same direction during charge and discharge. When the magnitudes of the transport modes are compared, diffusion is observed to be much greater than convection and migration for each species, expect V^{5+}, where convection (in particular, electro-osmotic convection) appears to be the dominant mode of transport for this particular species. The results shown in Fig. 4.3 and 4.4 also depict that for Nafion®, convection plays a deterministic role regarding the change in magnitude of crossover between charge and discharge. When the magnitudes of migration and convection are compared, the migration appears to have

a minimal effect on the net vanadium crossover, as it has a small magnitude and changes direction during charge and discharge. On the other hand, convection is found to occur in the same direction (i.e., always towards positive half-cell) for all species with a magnitude similar to the diffusive transport during discharge. This observation implies that convection may have an impact on the direction and the magnitude of the net crossover in Nafion®, which also explains the observed increase in net crossover during discharge in Fig. 4.2a.

Trends in s-Radel: When the model predictions are compared in Figs. 4.3 and 4.4, one key observation is that diffusive crossover is significantly reduced in s-Radel compared to Nafion® for all vanadium species. This result can be attributed to the lower vanadium permeability and higher vanadium ion selectivity of s-Radel (see Table 4.1). Figs 4.3 and 4.4 also show that migration is almost eliminated in s-Radel membrane for all vanadium species. The suppressed effect of diffusion and migration suggests that convection is the dominant transport mechanism responsible for vanadium crossover in s-Radel. Accordingly, the contribution of the convection to the net crossover is observed to be almost 10 times higher than the contribution of the diffusion in s-Radel. In addition, convection is observed to change direction during charge/discharge as opposed to Nafion®, which is found to be always in the same direction (i.e., towards positive half-cell) regardless of charge or discharge. These observations suggest that the direction and magnitude of convection in s-Radel has important implications on the direction and magnitude of net crossover in a cycle.

4.1.1.3.3 Convective Crossover

The simulation results shown in Fig. 4.3 and 4.4 suggest that convection is an important mechanism of species transport which affects the direction and magnitude of crossover for both membrane types. Especially for s-Radel, convection appears to be the primary mechanism responsible for crossover due to the minimal effect of diffusion. To further investigate the role of convection for these membranes, the convective transport mechanisms, including osmotic and electro-osmotic convection (i.e., electro-osmotic drag), are investigated for these two membrane types. Fig. 4.5 shows the break-down of the convective mass flow rate (i.e., electro-osmotic convection and osmosis) of the electrolyte at 50% SOC of the 40th cycle for both s-Radel and Nafion®.

Trends in Nafion® 117: Fig. 4.5a shows that osmotic convection, which occurs due to the pressure difference across the membrane, governs the direction and magnitude of the net convective transport in Nafion®, since the electro-osmotic convection appears to change direction from charge to discharge while maintaining the same magnitude. In a previous work by Knehr et al. [78], it was observed that the direction and magnitude of osmotic convection depended on the electrolyte viscosities in each half-cell, since the pressure gradient across the membrane is driven by the difference in electrolyte viscosities between half-cells. These viscosities vary based on the electrolyte composition and SOC. Since differently charged species exist in the positive and negative half-cell, it is expected that the electrolytes in the positive and negative half-cells have different viscosities, which results in species transport across the membrane due to hydraulic pressure differences under constant flow rate operation. In the same work [78], it was also observed that the direction of osmotic

convection will always take place from a high pressure region (more viscous electrolyte) to a low pressure region (less viscous electrolyte), which also explains the observed trend of net convective transport towards the positive half-cell in Fig. 4.5a . In these simulations, a higher viscosity was used for the negative half-cell (based on the studies in the literature), which results in net convective transport toward positive half-cell as shown in Fig. 4.5a.

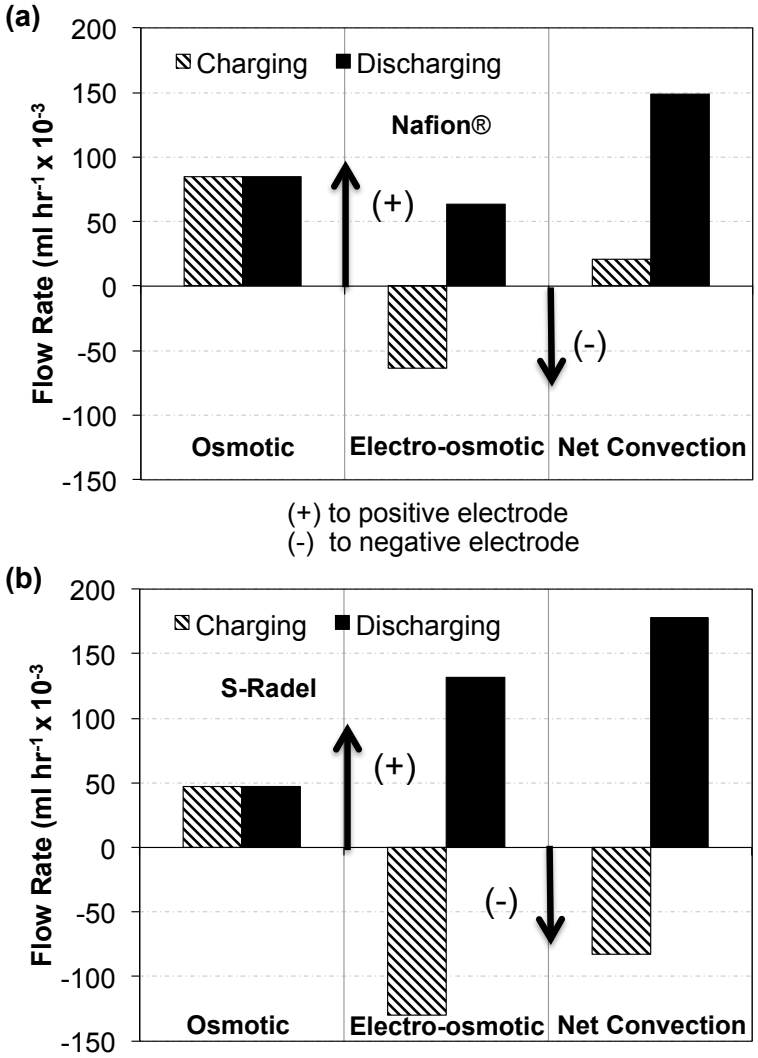

Figure 4.5 Convective mass flow rates of the electrolyte via osmotic and electro-osmotic convection at 50 % state of charge of 40th cycle during both charging and discharging through (a) Nafion® 117, (b) S-Radel.

Trends in s-Radel: Fig. 4.5b shows that the electro-osmotic convection (i.e., electro-osmotic drag), which occurs due to the viscous interaction of the charged species in the membrane, is the dominant mode of convective transport in s-Radel, as it has much larger magnitude than the osmotic convection. Furthermore, the magnitude of the osmotic convection in s-Radel is observed to be lower (almost half) than what is observed for Nafion®. The dominant role of electro-osmotic convection in s-Radel can be attributed to the difference in number of fixed ions between the two membrane types. The number of fixed ions is determined by the fixed acid concentration in the membrane and necessitates the presence of an equal amount of mobile ions to maintain the electroneutrality. The presence of more mobile ions in the membrane results in more viscous interactions, which yields more electro-osmotic convective transport. Although s-Radel has a lower electrokinetic permeability than Nafion®, it experiences more electro-osmosis because it has a higher IEC (i.e., a higher fixed acid concentration). In other words, there are more ions in s-Radel causing drag of vanadium species toward positive or negative electrode depending on the direction of the current.

The observed dominance of electro-osmotic convection in s-Radel also provides insight into the difference in the capacity fade between s-Radel and Nafion®. Electro-osmotic convection occurs always in the direction of the current; therefore it switches directions during charge and discharge, as shown in Fig. 4.5b. In addition, the magnitude of the electro-osmotic convection is directly controlled by the amount of the current drawn in the system. As shown in Figs. 4.3b, 4.3d and 4.4b, 4.4d, the crossover is found to change direction during charge and discharge for s-Radel. This reversal in the direction of crossover between charge and discharge results in

significantly lower “net” crossover for s-Radel as compared to Nafion®. The reversal in the direction of crossover occurs because of the fact that the convection changes direction between charging and discharging, which is primarily governed by the electro-osmotic convection in s-Radel. As such, for a given cycle, during charging electro-osmotic convection opposes osmosis, but during discharging both electro-osmotic convection and osmosis occur in the same direction (Fig. 4.5b), which results in more species crossover during “discharging” and causes the change of the direction of vanadium crossover between charge and discharge in s-Radel (see Figs. 4.3b, 4.3d and 4.4b, 4.4d).

4.1.1.4 Crossover, Efficiency, and Mitigation Strategies

Practical VRFB systems require a high energy density and thus high vanadium concentrations in order to be commercially viable. Unfortunately, these high vanadium concentrations make diffusion across the membrane unavoidable, which can be particularly problematic in diffusion-dominated membranes like Nafion®. In a previous work by Knehr et al. [78], how osmotic convection can be used to mitigate crossover in Nafion® was demonstrated. This strategy was accomplished by controlling the flow rate in each half-cell to reduce the pressure gradient across the membrane, which originates from the differences in the viscosities of the electrolyte solutions in the half-cells. Under ideal conditions, it is possible to control the flow rates, and thus the pressure gradient; in such a way that osmotic convection completely opposes diffusion. This approach is particularly effective for membranes which are diffusion-dominated, since the transport across these membranes tends to occur in the same direction during both charging and discharging.

Conversely, in this study, transport of vanadium in s-Radel was found to be primarily dominated by electro-osmotic convection; thus the direction of vanadium transport depends on the direction of the current. The present study demonstrates that this reversal in the direction of crossover results in significantly reduced capacity fade during cycling, which is due to the reduced net vanadium crossover during each individual cycle. Capacity fade could be further reduced by ensuring that the modes of the convective transport (osmosis and electro-osmotic convection) during charging and discharging are equal in magnitude. One possible approach to accomplish this balance would be to vary the magnitude of the applied current density between charging and discharging based on the electro-osmotic behavior of the membrane in order to obtain zero net flux of vanadium.

Theoretically, both of these techniques (controlling the pressure gradient or varying the current density) can be applied based on the membrane of interest to ensure that the vanadium concentration in each half-cell remains constant during operation. It is important to note that while these techniques may eliminate capacity-fade due to concentration imbalances, they do not necessarily minimize losses in coulombic efficiency due to the crossover of vanadium. Thus, they do not necessarily make the system more efficient. It is important to note that capacity fade should not be treated the same as coulombic efficiency. Any time when a vanadium ion crosses the membrane, it essentially causes a ‘chemical short circuit’, and the stored charge is lost, which lowers the coulombic efficiency. Conversely, the capacity fade is primarily affected by imbalances in volume or concentration between the two half-cells at the end of each cycle. For instance, s-Radel has a lower capacity fade because convection ‘switches direction’ between charging and discharging, resulting in “less” net

crossover during each single cycle. However, at all times during the cycle, vanadium is still moving to the opposite side of the membrane and causing side reactions, which will decrease the system's coulombic efficiency. So, even if the vanadium transport during charging is exactly equal and in the opposite direction of the transport during discharging (i.e. capacity fade is zero), the cell will still not have 100% coulombic efficiency. Therefore, to maximize the coulombic efficiency, the instantaneous transport of vanadium across the membrane during charging and discharging should be minimized, which requires further control of the specific transport properties of the membrane.

4.1.1.4 Conclusion

In this study, species transport mechanisms governing capacity loss in s-Radel and Nafion® 117 membranes were investigated using an experimentally validated, 2-D, transient VRFB model, which incorporates the species transport across the membrane due to migration, diffusion and convection. Model simulations show that species transport in Nafion® is governed by diffusion, whereas convection is found to be the dominating transport mechanism responsible for vanadium crossover in s-Radel due to the lower vanadium permeability of s-Radel. Among the convective transport modes, transport of vanadium in S-Radel is found to be primarily dominated by electro-osmotic convection due to the higher fixed acid concentration and corresponding free moving ions in s-Radel. Furthermore, vanadium crossover in s-Radel is found to switch direction during charge and discharge due to the change in direction of convection between charge and discharge. This reversal in the direction of crossover is found to result in significantly lower "net" crossover for s-Radel when compared to Nafion®.

Based on these observed trends, this section highlights two important observations. First, comparison of these two membranes indicates that the hydraulic and the electro-kinetic permeability of a membrane are equally as important as vanadium diffusion characteristics, when evaluating new membranes for VRFB applications. Second, the results of this study suggest that the lifetime of a VRFB can be extended by minimizing imbalances of species concentration between half-cells during cycling. However, this balancing may not necessarily render the system more efficient. Along with the lifetime, to maximize the coulombic efficiency, the instantaneous transport of vanadium across the membrane during charge and discharge should be minimized, which requires further control of the specific transport properties of the membrane.

4.1.2 Anion Exchange Membranes (AEMs)

As explained in the previous section (Section 4.1), the majority of the current research on VRFB membranes aims to develop proton exchange membranes (PEMs) that feature simultaneously high proton conductivity, low vanadium permeability, and long lifetime. VRFBs with over 99% coulombic efficiency (CE) were obtained by strategic tuning of the membrane's chemical structure and properties [77], however, the capacity fade of these batteries during long term operation can not be ignored because of vanadium cation crossover through this type of cation exchange membrane. Nanofiltration membranes that selectively transfer protons compared to vanadium ions by size exclusion was proposed as a new type of separator for VRFBs and 98% CE was achieved after optimization [65]. While these membranes have proven their usefulness for high performance cells, it would be highly desirable to have a minimal or zero capacity fade devices.

Anion exchange membranes (AEMs) have been well-understood to be able to block the transport of cations due to Donnan repulsion effects and were thus widely used in electrodialysis technologies [79]. Preliminary evaluations of AEMs in VRFB were reported with CE of as high as around 99%, however, very limited information was given regarding the operation principle of the AEMs and their detail cell performance [80-81]. It is generally recognized that protons are the charge-carriers passing through the separator of VRFBs to balance the anode and cathode charge during operation. In fact, any ion, such as sulfate in a sulfuric acid-based electrolyte, or chloride in a hydrochloric acid-based electrolyte, can be the charge carrier to balance the redox reactions of the vanadium species. For this reason the objective of this section is to explore the fundamental properties of AEMs as potentially no capacity fade separators for VRFBs. The recent success in employing an AEM in VRFB to get 100% CE under various current densities were reported. This part of the dissertation work on AEMs in VRFB was collaborated with Dr. Hickner's Group at the Pennsylvania State University.

4.1.2.1 Performance Characteristics of AEMs in VRFBs

4.1.2.1.1 Method of Approach

Quaternary ammonium functionalized poly(fluorenyl ether) (QA-PFE) with an ion exchange capacity of 2.0 mequiv. g^{-1} was synthesized by our collaborators at the Pennsylvania State University according to the procedure reported in the literature [82]. The AEM based on QA-PFE was cast from 8 wt.% solution in N,N'-dimethylacetamide on a glass plate at 80 ºC under atmospheric pressure for 24 h. The AEM was ion-exchanged to the SO_4^- anion form in 1 M Na_2SO_4 solution for 24 h, and then immersed in deionized water for 24 h three fresh water changes. The AEM

(thickness of 56 μm) was used for performance evaluation in a VRFB device. For comparison, Nafion® N212 was examined under the same conditions.

Ionic conductivity was measured by two-probe electrochemical impedance spectroscopy (EIS) using a Solartron 1260A frequency response analyzer [83]. The VO^{2+} permeability measurements were conducted in a membrane-separated cell by filling vanadium solution into one reservoir and vanadium-blank solution into another reservoir using the standard procedure reported in the literature [77]. VRFB cell performance measurements were conducted with 100 mL of 1 M $VOSO_4$ + 2.5 M H_2SO_4 solution in the positive electrolyte tank and 50 mL of 1 M $VOSO_4$ + 2.5 M H_2SO_4 solution in the negative electrolyte tank. The cell configuration was the same as reported in Section 2.2.2 [84]. The cell was first charged to 1.7 V and discharged to 0.7 V at the current density of 80 mA cm^{-2}, and then cycled at this current density for 15 cycles and finally charged-discharged at 60, 40 and 20 mA cm^{-2} with pre-discharging at the corresponding current density before the final charging-discharging process. The coulombic efficiency (CE), voltage efficiency (VE) and energy efficiency (EE) for any galvanostatic charging-discharging process were calculated from:

$$CE = \frac{t_d}{t_c} \times 100\% \tag{4.1}$$

$$VE = \frac{V_d}{V_c} \times 100\% \tag{4.2}$$

$$EE = CE \times VE \tag{4.3}$$

where t_d is the discharging time, t_c is the charging time, V_d is the average discharging voltage, V_c is the average charging voltage.

4.1.2.1.2 Results and Discussion

4.1.2.1.2.1 Operating Principles of AEMs in VRFBs

Generally, AEMs are notorious for their low conductivity compared to PEMs due to the high mobility of protons compared to other ions in solution. Indeed, the proton conductivity of N212 at room temperature was found to be 69 mS cm^{-1} while the SO_4^{2-} conductivity of the AEM at room temperature was only 5 mS cm^{-1}. This difference in ionic conductivity poses a critical challenge to deploy AEMs as alternatives to PEMs for electrochemical applications. Fortunately, the high concentration of SO_4^{2-} in the electrolytes of VRFBs mitigates the low conductivity of AEMs due to uptake of free SO_4^{-} ions into the membrane. Furthermore, the existence of protons in the anolyte and catholyte may also help lower the resistance of AEMs. To support these ideas, we measured the conductivity of N212 and the experimental AEM after equilibration in 1 M $VOSO_4$ + 2.5 M H_2SO_4 solution for 24 h. The apparent conductivity of N212 was 44 mS cm^{-1}, lower than its proton conductivity in pure water. This difference can be rationalized by considering that some of the proton sites were occupied by vanadium ions which had much lower mobility. Also, increased acid concentration has been observed to decrease the conductivity of solutions and membranes [85-86]. Interestingly, under these conditions the measured conductivity of the AEM had increased to 20 mS cm^{-1}, almost half of the conductivity of N212, making it promising for practical applications.

The transport properties of vanadium ions through the AEM and N212 were investigated by measuring their VO^{2+} permeability. For N212, the permeation of VO^{2+} could be visually observed by the change of the vanadium deficient solution from clear to blue within 1 h. The VO^{2+} permeability of N112 was calculated to be

3.2×10^{-12} m^2 s^{-1}, similar to literature values [16]. For the AEM, there was no solution color change after one month measurement time and also no detectable VO^{2+} ion by UV-vis analysis. This absence of VO^{2+} crossover indicated that the AEM has excellent capability to repulse the transport of vanadium ions. Therefore, the AEM in a VRFB can transport both proton and sulfate ions but retains vanadium ions, as depicted in Fig. 4.6.

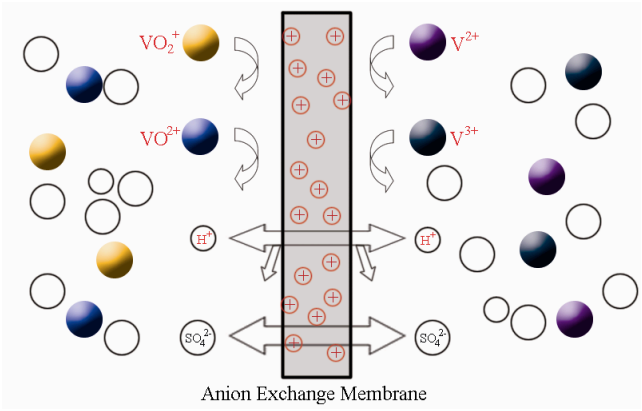

Figure 4.6 Functions of an AEM in a VRFB.

4.1.2.1.2.2 VRFB Performance under Different Current Densities

The charge-discharge curves of VRFBs assembled with AEM or N212 membranes at the current density of 20 mA cm^{-2} are shown in Fig. 4.7. The VRFB assembled with N212 had lower charge voltage than the VRFB assembled with the quaternary ammonium functionalized poly(fluorenyl ether) AEM. This difference in charge voltage was attributed to the lower resistance of N212 as discussed above since both membranes had similar thickness. The average discharge voltage for both the VRFBs were similar even though the discharge curve of the VRFB assembled with N212 was slightly lower than the discharge curve of the VRFB assembled with the AEM. Since N212 had lower resistance, its corresponding VRFB was expected to afford higher average discharge voltage than the AEM counterpart. Nevertheless, N212 suffered

from large vanadium permeation resulting in certain amount of short-circuit reactions, which negatively affected the discharge voltage and thus offset its lower resistance.

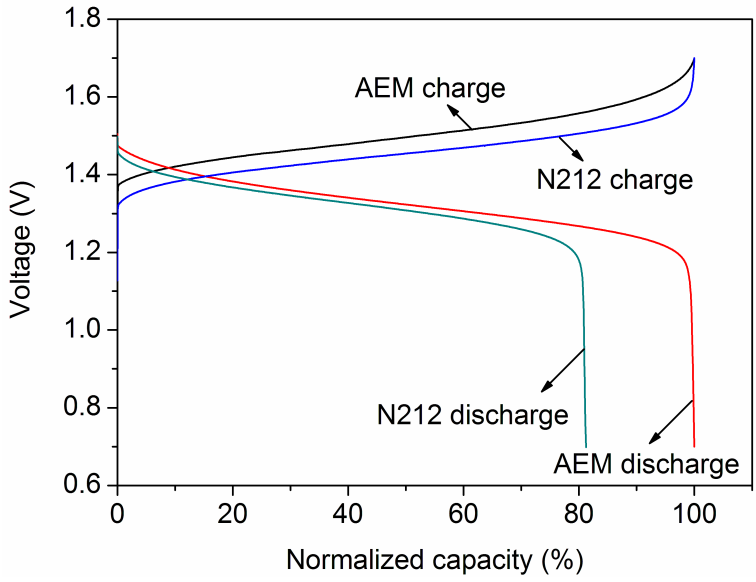

Figure 4.7 Charge-discharge curves of VRFBs at 20 mA cm^{-2}. The membranes used in the VRFBs are indicated in the figure.

The coulombic efficiency (CE) of the VRFB assembled with N212 at this current density was 81.2%, similar to literature values [87]. Surprisingly, the CE of the VRFB assembled with the AEM was 100%, or as near to 100 % as we could measure, suggesting there was no vanadium crossover or side reactions during cell operation. Generally, the CE of a VRFB is influenced by vanadium permeation, electrode corrosion, and side reactions of vanadium ions with oxygen or other solution contaminants. For this experiment, the upper limit of charging voltage was kept to 1.7 V, which has been shown to avoid corrosion of the electrodes [88]. Furthermore, electrolyte tank was sealed and purged with inert N_2 gas carefully to eliminate side reactions of vanadium ions. Together with the undetectable vanadium permeation of

the AEM, it is reasonable to achieve 100% CE, which paves the way for very high efficiency VRFBs under a wide range of conditions, even during long periods of test.

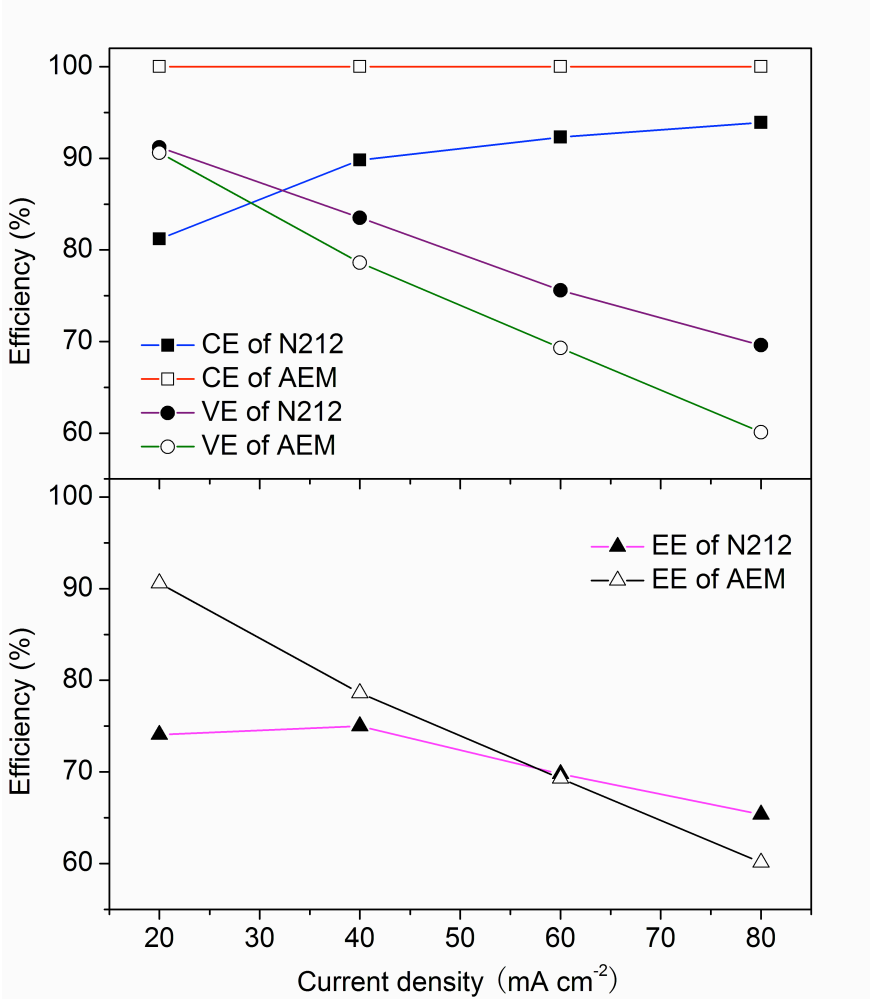

Figure 4.8 Coulombic efficiency (CE), voltage efficiency (VE) and energy efficiency (EE) of VRFBs at various current densities. The membranes used in the VRFBs are indicated in the figure.

The influence of current density on coulombic efficiency (CE), voltage efficiency (VE) and energy efficiency (EE) of the VRFBs are shown in Fig. 4.8. It can be seen that the VRFB assembled with AEM achieved 100% CE for all the current densities tested. The CE of the VRFB assembled with N212 increased with increasing current density, which was due to the decreased time allowed for vanadium permeation. The

VE of both the VRFBs decreased with the increasing current density because of the higher ohmic polarization at higher current densities. The VRFB with the N212 separator had a more pronounced advantage in VE with increasing current density as compared to the VRFB assembled with AEM, suggesting a larger influence of membrane resistance at higher current densities, as expected. The EE of the VRFB assembled with the AEM decreased monotonically from 20 mA cm^{-2} to 80 mA cm^{-2} due to the decreasing VE, while the EE of the VRFB assembled with N212 exhibited a peak value at 40 mA cm^{-2} which was the combination effect of its CE and VE. It is worthwhile to mention that the VRFB assembled with the AEM had higher energy efficiency than the VRFB assembled with N212 at current densities lower than 60 mA cm^{-2}, making it highly desirable for medium/low current density VRFB developments.

4.1.2.1.2.3 VRFB Cycling Performance

Capacity change and CE change versus cycle number were investigated in VRFB cycling tests, Fig. 4.9. Capacity fade of the VRFB assembled with N212 was observed, while the VRFB assembled with the AEM showed no measureable capacity fade. This observation correlated well with no vanadium crossover or no self-discharge in the VRFB assembled with the AEM and was in good agreement with the 100% CE of the battery. The absence of capacity fade guaranteed maintenance-free operation of the VRFB, which has not been met so far in other separator work. The CEs of the VRFBs were very stable during the cycling, Fig. 4.9. This phenomenon is typical in flow battery systems as long as there is no materials damage during device operation.

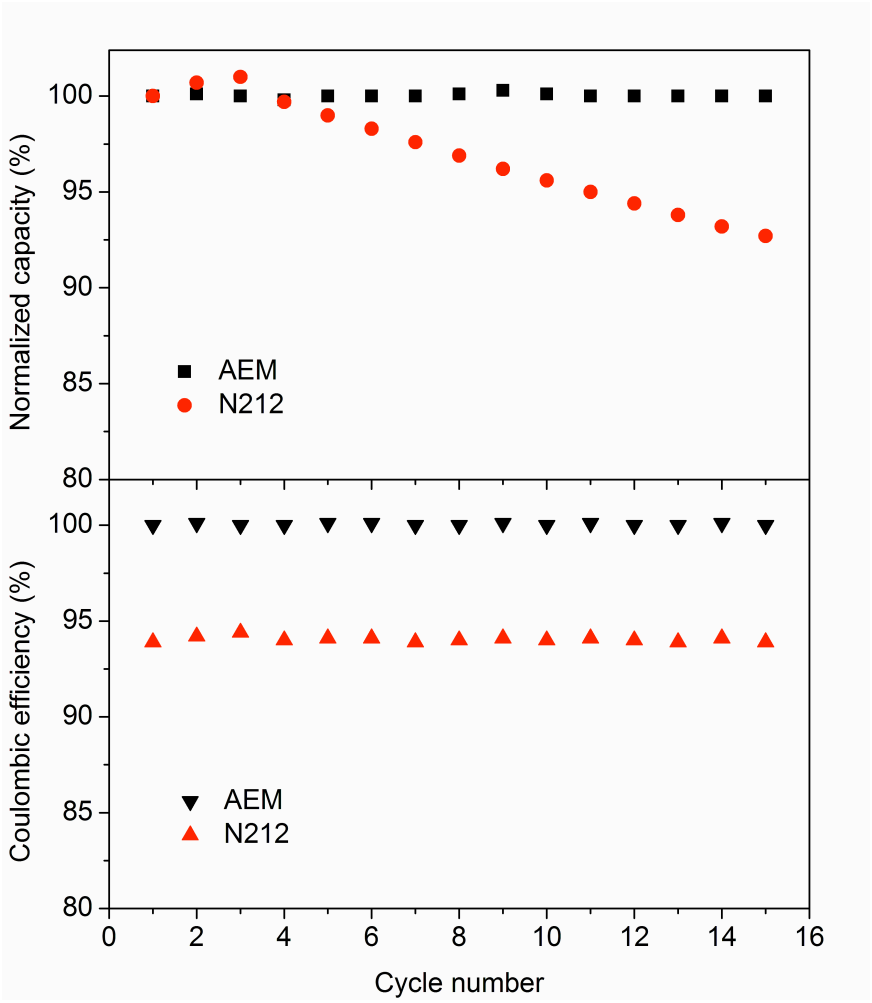

Figure 4.9 Normalized capacity changes and coulombic efficiencies of VRFBs in the cyling test. The membranes used in the VRFBs are indicated in the figure.

4.1.2.1.3 Conclusions

A quaternary ammonium functionalized poly(fluorenyl ether) AEM has been applied successfully as a separator in VRFB devices. The AEM had low intrinsic anionic conductivity, but upon soaking in VRFB electrolyte solution achieved almost half the conductivity of N212 under the conditions encountered in a flow cell. Furthermore, the VO^{2+} permeation of the AEM was undetectable over the course of a month while vanadium ion permeation of N212 was observed within 1 h and verified using UV-vis measurements. Moderate ion conductivity and extremely low vanadium ion

permeability qualified the AEM for device testing in a VRFB which was then characterized by charge-discharge and cycling performance. It was found that the VRFB assembled with this AEM achieved 100% coulombic efficiency at all the current densities tested which has not been reported previously. The energy efficiency of this VRFB was higher than that of a VRFB assembled with N212 when the current density was lower than 60 mA cm^{-2}. Capacity fade was observed for the VRFB assembled with N212 while it was absent for the VRFB assembled with AEM.

4.1.2.2 Effects of Ion Exchange Capacity of AEMs on VRFB Performance

In the second part of the AEM study, the effect of ion exchange capacity on single-cycle and long-term performance of VRFB is investigated using the AEMs with three different ion exchange capacities (IECs).

4.1.2.2.1 Introduction

AEMs contain tethered positively charged groups such as quaternary ammonium or pyridinium that can repulse vanadium cations, a membrane phenomenon known as, Donnan exclusion, resulting in extremely low vanadium cation permeation [62,89]. The sulfate anion (in the case of H_2SO_4-based electrolytes) or other anion in the electrolyte of the VRFB is the major charge carrier in this case, while the proton can be a minority charge carrier due to imperfect Donnan exclusion of the membrane [90-91]. The concept of using the electrostatic repulsion or Donnan repulsion to block the crossover of vanadium ions can also be found in polycation-polyanion layer-by-layer composites [51] or amphoteric membranes [92], where much higher coulombic efficiency and much lower self-discharge rate were obtained as compared to VRFBs employing Nafion® separators. While high-exclusion membranes have been

demonstrated in VRFBs recently, detailed information on the influence of the membrane composition and transport properties of AEMs and their relationship with the cell performance still needs to be sought to optimize these separator systems.

The vanadium crossover through the membrane in a VRFB is extraordinarily important as vanadium contaminants of the wrong valence in the anolyte or catholyte will accumulate during prolonged charge-discharge cycling. Therefore, low vanadium permeability AEMs appear to be one of the most promising candidates for use as ion-exchange separators in VRFBs. In order to develop high performance membranes for VRFBs, herein, quaternary ammonium randomly functionalized poly(arylene ether sulfone)s (Radel®) with IECs from 1.7 to 2.4 mequiv g^{-1} were synthesized and the membranes were examined for their fundamental physicochemical properties as well as their detailed VRFB performance.

4.1.2.2.1 Method of Approach

4.1.2.2.1.1 Membrane Preparation

All membranes used in this section were synthesized by our collaborators at the Penn State University. For the sake of the readers a brief explanation about membrane preparation is given. The quaternary ammonium functionalized Radel samples were dissolved in N,N'-dimethylacetamide solution at approximately 8 wt./vol.% and then cast onto glass plates and dried at 80 ºC under atmosphere pressure for 24 h. The cast membranes were then peeled from the glass plate and immersed in 1 L of 1 M Na_2SO_4 solution for 24 h, followed by immersion in deionized water for 24 h with three DI water changes. The membranes were stored in deionized water until use.

4.1.2.2.1.2 Membrane Characterization

Membrane Characterization: The water uptake of the membranes was defined as weight ratio of the absorbed water to that of the dry membrane. The swelling ratio was described as the linear expansion ratio of the hydrated membrane compared to its dry state. Ionic conductivity was measured by two-probe electrochemical impedance spectroscopy (EIS) using a Solartron 1260A frequency response analyzer [83]. Samples were equilibrated in a large excess of 1.4 M $VOSO_4$ + 2.0 M H_2SO_4 solution for 24 h before the impedance measurement. The VO^{2+} permeability measurements were conducted in a membrane-separated cell by filling vanadium solution into one reservoir and vanadium-blank ionic solution of the equivalent ionic strength to the vanadium solution into another reservoir using the standard procedure reported in the literature [77]. The amount of the vanadium permeated was detected by UV-vis spectroscopy using a Shimadzu spectrophotometer (UV-2600/2700).

Cell Performance: The VRFB setup, the starting electrolyte concentration and charge/discharge procedure were the same as reported in Section 4.1.2.1.1 [84,93]. Similarly, nitrogen was purged to the electrolyte tanks to protect the vanadium species from oxidation. For polarization curve measurements, the current was scanned with the lower limit voltage of 0.2 V to determine the end of the polarization curve. The VRFBs were first fully charged at 80 mA cm^{-2}, then the discharge current was scanned from 0 A to 700 mA cm^{-2} with steps of 10 mA cm^{-2}. The hold time at each step was 30 s. The cell potential after 30 s was recorded and plotted against current density.

4.1.2.2.2 Results and Discussion

4.1.2.2.2.1 Membrane Synthesis and Properties

Membranes with thicknesses in the range of 55-60 μm were obtained by solution casting. The basic membrane properties are listed in Table 4.3. The water uptake and swelling ratio increased monotonically with increasing IEC. These increases were attributed to the higher degree of hydrophilicity of the samples with greater IEC. The ionic conductivity of the samples increased as well with the increase in IEC. It was worthwhile to point out that the QA-Radel-2.4 sample showed much higher water uptake and swelling ratio than the other two IEC samples, while its conductivity only showed a small increase. Thus, pushing the IEC to higher levels is not necessarily desirable as poor mechanical properties and large crossover can result due to the increased swelling. In membrane VO^{2+} permeability measurements, Table 4.3, the QA-Radel-2.4 sample exhibited large values similar to Nafion® (3.2×10^{-12} m^2 s^{-1}), which is not optimal due to severe self-discharge during cell operation.[12] The VO^{2+} permeability of the QA-Radel-2.0 membrane was more than one order of magnitude lower than that of the QA-Radel-2.4 sample. VO^{2+} permeation across the QA-Radel-1.7 membrane was not detected during a one-week permeation experiment. The promisingly low vanadium permeability of the QA-Radel-2.0 and QA-Radel-1.7 samples was likely due to the Donnan exclusion of vanadium cations by the positively charged quaternary ammonium groups in the membrane. The large swelling of the QA-Radel-2.4 decreased the ionic concentration in the sample and lowered the effective Donnan potential. By taking into account the gravimetric IEC and the water swelling and density of the membranes, the calculated ion concentrations in the samples were 1.7 mequiv. cm^{-3}, 1.8 mequiv. cm^{-3} and 1.5 mequiv. cm^{-3} for QA-Radel-

1.7, QA-Radel-2.0 and QA-Radel-2.4, respectively, which supports a lower Donnan potential in the QA-Radel-2.4 sample.

Table 4.3 Physical properties of QA-Radel membranes and Nafion® N212.

Sample	Water uptake (%)	Swelling ratio (%)	Conductivity (mS cm^{-1})	VO^{2+} permeability (m^2 s^{-1})
QA-Radel-1.7	16	7	24	-
QA-Radel-2.0	29	12	41	3.7×10^{-14}
QA-Radel-2.4	73	23	49	2.9×10^{-12}
N212	28	14	69	3.2×10^{-12}

4.1.2.2.2.2 Cell Performance

The charge-discharge curves of the VRFBs assembled with different IEC QA-Radel membranes for a range of current densities are shown in Fig. 4.10. The cell assembled with the QA-Radel-2.4 membrane had the shortest charge and discharge times among the three VRFB membranes tested, while the VRFB assembled with the QA-Radel-2.0 membrane had the longest charge and discharge times. The charge/discharge times under any given current density dictates the available charge/discharge capacities. For the VRFB assembled with the QA-Radel-2.4 membrane, the high VO^{2+} permeability of the membrane lead to significant crossover of the vanadium electrolytes, resulting in the lowest charge/discharge capacity of the cells tested. For the VRFB assembled with the QA-Radel-1.7 membrane, the low VO^{2+} permeation of the membrane was associated with the lowest ionic conductivity among the three QA-Radels, causing the highest ohmic polarization of the batteries and therefore the lowest utilization efficiency of the active vanadium electrolyte species. The

combination of the low VO^{2+} permeability and low ionic conductivity of QA-Radel-1.7 rendered a battery with intermediate charge and discharge capacities compared to the other two membrane samples. The QA-Radel-2.0 membrane turned out to be the best membrane in this study for the VRFB application, suggesting that there was an optimal relationship between VO^{2+} permeability and ionic conductivity for the AEM samples in VRFBs. It can also be seen in Fig. 4.10 that with increasing current density, the charge voltage increased while the discharge voltage decreased for all the VRFBs. This difference was attributed to the higher ohmic polarization of the batteries at higher current density. The charge/discharge times decreased as the current density was raised, as expected due to the fixed amount of electrolyte in the cell.

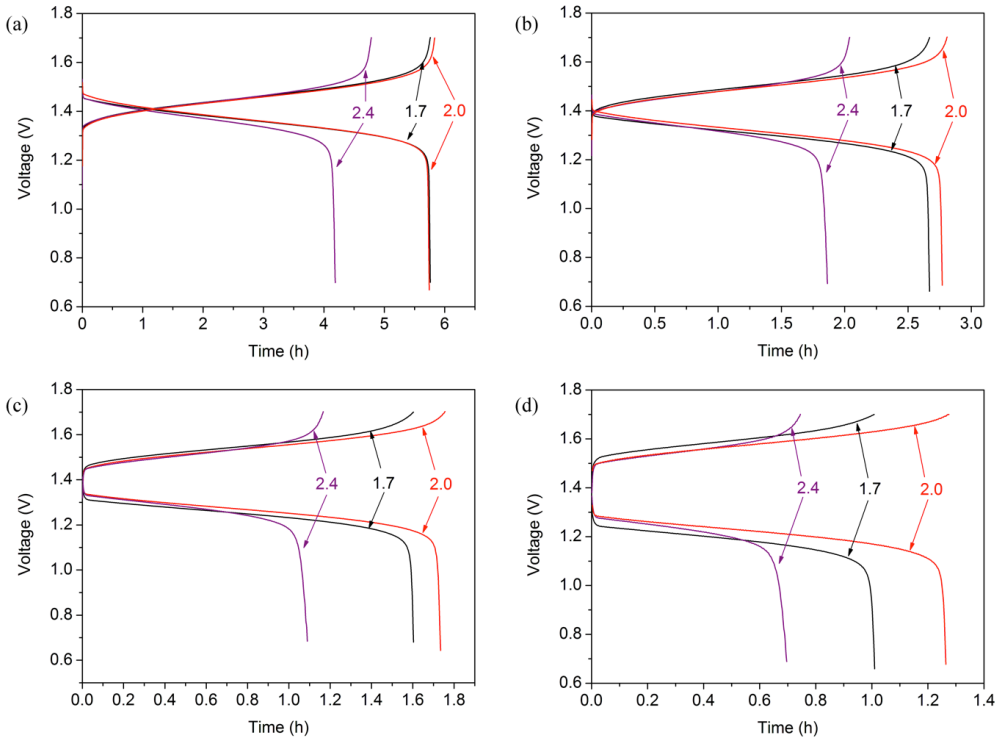

Figure 4.10 Charge-discharge curves of the VRFBs assembled with different QA-Radel membranes at 20 mA cm^{-2} (a), 40 mA cm^{-2} (b), 60 mA cm^{-2} (c) and 80 mA cm^{-2} (d). The numbers in the figures represent the IECs of the membranes.

The coulombic efficiencies (CEs) of the VRFBs at different current densities are shown in Fig. 4.11. It can be seen that the VRFB assembled with the QA-Radel-1.7 membrane had the highest CEs while the VRFB assembled with the QA-Radel-2.4 membrane had the lowest CEs under all the current densities, in good agreement with the VO^{2+} permeability results. CE describes the efficiency of round-trip storage and release of electrons from the cell redox reactions. The vanadium ion crossover and unwanted side reactions, such as electrode corrosion that consumes electrons or ions, may cause coulombic losses. Since the VRFBs tested were of identical construction except the IECs of the membrane separators, the possible side reactions during charge/discharge processes should be similar for all experiments in this study. Therefore, the ion crossover became the dominant factor that determining the relative CEs of the VRFBs. This explains why the CE decreased with the increasing VO^{2+} permeability of the membranes used in the VRFBs. With an increase in current density, the CEs increased monotonically. This increase in CE was attributed to the shorter time for vanadium crossover at higher current density during the charge/discharge processes since the cycle time was significantly decreased. The CE of the VRFB assembled with the QA-Radel-1.7 membrane at 80 mA cm^{-2} was nearly 100%, similar to results reported in Section 4.1.2.1, partially fluorinated AEM exhibits extremely low vanadium crossover [59]. This result suggested that the possible side reactions such as V^{5+} oxidation of the polymeric membrane or the carbon-based electrodes were minimal under the operational conditions of the cells in this work and the losses approached the instrumental error from small fluctuations of the applied currents during the galvanostatic charge/discharge processes.

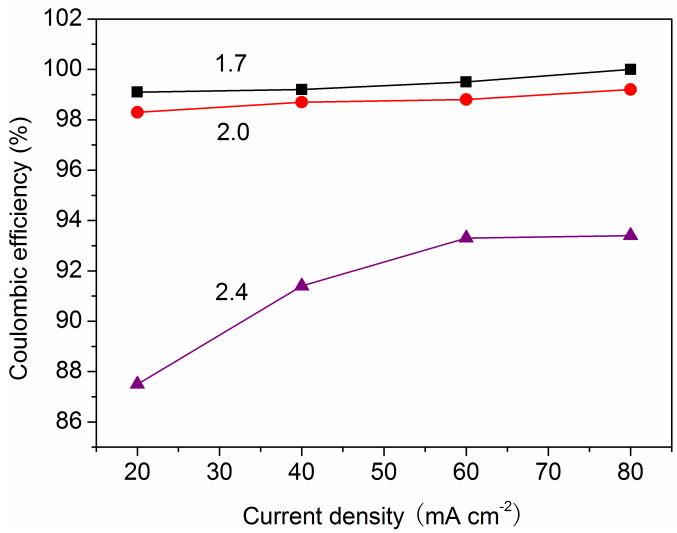

Figure 4.11 Coulombic efficiencies of the VRFBs as a function of current density.

The voltage efficiencies (VEs) of the VRFBs at different current densities are shown in Fig. 4.12. The VE increased with increasing IEC of the membrane used in the VRFB over all current densities tested, consistent with the membranes' trend in ionic conductivity. Therefore, increasing the IEC of the membrane was advantageous for the VE of the VRFBs while it was detrimental to the CE of the batteries. A further increase of the IEC beyond 2.4 mequiv g^{-1} may result in reduced VE due to large crossover voltage loss, which was not addressed in this study [90]. With the increase in current density, the VE for all the VRFBs decreased gradually due to the increasing ohmic polarization loss of the cells. It can be seen in Fig. 4.12 that the VE difference for the three VRFBs was only a few percent, while the ionic conductivity of the QA-Radel membranes varied by more than two times. This result suggested that the resistance of the membrane was not the main contribution to the total resistance of the cells in this study.

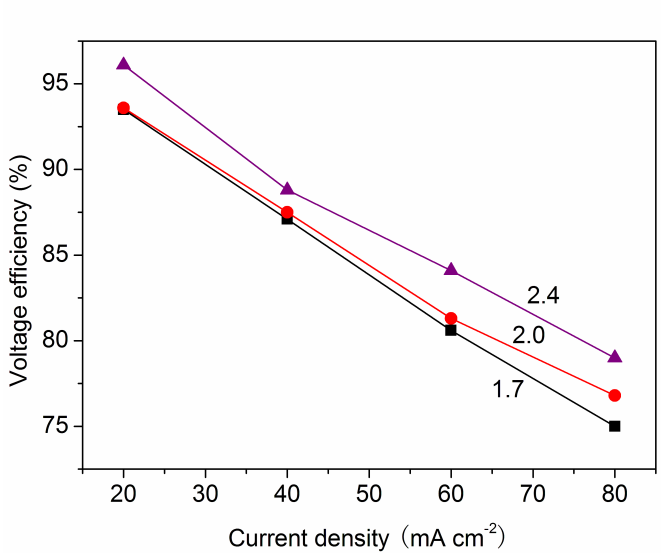

Figure 4.12 Voltage efficiency of the VRFBs as a function of current density.

The product of CE and VE is energy efficiency (EE), which is used to describe the ratio of the output and input energy of the cell. Self-discharge (vanadium crossover), side reactions and polarization are the main sources of energy loss in VRFBs [16]. From Fig. 4.13 it can be seen that the VRFB assembled with the QA-Radel-2.4 membrane had the lowest EE at all the current densities tested. The VRFB assembled with the QA-Radel-1.7 membrane had the highest EE at low current densities (20 mA cm^{-2} and 40 mA cm^{-2}) while the VRFB assembled with the QA-Radel-2.0 membrane had the highest EE at high current densities (60 mA cm^{-2} and 80 mA cm^{-2}). Therefore, membranes with high VO^{2+} permeability such as QA-Radel-2.4 are not suitable for VRFBs; membranes with low VO^{2+} permeability and low ionic conductivity such as QA-Radel-1.7 are promising for VRFBs operated at low current densities; and membranes with low VO^{2+} permeability and high ionic conductivity such as QA-Radel-2.0 are promising for VRFBs operated at high current densities. From Fig. 4.13 it can also be observed that the EE was highly dependent on the working current density. The EEs of all the three VRFBs decreased gradually as the current density

was increase from 20 mA cm^{-2} to 80 mA cm^{-2}. These EEs were higher than the reported EEs of VRFBs based on proton exchange membranes [19,94], and comparable to the EEs of the VRFBs based on the other AEMs [92].

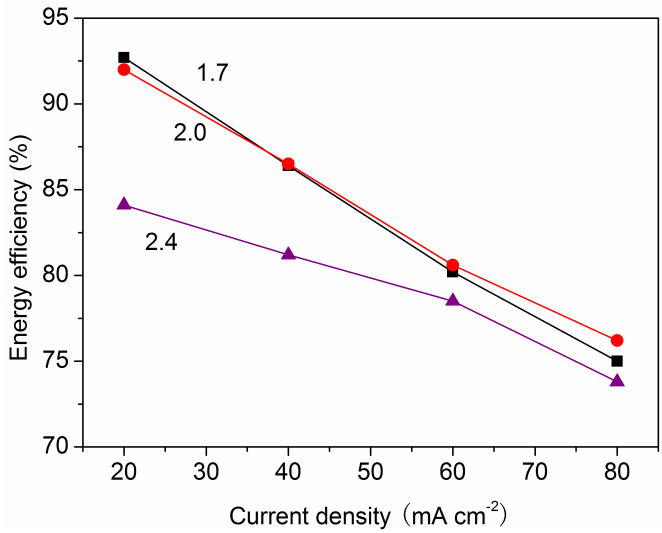

Figure 4.13 Energy efficiencies of the VRFBs as a function of current density.

The influence of the membrane IEC on the cycling performance of the VRFBs was investigated. As shown in Fig. 4.14, the initial capacities of the VRFBs varied due to the different charge/discharge times at the same current density in Fig. 4.10, which also gave a different utilization rate of the vanadium species or charge depth of the batteries. During cycling, the capacity of the VRFB assembled with the QA-Radel-1.7 membrane exhibited the lowest decline in capacity while the capacity of the VRFB assembled with QA-Radel-2.4 decayed most rapidly, as is consistent with the CE of the single cell performance where the VRFB assembled with the QA-Radel-1.7 membrane had the highest CE while the VRFB assembled with QA-Radel-2.4 had the lowest CE. The IEC of the QA-Radel samples influenced the VO^{2+} permeability of the membranes, which was reflected in the CE of the VRFBs in the cell output performance and on the capacity fade of the VRFBs in cell cycling tests. In the

normalized capacities of the VRFBs during cycling tests, Fig. 4.15, it is clear that the rate of capacity fade increased with increasing membrane IEC. After 15 cycles, the capacity of the VRFB assembled with a QA-Radel-2.4 membrane maintained 72.7% of its initial capacity while the capacity of the VRFB assembled with QA-Radel-1.7 maintained 98.3% of its initial capacity. Therefore, careful control of the membrane IEC was critically important for cycling cell performance.

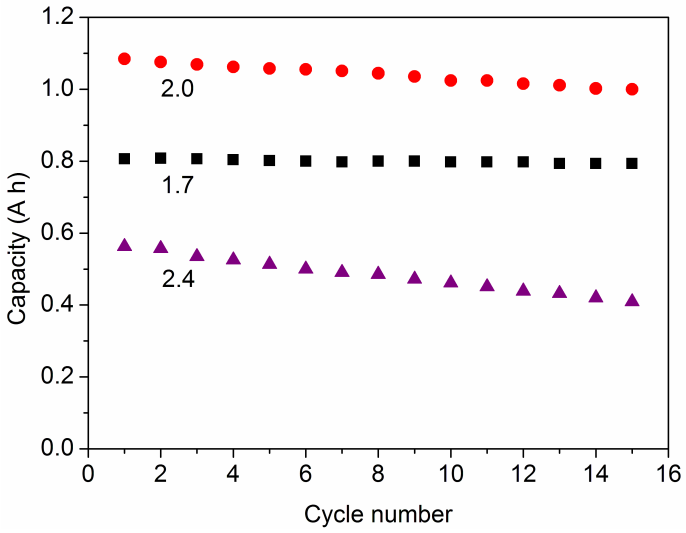

Figure 4.14 Cycling capacities of the VRFBs as a function of cycle number at 80 mA cm^{-2}.

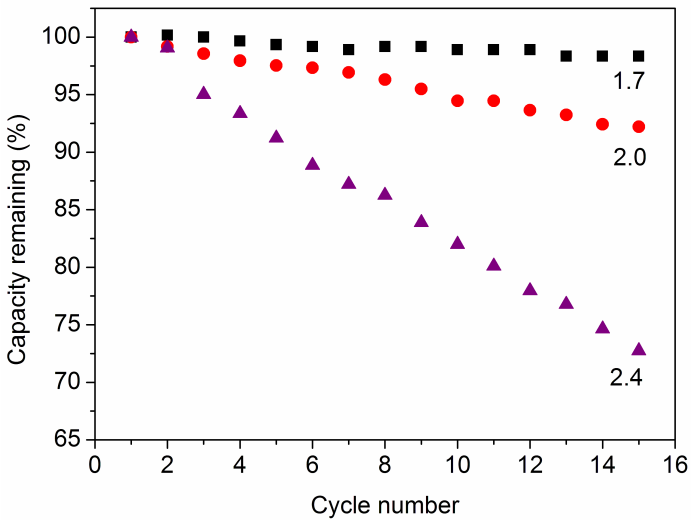

Figure 4.15 Normalized cycling capacities of the VRFBs as a function of cycle number

The polarization curves of the VRFBs assembled with the QA –Radel samples are shown in Fig. 4.16, with the polarization curve of the VRFB assembled with Nafion® N212 membrane for comparison. It can be seen that the voltage of the VRFB assembled with the QA-Radel-2.4 membrane showed slightly poorer performance than the VRFB assembled with N212. The voltage of the VRFB assembled with the QA-Radel-1.7 membrane maintained higher current density than that of the VRFB with a N212 separator, while the voltage of the VRFB with the QA-Radel-2.0 membrane displayed the highest current density (420 mA cm^{-2}). The discharge voltage of the VRFB can be represented as $V = E - \Delta V_{act} - \Delta V_{ohm} - \Delta V_{trans} - \Delta V_{cross}$, where E is the theoretical open circuit voltage of the cell, ΔV_{act} is the voltage loss caused by activation, ΔV_{ohm} is the voltage loss caused by ohmic loss (or iR loss where i is current and R is resistance), ΔV_{trans} is the voltage loss caused by mass transport and ΔV_{cross} is the voltage loss caused by electrolyte crossover. The properties of the membrane have a direct impact on the terms of ΔV_{ohm} and ΔV_{cross} though membrane resistance and VO^{2+} crossover, respectively. Therefore, the QA-Radel-2.0 sample had the best balance of properties for high current density operations. The highest power density achieved for these VRFBs was 218 mW cm^{-2}, which was obtained at the current density of 270 mA cm^{-2} using QA-Radel-2.0 membrane. While this performance was lower than the highest reported power density of the VRFB using IEC- and thickness-optimized proton exchange membrane in the literature [93], this result still was higher than the maximum power density of the VRFB assembled with N212 and demonstrated good prospects for employing anion exchange membranes in VRFBs.

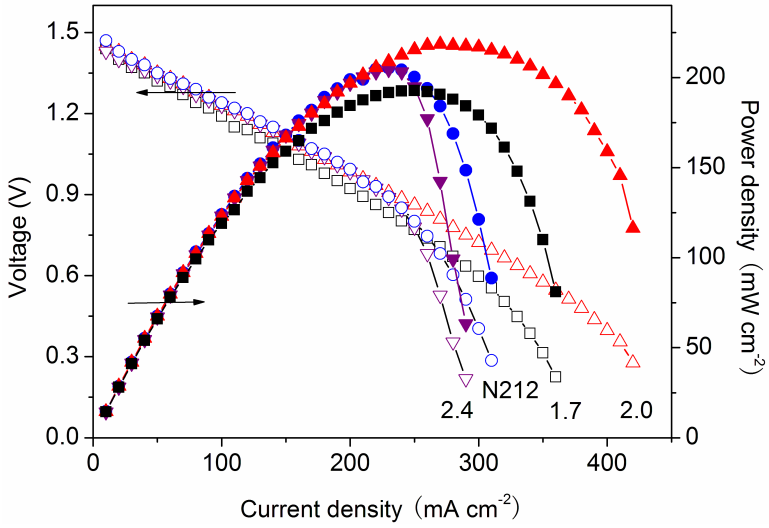

Figure 4.16 Polarization curves and power densities of the VRFBs as a function of current density.

4.1.2.2.3 Conclusions

Quaternary ammonium functionalized Radel® (QA-Radel) membranes with three different IECs of 1.7, 2.0 and 2.4 mequiv. g^{-1} were synthesized and evaluated in the VRFBs. The ionic conductivity of QA-Radel samples after equilibration in 1.4 M $VOSO_4$ + 2.0 M H_2SO_4 solution was of the same order as that of an electrolyte-equilibrated Nafion® N212 membrane, while the VO^{2+} permeability of the QA-Radel samples was significantly lower than that of N212 except the QA-Radel with an IEC of 2.4 mequiv. g^{-1}. Increasing the IEC of the QA-Radel samples increased both the ionic conductivity and the VO^{2+} permeability of the membranes. The ionic conductivity of the membranes influenced the voltage efficiency of the battery while the VO^{2+} permeability of the membranes affected the coulombic efficiency of the cells. It was found that the VRFB assembled with the QA-Radel-1.7 membrane had the highest energy efficiency at 20 mA cm^{-2} and 40 mA cm^{-2} charge/discharge current densities, while the VRFB assembled with the QA-Radel-2.0 separator had the highest energy efficiency at 60 mA cm^{-2} and 80 mA cm^{-2}. The VRFB assembled with

the QA-Radel-2.4 membrane exhibited the lowest energy efficiency at all the current densities tested, because of the highest VO^{2+} permeability of the sample. Increasing the membrane IEC also resulted in faster capacity fade during cell cycling tests. Due to the best balanced ionic conductivity and VO^{2+} permeability of QA-Radel-2.0, the VRFB with this membrane showed the highest power density of 218 mW cm^{-2}, higher than the maximum power density of the VRFB assembled with N212.

4.2 Membrane Thickness

4.2.1 Introduction

The proton conductivity (σ) and vanadium permeability (*P*, the product of the diffusion coefficient of vanadium in the membrane, *D*, and the species partition coefficient from the solution phase into the membrane phase, *H*) are two of the most important parameters for the operation of PEMs in VRFBs [77,96]. The σ can be converted to membrane resistance, *R*, through $R = L/\sigma A$ (*L* is thickness and *A* is the area for ion conduction), while *P* can be converted to crossover flux, *N*, through $N = -P\Delta C/L$ (ΔC is the vanadium concentration difference of the electrolytes). The membrane resistance determines the VE while the vanadium crossover flux dictates the CE of the operating device. There is a tradeoff between these two fundamental material properties with thickness, through which the cell performance can be optimized for different baseline membrane properties. Generally, proper tailoring of the ion exchange capacity (IEC) of PEMs is the first and the most important step towards balanced proton conductivity and vanadium permeability after the backbone of the separator material is selected [77,97]. Further modifications such as hybridizing or blending with other desirable components like inorganic fillers can lead to better selectivity properties [87,94,98] and the thickness optimization observations in this

work should be generally applicable to the use of many different types of ion exchange membranes in VRFBs.

In addition to chemical composition and properties, the thickness of the membrane has direct implications on the cell performance and longevity. For instance, the thickness of the membrane affects the amount of undesired species crossover during charging/discharging, which governs the capacity loss/fade and thus the long-term performance of VRFBs. Recent work has shown that species crossover in a VRFB occurs as a result of three transport mechanisms in the membrane, namely; convection, diffusion, and migration [78]. Along with the polymer backbone type and electrolyte chemistry, the rate and relative importance of these species transport mechanisms in the membrane is also reported to be highly dependent upon the thickness of the membrane [78]. Thickness controls the ion transport resistance and alters the magnitude of the driving forces governing the species transport during VRFB operation. In particular, the rate of the osmotic convection and diffusion was shown to be highly sensitive to the membrane thickness [78,84].

In addition to capacity loss, the thickness of the membrane also plays a key role in the cell ohmic resistance and membrane mechanical properties such as compressibility and osmotic stability. While the mechanical strength of the membranes is enhanced with thickness, the VE of the overall system is diminished because of the increased ohmic resistance. Furthermore, the CE of the system is observed to increase with a thicker membrane due to the lower amount of vanadium species crossover. Therefore, the thickness of the membranes can simultaneously influence the CE and VE of flow batteries through membrane resistance and electrolyte crossover, similar to the role of membrane IEC or changes in intrinsic membrane properties during

blending/hybridization. Despite its importance, few systematic studies have been performed to understand the role of membrane thickness on the cell performance and assess the importance of optimizing the membrane thickness for a given set of VRFB operational conditions. Herein, the effort on the investigation of the influence of membrane thickness on VRFB cell performance using an IEC-optimized ionomer is reported.

4.2.2 Method of Approach

4.2.2.1 Materials

Fluorinated sulfonated poly(arylene ether) (SFPAE) with an IEC of 1.8 mequiv. g^{-1}, room temperature proton conductivity of 61 mS cm^{-1} and VO_2^+ permeability of 7×10^{-13} m^2 s^{-1} was synthesized by our collaborators at the Pennsylvania University according to the previous reports in the literature [77]. Membranes with three difference thicknesses (28 μm, 45 μm and 80 μm) were obtained by casting different amounts of 8 wt.% SFPAE solution in N,N'-dimethylacetamide onto glass plates followed by drying at 80 ºC for 24 h. All reagents were purchased from common commercial suppliers and used as received.

4.2.2.2 VRFB Construction

A VRFB cell was constructed as described in Sections 2.2.2 and 4.1.2.1.1 [59,81,90].

4.2.2.3 Electrochemical Measurements

All electrochemical measurements were conducted using a custom-designed fully automated redox flow battery testing system as described in Section 2.2.2. For charge/discharge experiments, a constant current program was used with an upper

limit voltage of 1.7 V and a lower limit voltage of 0.7 V to determine the end of the charge/discharge processes under each current density studied. For polarization curve measurements, the current was scanned with the lower limit voltage of 0.2 V to determine the end of the polarization curve. The VRFBs were first fully charged at 80 mA cm^{-2}, then the discharge current was scanned from 0 A to 700 mA cm^{-2} with steps of 10 mA cm^{-2}. The hold time at each step was 30 s. The voltage after 30 s was recorded and plotted against current density.

4.2.3 Results and Discussion

4.2.3.1 Charge/Discharge Behavior

The charge/discharge behavior of a VRFB is usually quantified as the voltage change of the cell as a function of charge/discharge time. When charging a VRFB, the voltage increases gradually with time until the concentration of uncharged species is too low to support the charging rate and then a sudden increase in the charge voltage occurs. This point is generally considered as the end point of the charging process. Similarly, when discharging a VRFB, the voltage decreases gradually with discharge time until the concentration of the charged species becomes insufficient to afford the discharging rate and then a sudden decrease in the discharge voltage occurs, which is taken as the end point of the discharging process.

The charge/discharge curves of VRFBs assembled with different thickness SFPAE membranes (28 μm, 45 μm and 80 μm) are shown in Fig. 4.17. It was observed that the difference between charge and discharge voltage of the VRFBs assembled with different thickness membranes increased with increasing current density. This observation can be explained by analyzing the ohmic losses of the cells with the

different thickness membrane samples. The discharge voltage of a cell can be represented as $V_{dis} = E_0 - \Delta V_{act} - \Delta V_{ohm} - \Delta V_{trans} - \Delta V_{cross}$, where E_0 is the theoretical open circuit voltage of the cell, ΔV_{act} is the voltage loss caused by activation, ΔV_{ohm} is the voltage loss caused by ohmic loss (or IR loss where I is current and R is resistance), ΔV_{trans} is the voltage loss caused by mass transport and ΔV_{cross} is the voltage loss caused by electrolyte crossover. Similarly, the charge voltage of a cell can be calculated as $V_{ch} = E_0 + \Delta V_{act} + \Delta V_{ohm} + \Delta V_{trans} - \Delta V_{cross}$. Both the charge and discharge voltages are influenced by the ohmic loss, which increases with increasing current density and membrane resistance. In this case, the conductivity of SFPAE membrane equilibrated in the electrolyte was 35 mS cm^{-1} at room temperature, lower than the pure proton conductivity of the membrane immersed in deionized water [62]. Therefore, the resistances of 28 μm, 45 μm and 80 μm SFPAE membranes with an active cell area of 10 cm^2 were 8 mΩ, 13 mΩ and 23 mΩ, respectively. Accordingly, the calculated ohmic losses for these membranes at 20 mA cm^{-2} were found to be 1.6 mV, 2.6 mV and 4.6 mV, respectively. When the current density was increased to 80 mA cm^{-2}, the ohmic losses for these tested membranes were increased to 6.4 mV, 10.4 mV and 18.4 mV, respectively.

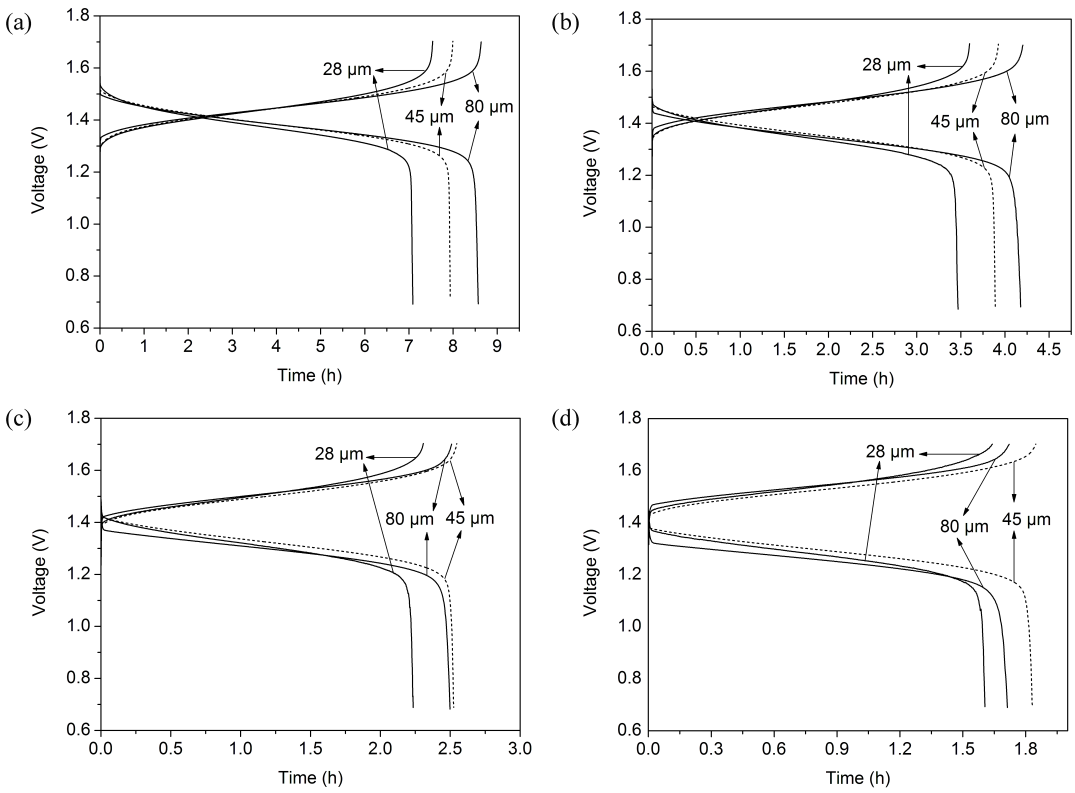

Figure 4.17 Charge/discharge curves of VRFBs assembled with different thickness membranes at (a) 20 mA cm^{-2}; (b) 40 mA cm^{-2}; (c) 60 mA cm^{-2} and (d) 80 mA cm^{-2}.

Since E, ΔV_{act} and ΔV_{trans} are presumably the same for all the membranes, the difference of V_c and V_{dis} for VRFBs assembled with different membranes can only arise from (ΔV_{ohm} – ΔV_{cross}) and (– ΔV_{ohm} – ΔV_{cross}) for charge and discharge, respectively. The ΔV_{cross} decreases with increasing membrane thickness because of the lower amount of electrolyte crossover for a thicker membrane, while ΔV_{ohm} increases with increasing thickness because of the higher resistance for the thicker membrane. The combined effects of these two factors complicates the determination of the link between V_{ch} and V_{dis} for the tested membranes, therefore, no obvious trend of V_{ch} and V_{dis} was observed with the variation of membrane thickness at a given current density.

The trends of V_c and V_{dis} with the variation of current density are displayed in Fig. 4.17. The V_c increased with increasing current density, while V_{dis} decreased with an increase in the current density. It is anticipated that the ΔV_{cross} decreased with increasing current density (since the undesired species crossover is significantly reduced under high current due to the increased electrolyte consumption [78,84]), and the ΔV_{ohm} increased with increasing current density through $\Delta V_{ohm} = IR$. However, the combination of ΔV_{ohm} and ΔV_{cross} has direct implication on the relationship between V_c, V_{dis} and current density, suggesting that the change of ΔV_{ohm} was much more significant than the change of ΔV_{cross} as a function of current density. This observation agrees well with the findings in published experimental data [77] and recent modeling work [99], which was aimed at the comparison of ion transport mechanisms governing species crossover for Nafion® and S-Radel membranes. A thorough analysis of species transport mechanisms in these two membrane types indicated that the species crossover through the membrane was significantly reduced for S-Radel sulfonated aromatic type membranes when compared to Nafion® due to the competing effects of electro-osmotic convection and diffusion during charging/discharging [99]. Accordingly, it is anticipated that significantly lower flux of vanadium species (ΔV_{cross}) across the tested SFPAE membranes (that have similar properties to S-Radel) had minimal influence on V_{ch} and V_{dis}, which can also be observed in these experiments.

The charge and discharge times for the VRFBs assembled with different thickness membranes increased as the membrane thickness increased from 28 μm to 45 μm to 80 μm at 20 mA cm^{-2} and 40 mA cm^{-2}, Fig. 4.17. At higher current densities of 60 mA cm^{-2} and 80 mA cm^{-2}, the charge and discharge times increased for the

membranes in the thickness order of 28 μm, 80 μm and 45 μm, as shown in Fig. 4.17. The longer charge/discharge time for thicker membranes could be attributed to the lower amount of vanadium crossover for the thicker membrane which yields very low capacity fade in the device. However, at high current densities, the VRFB assembled with the 45 μm membrane was observed to have the longest charge/discharge time. This difference in charge/discharge time for different membrane thicknesses can be attributed to the fact that the terminal point of the galvanostatic charging/discharging process is usually determined by a preset voltage value, which is influenced by the ohmic resistance of the membrane. At high current densities, the VRFB assembled with the 80 μm membrane cannot charge and discharge as completely as the VRFB assembled with the 45 μm membrane with the same voltage limit due to the higher ohmic resistance of the 80 μm membrane. In these tests, the end of the charge process was set to 1.7 V because electrode corrosion by VO_2^+ was observed when the cell voltage exceeded this limit [38,88,100]. On the other hand, the charge/discharge time decreased with increasing current density for each membrane, as expected.

The charge depths of the VRFBs as a function of membrane thickness at various current densities are shown in Fig. 4.18. The charge depth herein is defined as the ratio of the measured charge capacity to 100% charge capacity based on the electrolyte concentration and volume. This measure can provide additional information about the electrolyte species utilization efficiency as a function of the charge/discharge time or charge capacity. As shown in Fig. 4.18, the charge depth was observed to vary significantly with the membrane thickness and the current density. For example, the charge depth of the VRFB assembled with a 28 μm membrane at 20 mA cm^{-2} was 80% while that of the VRFB assembled with an 80 μm

membrane at the same current density was found to be 92%. These results indicate that even for the same electrolyte composition and cell construction, the effective cell capacity is highly dependent on the operating conditions and the membrane thickness, which need careful attention for designing optimized VRFB systems.

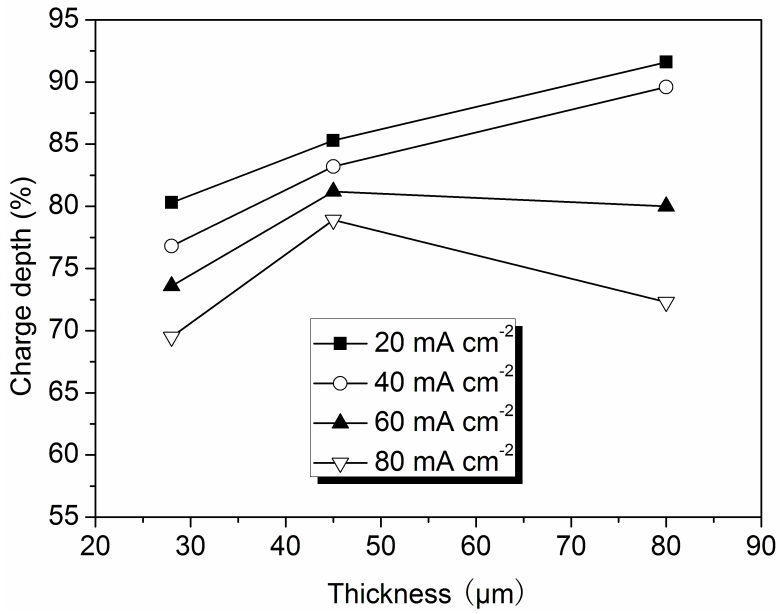

Figure 4.18 Charge depth of the VRFBs as a function of membrane thickness at various current densities.

4.2.3.2 Coulombic, Voltage and Energy Efficiency

The coulombic efficiency (CE), voltage efficiency (VE) and energy efficiency (EE) are the most common performance metrics of VRFBs that can be derived from the charge/discharge curves [38]. The CE describes how well electrons are transferred into and out of the system and can be used to track side reactions or other faradaic losses. During normal operation of a VRFB, the CE is likely only limited by the electrolyte crossover (vanadium permeation) because ~100% CE can be achieved using an AEM with extremely low vanadium permeability [62]. From Fig. 4.19, it can be seen that the CE increased with increasing membrane thickness and current density, which can be attributed to the reduced electrolyte crossover due to both the

suppressed convective/diffusive species transport for thicker membranes and the increased electrolyte consumption with increasing current density [78,84].

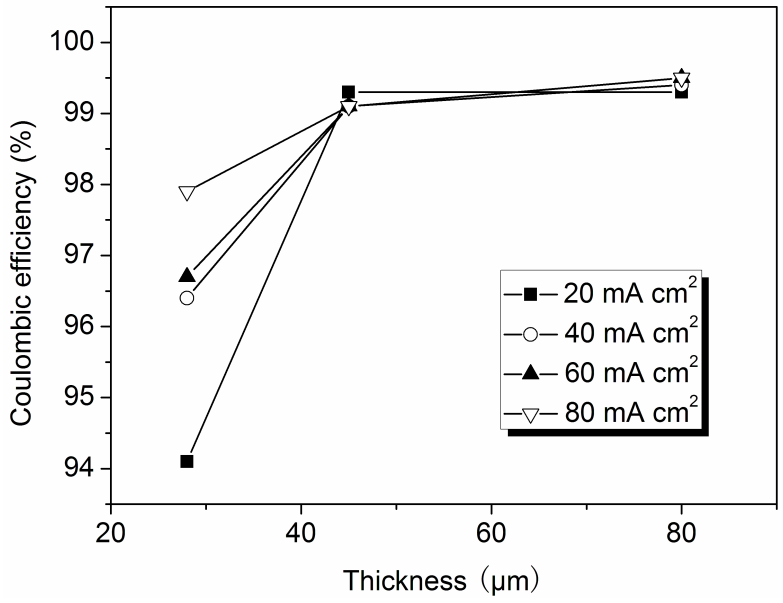

Figure 4.19 Coulombic efficiency of the VRFBs as a function of membrane thickness at various current densities.

The VE describes losses through both overpotential and electrolyte crossover. It can be seen from Fig. 4.20 that the VE decreased with increasing current density due to larger ohmic losses at higher current densities. Similarly, it is expected that the VE decreases with increasing membrane thickness due to the higher resistance of thicker membranes. However, the VRFB assembled with the 28 μm membrane did not always show the highest VE over the range of tested current densities. This observation can be attributed to the combined effects of ohmic loss and crossover as discussed previously. Because the 28 μm membrane is very thin and would be prone to high vanadium flux, crossover losses may have negatively impacted the cell performance and mitigated the positive effect of reduced resistance of this sample. The EEs of the VRFBs assembled with different thickness membranes are also shown

in Fig. 4.21. As the product of CE and VE, EE reveals the overall efficiency of the VRFB. It can be seen in Fig. 4.21 that the VRFB assembled with the 45 μm membrane exhibited the highest EE among the membranes studied, suggesting that the 45 μm SFPAE membrane possessed the best compromise between ohmic resistance and crossover for the intrinsic ion conductivity and vanadium permeability of this material.

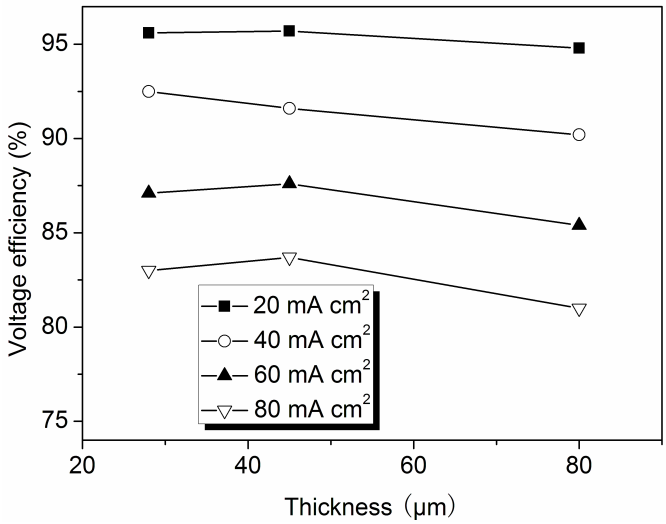

Figure 4.20 Voltage efficiency of the VRFBs as a function of membrane thickness at various current densities.

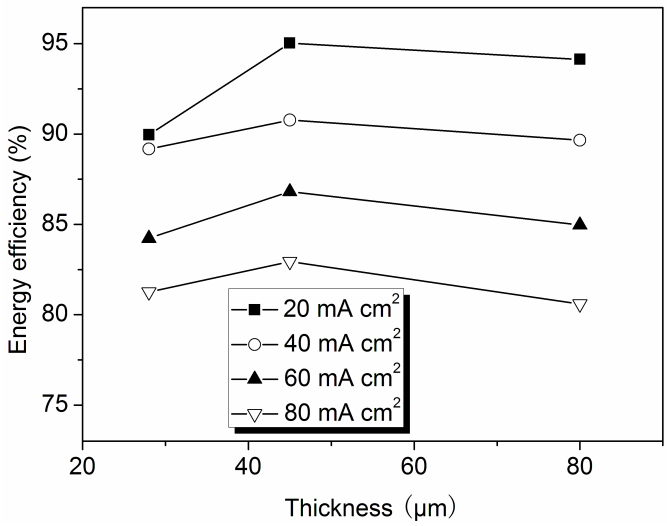

Figure 4.21 Energy efficiency of the VRFBs as a function of membrane thickness at various current densities.

4.2.3.3 Polarization Curves

Commonly, VRFBs are examined over the current density range of 10-100 mA cm^{-2} without reaching the maximum power density of the cell [100-102]. To determine the maximum power density of VRFBs assembled with the tested SFPAE membranes and to understand the influence of membrane thickness on the maximum power density, the polarization curves of the VRFBs assembled with different thickness SFPAE membranes were measured, Fig. 4.22. The maximum power densities for the VRFBs assembled with 28 μm, 45 μm and 80 μm membranes were found to be 267 mW cm^{-2}, 311 mW cm^{-2} and 253 mW cm^{-2}, respectively. The 45 μm membrane was observed to be the optimal sample among the three thicknesses studied based on the polarization curve analysis as the cell with this membrane gave the highest maximum power density. A N212 membrane (DuPont) with wet thickness of 60 μm was also measured in a VRFB under the same conditions. The maximum power density for this membrane was found to be only 204 mW cm^{-2}, confirming the superior performance of the SFPAE membranes when compared to N212 as reported previously [77].

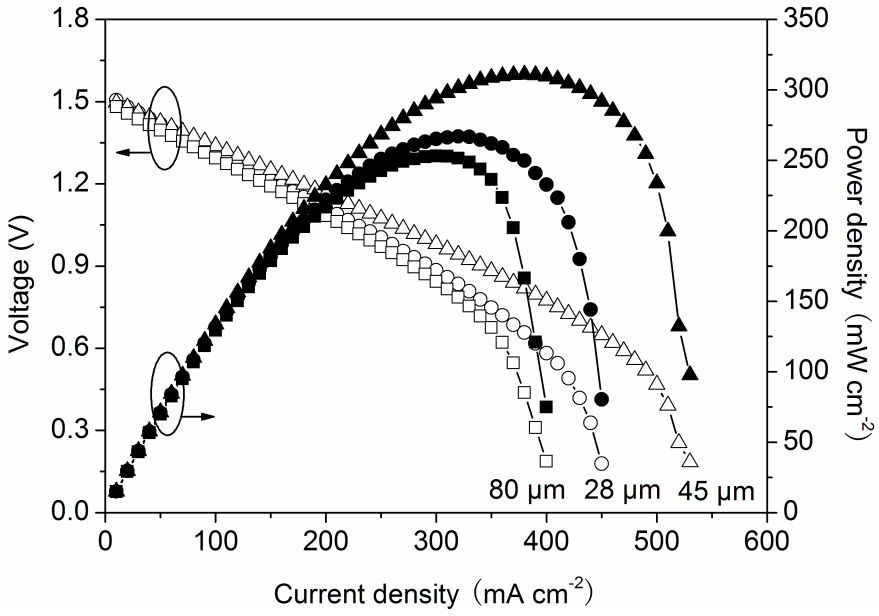

Figure 4.22 Polarization curves of the VRFBs assembled with different thickness membranes.

4.2.4 Conclusions

Proton exchange membranes based on IEC-optimized SFPAE 1.8 meq g^{-1} polymer were prepared with three thicknesses of 28 μm, 45 μm and 80 μm and were evaluated in VRFB operation to explore the effect of membrane thickness on the cell performance. It was found that the charge/discharge voltage and time were both influenced by the membrane thickness. The membrane thickness governs the membrane resistance and electrolyte crossover directly, which was used to rationalize the change of charge/discharge voltage and time with respect to the membrane thickness. The charge depth, which is defined as the effective capacity of the battery, was found to be highly dependent on the membrane thickness and VRFB operational conditions. Due to the combination effects of ohmic loss and electrolyte crossover loss, the 45 μm thick membrane sample was found to be the optimum thickness of the SFPAE material studied in this work in terms of VRFB energy efficiency and maximum power density.

Chapter 5. Effects of Operating Conditions on Capacity Loss

This chapter presents the studies performed to determine the effects of operating conditions on long-term VRFB performance. Several studies were performed to identify effective mitigation strategies to control and minimize the capacity fade in these systems. The details of these studies are presented in the following sections.

5.1 Controlling Electrolyte Flow Rate

5.1.1 Introduction

The model simulations that were explained in Chapter 4 suggested that diffusion and migration may not be the dominating mechanisms for species crossover in the membrane. Motivated by this observation, the objective of this study is to investigate the convective transport and related effects on the vanadium crossover. Several case studies were conducted to examine the impact of i) electro-osmotic convection due to viscous interactions between the mobile ions and electrolyte and ii) osmotic convection due to pressure gradients across the membrane. In addition, the model was utilized to provide insight on how to select operating conditions to control the convection in the membrane and minimize the capacity loss in VRFBs.

In this section, four different case studies (that have different electrolyte viscosities and flow rates) were simulated to quantify the impact of convection on vanadium crossover. The main input parameters for these cases can be found in Table 5.1.

Table 5.1 Input parameters for simulated cases.

Parameters	Operating conditions		Viscosity effect	
	Case 1 (const flow rate)	Case 2 (const pressure)	Case 3	Case 4
Cell size [cm^2]	10	10	10	10
Current [mA]	500	500	500	500
Half-cell volume [ml]	25	25	25	25
Initial vanadium [mol l^{-1}]	1.04	1.04	1.04	1.04
Total sulfate [mol l^{-1}]	5.04	5.04	5.04	5.04
(+) viscosity [Pa s]	5×10^{-3}	5×10^{-3}	2.5×10^{-3}	2.5×10^{-3}
(−) viscosity [Pa s]	2.5×10^{-3}	2.5×10^{-3}	5×10^{-3}	25×10^{-3}
(+) flow rate [ml min^{-1}]	20	40	20	20
(−) flow rate [ml min^{-1}]	20	20	20	20

5.1.2 Results and Discussions

5.1.2.1 Constant Flow Rate vs. Constant Pressure

Osmotic convection occurs due to the pressure gradients across the membrane. These pressure gradients arise as a result of the electrolyte flow conditions (i.e., flow rate and electrolyte composition) within the system. Therefore, the first set of simulations (Cases 1 and 2) were selected to represent two flow conditions for a VRFB. Case 1 is a constant flow rate condition (i.e., same flow rate in each half-cell), and Case 2 represents a constant pressure condition (i.e., same pressure throughout each half-cell), where constant pressure was obtained by increasing the positive half-cell flow rate to account for variations in viscosity. In this study, simulations were performed for an electrolyte composition that has 1.04 M $VOSO_4$ (VO^{2+}) in 4 M H_2SO_4.

Figure 5.1a shows the change in capacity after each cycle for both cases, where capacity was calculated with respect to the discharge time of the first cycle:

$$capacity = \left(\frac{t_{dis,n}}{t_{dis,1}} \right) \times 100\% \tag{5.1}$$

The capacity of a VRFB is limited by the amount of vanadium in the most vanadium deficient half-cell, which is the positive half-cell for the electrolyte composition simulated in this study. As seen in Fig. 1a, the constant pressure operation appears to have significantly reduced capacity loss (~96% capacity after 35 cycles) as compared to the constant flow rate operation (~87% capacity after 35 cycles). The amount of vanadium crossover in the constant pressure operation is observed to be relatively lower than the constant flow rate operation (Fig. 5.1b). This trend can be attributed to the smaller net vanadium transfer from the positive to the negative half-cell in the constant pressure condition. When the positive half-cells (i.e., deficient half-cells) of these two cases are compared, the constant pressure case has a consistently larger amount of vanadium in the positive half-cell over each cycle due to the slower rate of capacity loss.

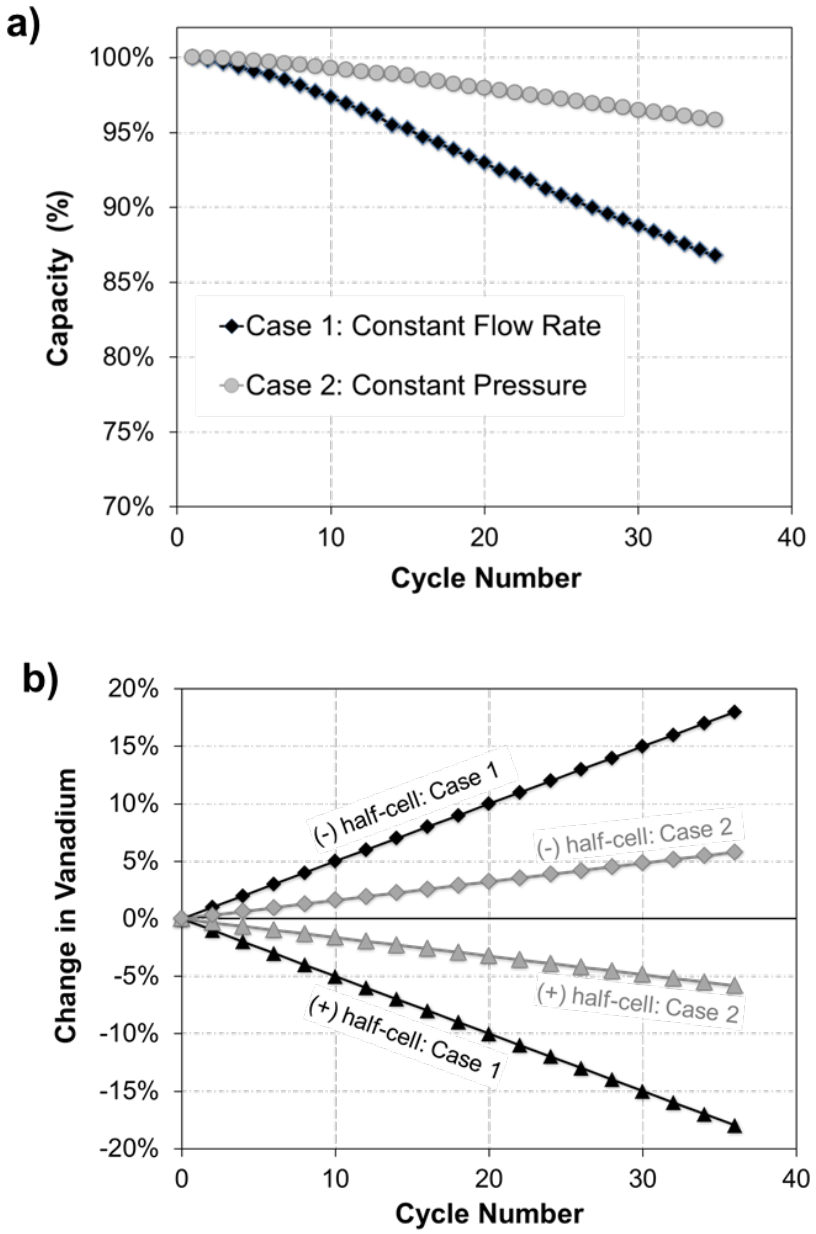

Figure 5.1 Simulated results for constant pressure vs. constant flow rate case study: a) change in capacity loss (discharge time) after 35 cycles and b) change in vanadium in each half-cell at the end of each cycle.

The observed discrepancy in vanadium crossover between Cases 1 and 2 (Fig. 5.1b) can be explained through analysis of the magnitude and direction of the osmotic convection. Fig. 5.2 shows the average convection in the membrane at 50% state of charge (SOC) during the 35th cycle for both cases. Fig. 5.2a shows that the constant flow rate operating condition (Case 1) produces a constant osmotic convection from

the '+' to '-' half-cell regardless of the direction of current, whereas the electro-osmotic convection is same but in different direction during charge and discharge. This trend can be attributed to the difference in electrolyte viscosity between '+' and '-' half-cell (the positive electrolyte is more viscous than the negative electrolyte). The difference in electrolyte viscosities causes each half-cell to have a different pressure drop, which would result in a pressure difference (and osmotic convection) across the membrane.

In addition, Fig. 5.2a shows that the *net* rate of convection from the '+' to '-' half-cell during charge is 2X higher than the *net* rate of convection from the '-' to '+' half-cell during discharge. The difference in net convective transfer is governed by the osmotic convection, since electro-osmotic convection yields zero net effect for an entire cycle. Therefore, during constant flow rate operation, one would expect a net convection from the '+' to '-' half-cell, which yields a net vanadium transfer in the same direction.

In line with the analyses given above, Fig. 5.2b suggests that the constant pressure operating condition (Case 2) eliminates the osmotic convection, which results in a more balanced net convection between charging and discharging. Elimination of the pressure gradient across the membrane reduces the net vanadium transfer from the '+' to the '-' half-cell during a single cycle, which agrees with the trends in vanadium transfer observed for the 35 cycle simulation (Fig 5.1b). However, it is important to note that despite the elimination of osmosis, a net crossover from the '+' to '-' half-cell is still observed for Case 2. This occurs for two reasons: *i)* electro-osmosis always facilitates vanadium transfer in the same direction as current (i.e. from '+' to '-' half-

cell during charge and vice versa during discharge) and *ii)* the charge time is longer than the discharge time. Therefore, in a given cycle, the longer charge time results in more time for vanadium to transfer from the '+' to '-' half-cell, yielding a net crossover towards the '-' half-cell. Based on the simulation results of Cases 1 and 2, it can be concluded that one potential approach to mitigate the capacity loss in VRFB would be to operate the system at constant pressure condition through utilization of asymmetric flow rates (i.e., different flow rates in the '+' and '-' half-cells) to minimize the impact of osmotic convection on species crossover.

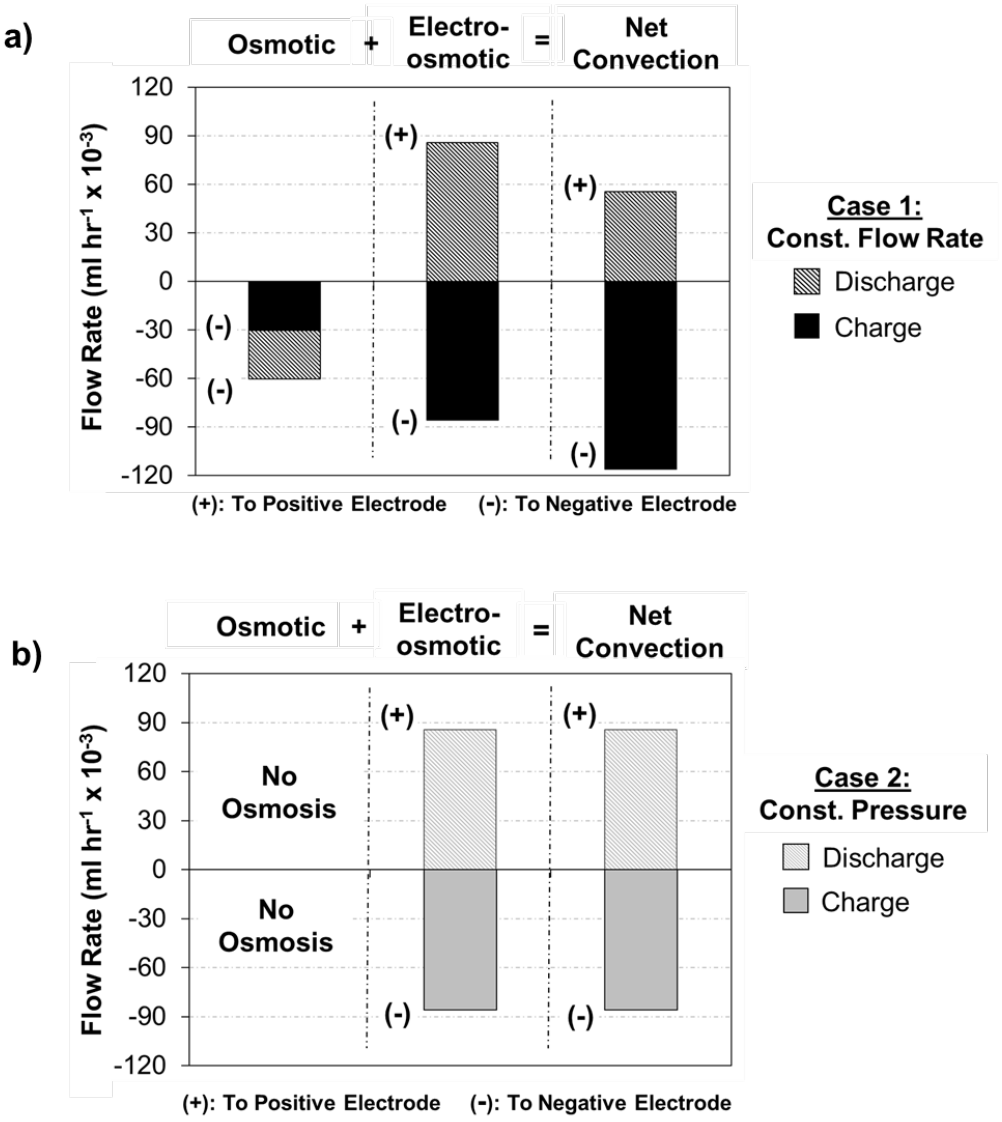

Figure 5.2 Average convective flow rate across the membrane during the 35th cycle at 50% SOC for a) Case 1 (constant flow rate) and b) Case 2 (constant pressure).

5.1.2.2 Influence of Viscosity on Vanadium Crossover

In the previous section, it was suggested that the osmotic convection in the constant flow rate case occurs as a result of variations in the electrolyte viscosities, which yields a pressure gradient across the membrane. To further investigate the impact of electrolyte viscosity on vanadium crossover, three different cases (Cases 1, 3, and 4, see Table 5.1) were simulated with varying electrolyte viscosities.

Figure 5.3a shows the capacity loss over 20 cycles for these three cases. It was observed that the rate of capacity loss varies significantly depending on the variations in electrolyte viscosity. For example, a 5X increase in the negative electrolyte viscosity between Cases 3 and 4 results in an increase of capacity loss from ~0% to over 25% after 20 cycles. These variations in capacity loss can be attributed to the impact of the difference in electrolyte viscosities on the magnitude of the pressure gradient across the membrane.

In addition, Fig. 5.3b indicates that the direction and magnitude of net vanadium crossover also depends on the electrolyte viscosities, which vary based on electrolyte composition and SOC. The net direction of vanadium crossover is found to be towards the less viscous electrolyte regardless of the tested cases (e.g., '+' half-cell for Case 1 and '-' half-cell for Cases 3 and 4), which agrees with the fact that the direction of osmotic convection will always take place from high pressure region (more viscous electrolyte) to low pressure region (less viscous electrolyte).

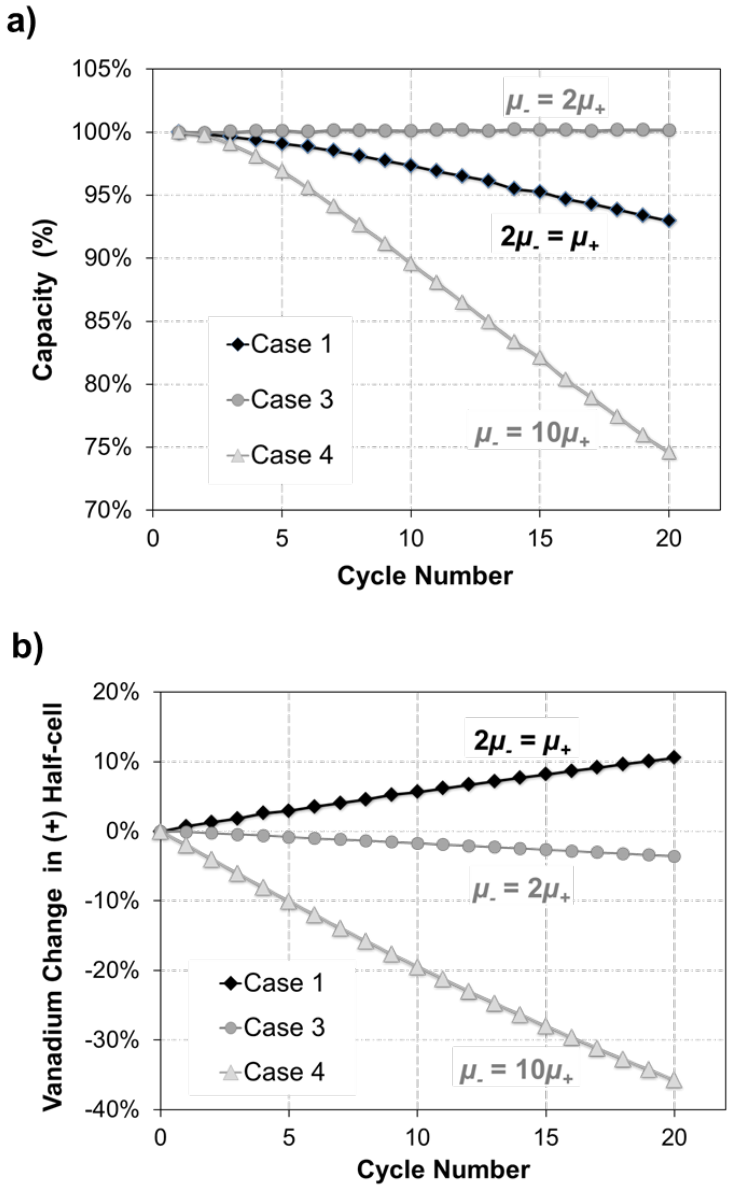

Figure 5.3 Simulated results for viscosity case study: a) change in capacity loss (discharge time) after 20 cycles, and b) change in vanadium in '+' half-cell at the end of each cycle.

5.1.3 Conclusions

In the first section of this chapter, the convective transport in the membrane and related effects on vanadium crossover and capacity loss in VRFBs was investigated using the developed model explained in Chapter 2. The model predictions indicate that convective transport across the membrane is a major mechanism contributing to the vanadium crossover. Model simulations suggest that the rate of vanadium

crossover can be reduced through the use of asymmetric flow rates (different flow rates in the '+' and '-' half-cells) to control the pressure drop across the membrane and minimize the impact of osmotic convection. Furthermore, the direction and magnitude of the osmotic convection and resulting crossover is found to be highly dependent on the viscosity of the electrolytes in each half-cell.

5.2 Controlling Charge/Discharge Current

5.2.1 Introduction

In the Section 4.1.1 the species transport mechanisms governing capacity loss in Nafion® 117 and sulfonated Radel (s-Radel) membrane were compared. The goal of this study was to quantify how the differences in key membrane properties affect the dominance of specific species transport mechanisms within the membrane. When compared to Nafion®, s-Radel (composed of post-sulfonated polyphenylsulfone resin - Radel) has been shown to possess superior ion selectivity, high coulombic efficiency, and low capacity fade rate (almost half that of Nafion®) [8]. Simulation results reported in Section 4.1.1 indicated that the transport of vanadium ions across s-Radel is primarily dominated by electro-osmotic convection, which depends on the magnitude and direction of the current [99]. Accordingly, it was suggested that varying the applied current during charging and discharging (i.e., using different current during charge and discharge) can potentially balance the convective crossover (osmosis and electro-osmotic convection) during cycling, which would reduce the capacity fade.

Motivated by the findings in the Section 4.1.1, in this part of the thesis, the effectiveness of altering the charge and discharge current as a potential technique to

reduce the capacity loss in VRFBs were further explored. Two types of membranes, namely a diffusion-dominated and a convection-dominated membrane, were investigated to assess the effectiveness of the proposed technique with respect to membrane type/properties. Analyses were conducted by using the experimentally-validated VRFB model that was explained in detail in Chapter 2. Several studies, including; the long-term cycling performance under symmetric (i.e., same current during charge/discharge) and asymmetric current operations (i.e., different currents during charging and discharging) were performed for these two membrane types. The changes in specific transport modes and resulting crossover with respect to tested operating conditions were quantified and linked to the membrane properties to assess the effectiveness of the approach and provide guidance for future optimization efforts.

5.2.2 Method of Approach

5.2.2.1 Simulated Case Studies

In this study, simulations were performed for two different membrane types (i.e., diffusion-dominated and convention-dominated membrane), in which different transport modes dominate species crossover. For the diffusion-dominated membrane, Nafion® 117 was selected as an exemplary membrane for analysis. Nafion® 117 has been extensively studied in other fields and its properties have been well-characterized [47,49-52] (see Table 5.2). In addition, Nafion® has been used in many VRFB studies [68-69,98-102] as a baseline membrane to study device performance. For the convection-dominated membrane, a model membrane (see Table 5.2) that has properties similar to those found in s-Radel (e.g., much lower diffusivity and higher ion exchange capacity than Nafion®) was selected [8]. The selection of the properties for the convection-dominated membrane was performed based on the findings in

previous studies reported in the literature [99]. The simulation results reported in Section 4.1.1 indicated that the transport of vanadium ions due to convection (specifically electro-osmotic convection) is more dominant for the membranes that have large number of fixed acid sites and free ions [99]. With the larger number of fixed charges, more interaction is expected to occur between the charged species within the membrane, which would lead to higher electro-osmotic drag of electrolyte across the membrane [99].

Table 5.2 Membrane properties and parameters used in the model.

Symbol	Description	Nafion® 117	Convection-dominated Membrane
L^m	Membrane thickness (μm)	203 [22]	115
c_f	Fixed acid concentration (mol m^{-3})	1432 [22]	2800
κ_ϕ	Electrokinetic permeability (m^2)[a]	1.13×10^{-20}	7.533×10^{-21}
κ_p	Hydraulic permeability (m^2)	1.58×10^{-18} [23]	5.27×10^{-19}
D_{II}^m	V(II) membrane diffusion coefficient ($m^2\ s^{-1}$)[a]	3.125×10^{-12}	2.0×10^{-13}
D_{III}^m	V(III) membrane diffusion coefficient ($m^2\ s^{-1}$)	5.93×10^{-12} [24]	3.80×10^{-13}
D_{IV}^m	V(IV) membrane diffusion coefficient ($m^2\ s^{-1}$)	5.0×10^{-12} [24]	3.21×10^{-13}
D_V^m	V(V) membrane diffusion coefficient ($m^2\ s^{-1}$)	1.17×10^{-12} [24]	7.5×10^{-14}
$D_{H^+}^m$	H^+ membrane diffusion coefficient ($m^2\ s^{-1}$)	3.35×10^{-9} [25]	2.68×10^{-9}
$D_{HSO_4^-}^m$	HSO_4^- membrane diffusion coefficient ($m^2\ s^{-1}$)	4×10^{-11} [26]	2×10^{-11}

[a] Fitted parameter

In terms of simulations, the convection-dominated membrane was simulated at four different charging current densities (e.g., 400 A m^{-2}, 600 A m^{-2}, 800 A m^{-2} and 1000 A m^{-2}), while the discharge current was held constant at 600 A m^{-2} for each case. Similarly, the diffusion-dominated membrane (Nafion® 117) was simulated at a charging current density of 500 A m^{-2} and 1000 A m^{-2} while the discharging current was held constant at 500 A m^{-2}. There are two main reasons why the charging current was varied while the discharging current kept constant in this study. The first reason is that from an operational perspective, a VRFB typically considered for use as a generator in the electricity market must satisfy the load, in which it is dispatched to serve, up to the maximum power bid placed by the operator. Thus, the output power of the system is dictated by the demand for electricity, and cannot be actively controlled by the operator to minimize crossover. However, when the system is charging (i.e., acting as a load on the electrical grid), the consumption can be varied at the operator's discretion. For this reason, it is reasonable to consider the charging current as the controllable variable. The second reason is that in Section 4.1.1, it was found that crossover appears to occur much more during discharging than charging [96]. Therefore, changing the current during charging would provide more insight with regards to the possibility of balancing the species crossover (and thus reducing overall net crossover) between charging and discharging.

5.2.3 Results and Discussion

5.2.3.1 Capacity Loss for Convection-dominated Membrane w.r.t Asymmetric Current Operation

Figure 5.4 compares the capacity fade for the convection-dominated membrane under four different charging current conditions. As seen in Fig. 5.4, the capacity loss of the VRFB under all four operating conditions generally follows the same trend. Initially,

the loss in capacity is not significant due to very small amount of accumulation of vanadium ions in each half-cell. However, as the VRFB continues to be cycled, the change in capacity is more pronounced due to the build-up of vanadium species in each half-cell. When the tested conditions are compared, it is observed that the change in capacity considerably varies with increasing the charging current from 400 A m^{-2} to 1000 A m^{-2}, which indicates the benefit of operating the VRFB under an asymmetric current condition. As seen in Fig. 5.4, an improvement of ~ 7.1% in the capacity retention is observed at the end of 40th cycle for 1000C/600D case, as compared to 400C/600D case (C represents charging where D represents discharging current density).

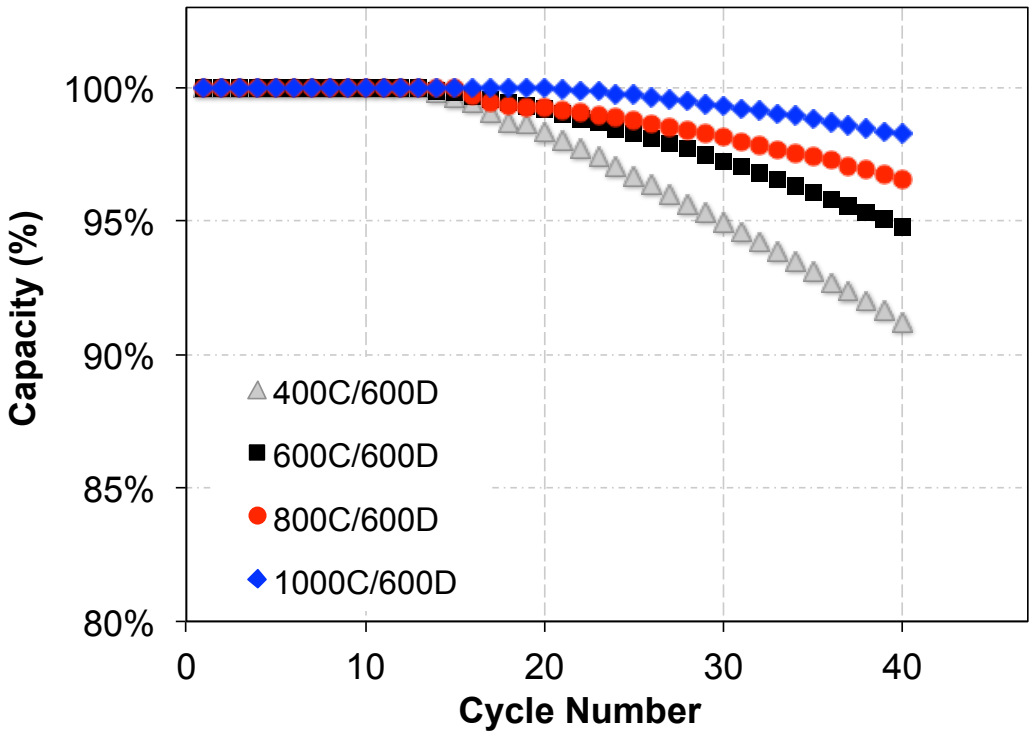

Figure 5.4 Capacity loss over 40 cycles when operated at 400C/600D (i.e., charging at 400 A m^{-2} and discharging at 600 A m^{-2}), 600C/600D, 800C/600D, and 1000C/600D for the convection-dominated membrane.

To investigate the rationale behind this improvement, the change in the crossover of vanadium ions with respect to the tested conditions was analyzed. Fig. 5.5 shows a representative analysis of the crossover mechanisms for V^{2+} for the 20th cycle at 50% SOC. As the charging current density increases, the diffusive and migrative fluxes do not change substantially. Diffusion is driven by the concentration gradients that exist across the membrane, whereas migration is driven by the potential gradient between the two half-cells. Neither of these parameters (i.e., concentration and potential gradient) is significantly affected by the increase in the charging current density, therefore the change in diffusive and migrative flux is observed to be very small (almost negligible) for all these tested cases (Fig. 5.5). On the other hand, the convective flux during charging is observed to increase with the charging current and consequently, the net convective flux over the course of a single cycle decreases as the charging the current increases from 400 to 1000 A m^{-2}. Since convection is the dominant transport mechanism for this type of membrane, a decrease in the net convective flux also contributes to a reduction in the net "total" crossover flux of vanadium ions (Fig. 5.5).

To further investigate this observation, the change in the flux of individual vanadium species was analyzed. Fig. 5.6 shows the net crossover flux of each vanadium species (V^{2+}, V^{3+}, V^{4+} and V^{5+}) at 50 % SOC for the 20th cycle for the tested conditions. Similarly, the net crossover of all species is observed to decrease considerably as the charging current density increases from 400 to 1000 A m^{-2}. The decrease in the net crossover flux of each vanadium ions represents the primary reason for the observed 7.1 % improvement in the capacity retention with increasing charging current shown in Fig. 5.4.

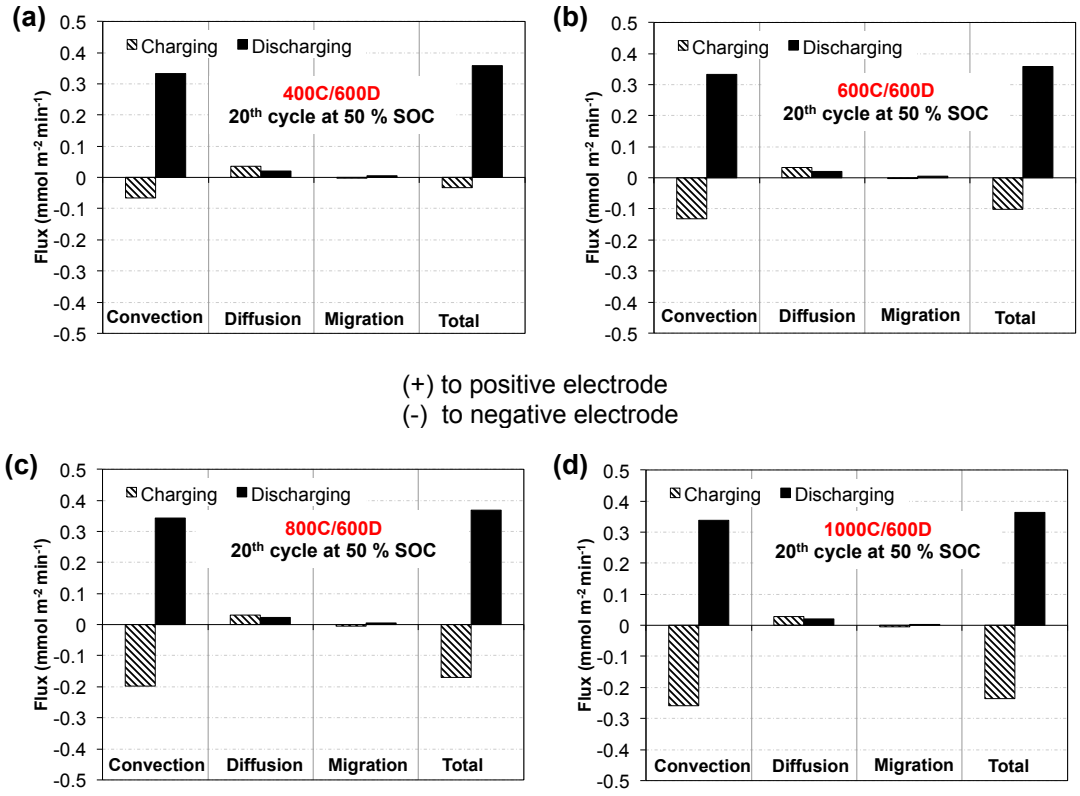

Figure 5.5 Crossover flux of V^{2+} ions due to diffusion, convection, and migration (20th cycle at 50% SOC) when operated at (a) 400C/600D (charging at 400 A m^{-2} and discharging at 600 A m^{-2}); (b) 600C/600D; (c) 800C/600D; (d) 1000C/600D for the convection-dominated membrane.

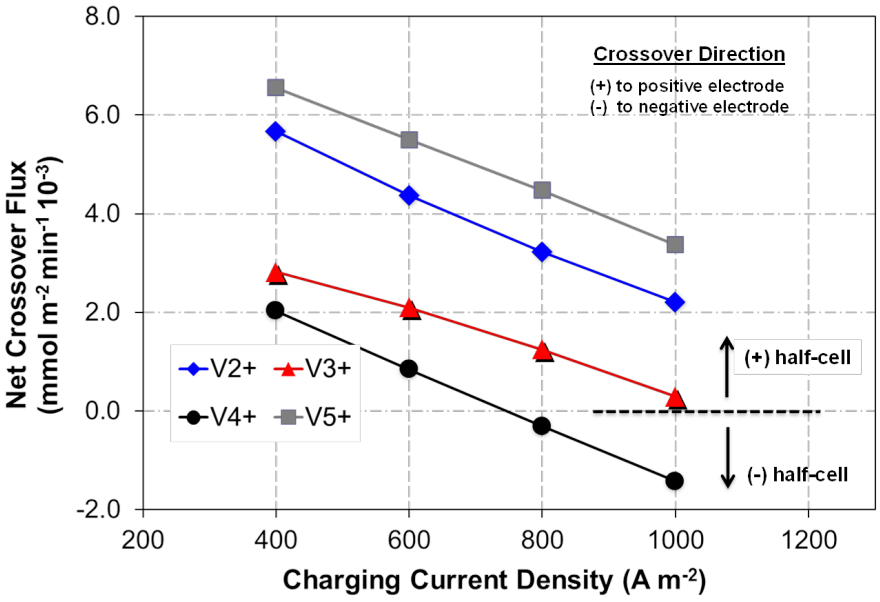

Figure 5.6 Net crossover flux of V^{2+}, V^{3+}, V^{4+}, and V^{5+} (20^{th} cycle at 50% SOC) when operated at 400C/600D (charging at 400 A m^{-2} and discharging at 600 A m^{-2}), 600C/600D, 800C/600D, and 1000C/600D for the convection-dominated membrane.

5.2.3.2 Dependence of Capacity Loss on Charging Current

The simulation results shown in Figs. 5.5 and 5.6 suggest that the magnitude and direction of "net" crossover flux for the convection-dominated membrane highly depends on the charging current. In order to quantify this dependency, the convective crossover of the bulk electrolyte was predicted for the tested conditions and is shown in Fig. 5.7. Figs 5.7a, 5.7c, and 5.7d depict the convective crossover of the bulk electrolyte under asymmetric current conditions, whereas Fig. 5.7b shows the convective crossover during the symmetric current operation. In each of these cases, osmotic convection is found to occur in the same direction with the same magnitude (for both charging and discharging) irrespective of the charging current. This trend is expected since osmotic convection is driven by the pressure gradient across the membrane, rather than the current. The electro-osmotic convection, on the other hand, appears to be considerably affected by the charging current. Under asymmetric

current operation, simulation results indicate that the electro-osmotic convection during charging and discharging is not balanced (e.g., having different magnitudes and directions). As the charging current increases from 400 A m^{-2} to 1000 A m^{-2}, the electro-osmotic convection during "charging" is observed to increase. This increase appears to compensate for the impact of the osmotic crossover, and lead to a decrease in the overall "net" convective flux.

To further investigate this observation, the change in volume of electrolyte in each half-cell was analyzed for all these four conditions. A representative analysis of change in electrolyte volume for 20^{th} cycle is shown in Fig. 5.8. It is observed that the net rate of vanadium crossover is greater during discharging than charging for all the tested conditions. Furthermore, increasing the charging current density appears to reduce the net change in volume of electrolyte in each half-cell at the end of the cycle. This finding also agrees well with the previous observation of reduced "net" convective crossover with increasing charging current.

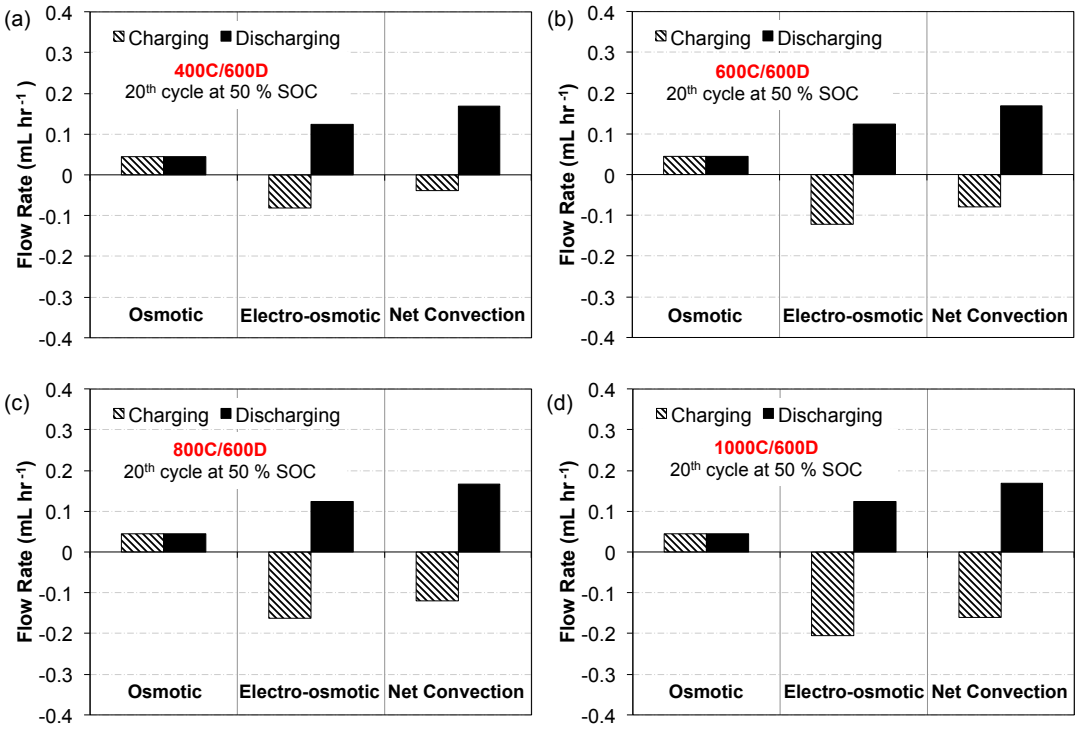

Figure 5.7 Convective crossover (osmotic, electro-osmotic, and total) of bulk electrolytes (20^{th} cycle at 50% SOC) when operated at (a) 400C/600D (charging at 400 A m^{-2} and discharging at 600 A m^{-2}); (b) 600C/600D; (c) 800C/600D; (d) 1000C/600D for the convection-dominated membrane.

It is also important to note that although a significant reduction in capacity fade was observed by operating under asymmetric current conditions, the capacity loss was not entirely eliminated for the convection-dominated membrane. This is due to the contributions of diffusion to the overall crossover of vanadium ions. As shown in Fig. 5.5, although the effect of convection is significantly minimized with increasing charging current, diffusion (driven by the concentration gradient across the membrane) occurs in the same direction during charging and discharging. As a result, the net contribution of diffusion for each vanadium species, at the end of a single cycle is non-zero, which leads to a small capacity loss in the system. However, it should be noted that as the VRFB is continually cycled, the driving force for diffusion

(i.e. the concentration gradient) gradually diminishes over time with the accumulation of an equivalent concentration of vanadium ions in each half-cell.

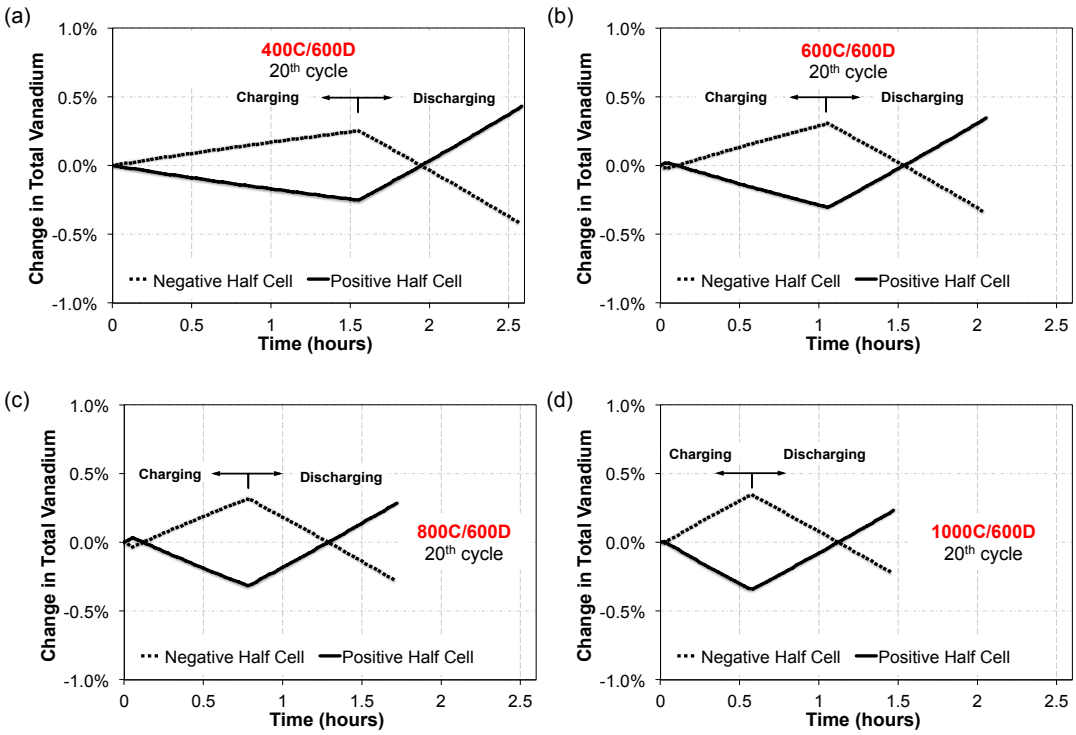

Figure 5.8 Change in volume of each half-cell (20th cycle) operated at (a) 400C/600D (charging at 400 A m^{-2} and discharging at 600 A m^{-2}); (b) 600C/600D; (c) 800C/600D; (d) 1000C/600D for the convection-dominated membrane.

5.2.3.3 Voltage Efficiencies for Convection-dominated Membrane

The simulation results indicate the possibility of reducing the capacity loss for the convection-dominated membrane by running the system under asymmetric current operation (i.e., increasing charging current). In order to determine the cost of this improvement, the voltage efficiencies of the system under each condition were analyzed. As shown in Fig. 5.9, increasing the charging current density from 400 A m^{-2} to 1000 A m^{-2} decreased the average voltage efficiency over 40 cycles by ~ 6%. This reduction in voltage efficiency can be attributed to the increased ohmic losses as a result of increased charging current. Increasing the charging current density

increases the rate at which ions flow across the membrane to maintain the electroneutrality in the system. Assuming that the resistance of the membrane stays fairly constant, an increased current across the membrane manifests itself as a higher voltage drop (i.e., ohmic loss), which would adversely impact the voltage efficiencies. The same ohmic behavior occurs in the electrodes and current-collectors as well.

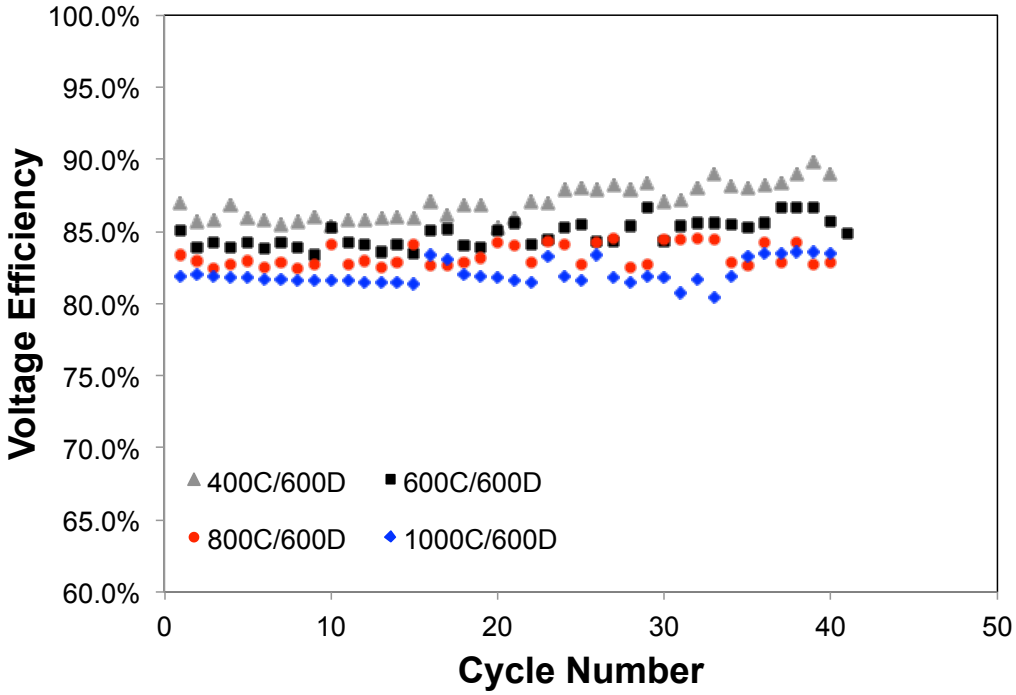

Figure 5.9 Voltage efficiency over 40 cycles when operated at (a) 400C/600D (charging at 400 A m^{-2} and discharging at 600 A m^{-2}); (b) 600C/600D; (c) 800C/600D; (d) 1000C/600D for the convection-dominated membrane.

5.2.3.4 Capacity Loss for Diffusion-dominated Membrane (Nafion® 117)

In the second part of this study, Nafion® 117 was simulated in order to investigate the effects of asymmetric current operation on the diffusion-dominated membrane. In these simulations, two different charging current densities (500 A m^{-2} and 1000 A m^{-2}) were simulated, while the discharging current was held constant at 500 A m^{-2}. The simulated charging current densities are representative of the high and low ends of those used in the simulations for the convection-dominated membrane to gauge the

impact of asymmetric current operation. According to the simulation results reported in Section 4.1.1, it was found that under symmetric current condition, the net convective crossover is always greater during discharging than charging due to the dominance of osmotic convection, which occurs in the same direction for both charging and discharging.

Figure 5.10 shows the predicted capacity loss and voltage efficiency over 40 cycles for the diffusion-dominated membrane. It is observed that increasing the charging current from 500 to 1000 A m^{-2} decreases the capacity loss by approximately 12.4 %. However, the average voltage efficiency over 40 cycles is observed to decrease by ~4.3 % due to the increased ohmic losses.

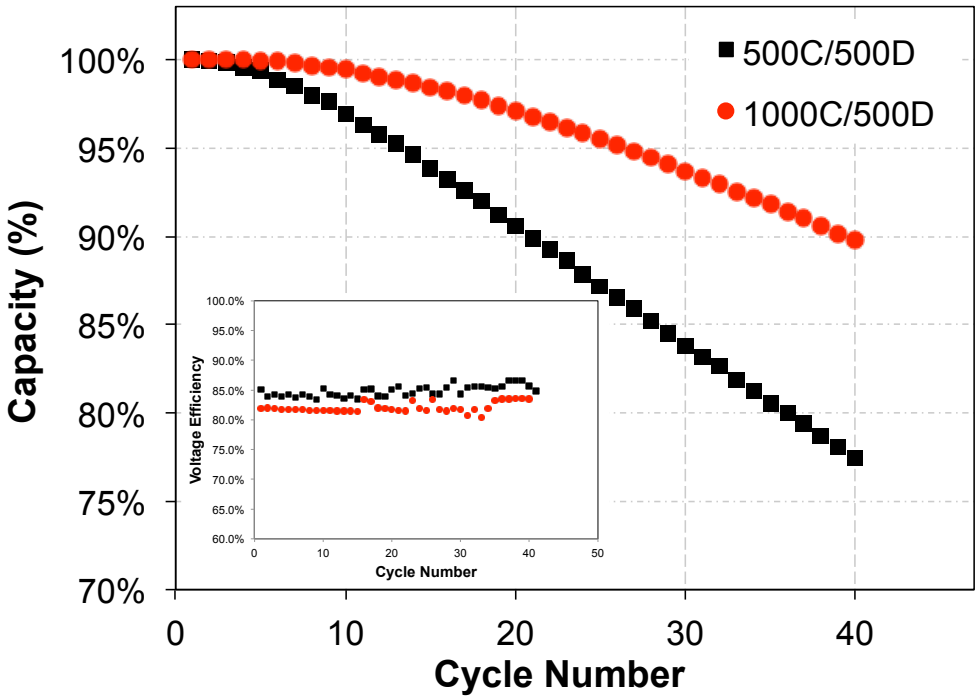

Figure 5.10 Capacity loss and voltage efficiency over 40 cycles when operated at 500C/500D (charging at 500 A m^{-2} and discharging at 500 A m^{-2}), and 1000C/500D for the diffusion-dominated membrane (Nafion® 117).

Physical insight into the observed decrease in the capacity fade was obtained by investigating the crossover of active species across the membrane. Figs 5.11 and 5.12 show the crossover flux for all mechanisms (i.e., convection, diffusion and migration), and the convective crossover of the bulk electrolyte under these two operating conditions, respectively. As seen from Fig. 5.11, the main difference between these two cases is the direction of convection during charging. As the charging current is increased from 500 A m^{-2} to 1000 A m^{-2}, convection during charging changes direction, which leads to a reduction in "net" convection at the end of a full cycle (Fig. 5.11b). As shown in Fig. 5.12, this change of direction in convection stems from the increased electro-osmotic drag during charging with increasing charging current. Furthermore, increasing the charging current density increased the magnitude of the electro-osmotic crossover during charging, which compensates for the osmotic crossover and reduces the "net" convective crossover. The decrease in "net" convection leads to a reduction in the total crossover flux, which manifests itself as a reduction in the overall capacity loss of the device.

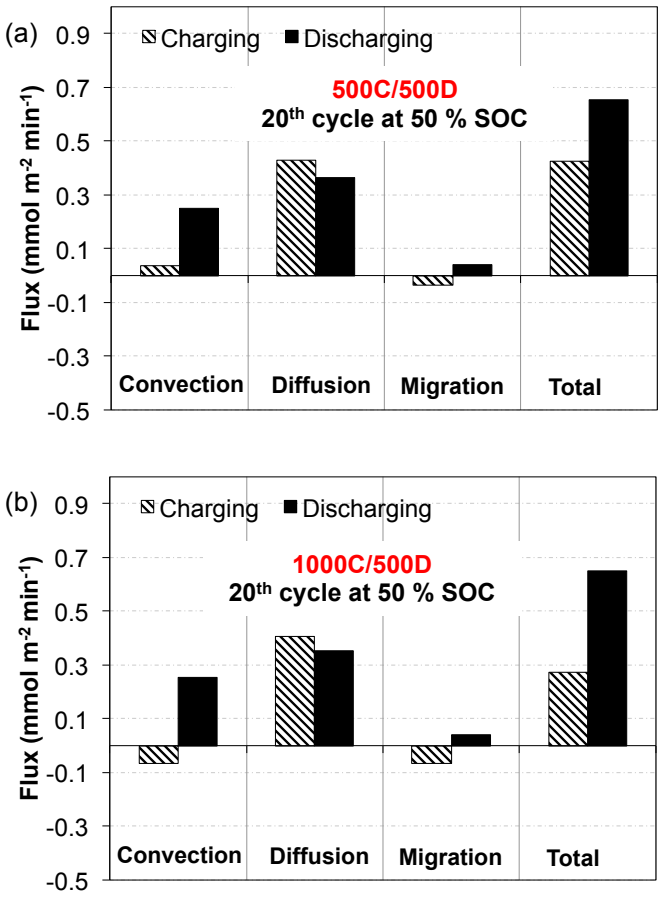

Figure 5.11 Crossover flux of V^{2+} ions due to diffusion, convection, and migration (20^{th} cycle at 50% SOC) when operated at (a) 500C/500D (b) 1000C/500D for the diffusion-dominated membrane (Nafion® 117).

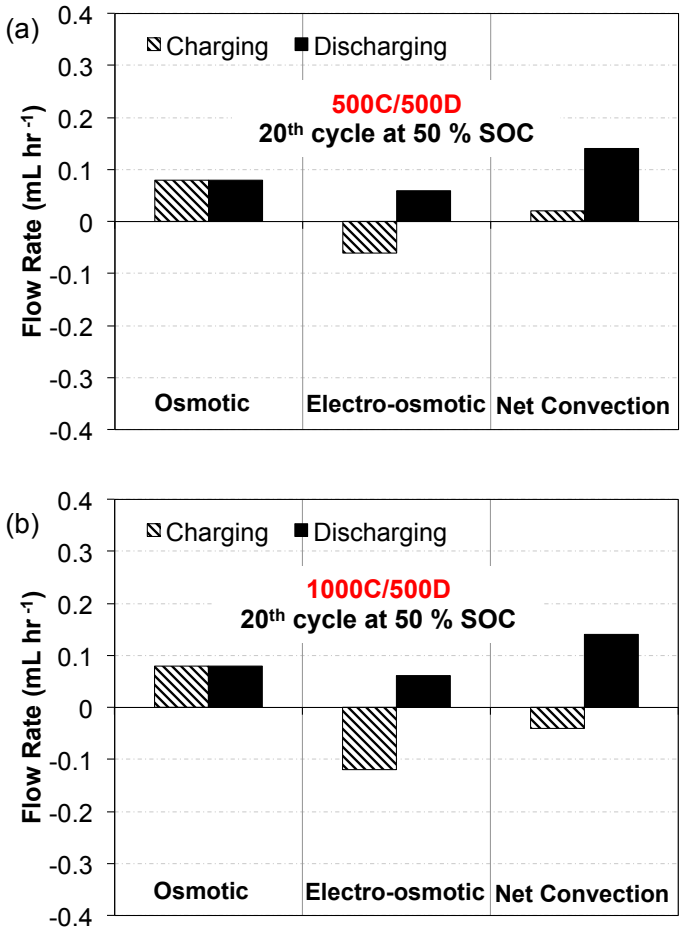

Figure 5.12 Convective crossover (osmotic, electro-osmotic, and total) of bulk electrolytes (20th cycle at 50% SOC) when operated at (a) 500C/500D (b) 1000C/500D for the diffusion-dominated membrane (Nafion® 117).

5.2.3.5 Comparison of Convection-dominated vs. Diffusion-dominated Membrane

When both membranes are compared, simulation results indicate that operating under asymmetric current conditions can mitigate capacity fade in VRFBs regardless of the membrane type. For both membranes, increasing the charging current density appears to help reduce the net convective crossover of ions, which diminishes the loss of capacity. However, when the magnitude of the reduction in capacity loss is compared, a more significant reduction in capacity fade is observed for the diffusion-dominated membrane (~12.4 %, see Fig. 5.10), as compared to the convection-dominated

membrane (~7.1 %, see Fig. 5.4). This observed discrepancy can be attributed to the reduction in the overall cycle time under asymmetric current operation. For Nafion® 117, the impact of diffusion (i.e., the dominant transport mechanism) is essentially suppressed due to a reduction in the overall cycle time. Increasing the charging current density from 500 A m^{-2} to 1000 A m^{-2} decreased the cycle time by ~33%. Since the concentration gradients for all vanadium species remain relatively constant over 40 cycles, a reduced cycle time translates to a decrease in the crossover of vanadium ions due to diffusion. The convection-dominated membrane, on the other hand, was found to be less sensitive to cycle time since the contribution of diffusion to the overall crossover is relatively smaller. For this type of membrane, the total convective flux (i.e., dominant transport mechanism) depends on other factors besides time (such as, pressure difference across the membrane, current density, etc), which makes it less sensitive to the changes in cycle time.

5.2.4 Conclusions

In this study, asymmetric current operation (i.e., different current during charging and discharging) was investigated as a technique for mitigating the capacity fade of a VRFB for both convection-dominated and diffusion-dominated membranes. For both types of membranes, it was found that increasing the charging current density decreases the net convective crossover of the bulk electrolyte, which leads to a reduction in the overall crossover at the end of the cycle. This observation was attributed to the fact that increasing the charging current increases the magnitude of the electro-osmotic convection during charging, which in turn, compensates for the convective crossover due to osmosis. Furthermore, when both membranes are compared, a more significant improvement in capacity retention was observed for the

diffusion-dominated membrane because of the fact that diffusion has less time to affect the capacity during a single cycle as a result of increased charging current. On the other hand, convection-dominated membrane was found to be less affected by similar changes in cycle time, since the impact of diffusion is very small as compared to the convection. While the simulation results indicate that asymmetric current operation offers an opportunity to increase the life span of a VRFB regardless of membrane type, it comes at the expense of reduction in the voltage efficiencies due to the increased ohmic losses.

Along with the results of previous section of this chapter, the findings of this study highlight the importance of intelligently selection of operating conditions on reducing the capacity fade of VRFBs. An optimal solution to capacity fade will probably result when operating conditions are matched to the crossover behavior of the membrane. Developing such operational strategies will compliment advances in membrane development for these systems.

Chapter 6. Conclusions and Future Work

6.1 Conclusions

The overall objective of this Ph.D. study is to establish a fundamental understanding of multi-ionic transport mechanism through VRFB membrane, and utilize this understanding to reveal the role of membrane properties and operating conditions on the capacity loss. To achieve these goals, a combined experimental and computational study was designed. An experimentally validated, 2-D, transient VRFB model that can predict the species crossover and related capacity loss was developed. In addition to that, several experimental studies were conducted to characterize different membrane types and study the effects of various operating conditions on long-term performance of the VRFB. Two fundamental conclusions derived from this study are as follows:

- Each of these three species transport mechanisms has important implications on the species crossover in VRFB membranes. Depending on the chemical structure of the membrane and operating conditions, they do make different contribution to the crossover and resulting capacity fade.
- In addition to tailoring the membrane properties, this study shows that one potential approach to reduce the crossover during VRFB operation is altering the operating conditions (e.g., flow type, flow rate) based on the membrane properties. The idea behind this approach is that by adjusting the operating conditions, it is possible to minimize the driving forces that are responsible for species crossover in the membrane.

In addition to these, following important conclusions were obtained from this dissertation study.

6.1.1 Role of Membrane Properties on Capacity Loss of a VRFB

6.1.1.1 Membrane Type

6.1.1.1.1 Proton Exchange Membranes (PEMs)

- The relative contribution of diffusion, migration, osmotic and electro-osmotic convection to the net vanadium crossover in Nafion® and sulfonated Radel (s-Radel) membranes was distinguished using the developed model.
- Model simulations indicate that diffusion is the dominant mode of vanadium transport in Nafion®, whereas convection dominates the vanadium transport through s-Radel due to the lower vanadium permeability, and thus diffusivity of s-Radel.
- Among the convective transport modes, electro-osmotic convection (i.e., electro-osmotic drag) was found to govern the species crossover in s-Radel due to its higher fixed acid concentration and corresponding free ions in the membrane.
- Simulations also showed that vanadium crossover in s-Radel changes direction during charge and discharge due to the change in the direction of electro-osmotic convection. This reversal in the direction of crossover during charge and discharge was found to result in significantly lower "net" crossover for s-Radel when compared to Nafion®

6.1.1.1.2 Anion Exchange Membranes (AEMs)

- A quaternary ammonium functionalized poly(fluorenyl ether) anion exchange membrane (AEM) with extremely low VO^{2+} permeation was characterized for VRFB applications.

- 100% coulombic efficiency (CE) was observed for the VRFB assembled with this AEM at all the current densities tested. Comparatively, the CE of the VRFB assembled with N212 was lower than 94% and varied with charge/discharge current density.
- At current densities lower than 60 mA cm^{-2}, the energy effiency of the VRFB assembled with the AEM was higher than that of the VRFB assembled with N212.
- The cycling performance demonstrated that the VRFB assembled with an AEM was free of capacity fade, which is a consequence of its low VO^{2+} permeability and is related to its 100% CE performance in an operating device.
- Increasing the IEC of the QA-Radel membranes increased both the ionic conductivity and VO^{2+} permeability.
- Increasing the polymer IEC resulted in higher voltage efficiency for the 2.0 and 2.4 mequiv. g^{-1} samples, but the cells with these membranes displayed reduced coulombic efficiency and faster capacity fade.
- The QA-Radel with an IEC of 2.0 mequiv. g^{-1} had the best balance of ionic conductivity and VO^{2+} permeability, achieving a maximum power density of 218 mW cm^{-2} which was higher than the maximum power density of a VRFB assembled with a Nafion® N212 membrane.

6.1.1.1 Membrane Thickness

- IEC-optimized SFPAE membranes with three different thicknesses (28 μm, 45 μm and 80 μm) were prepared and tested experimentally.
- It was found that the combined effects of the ohmic loss and electrolyte crossover loss in the VRFB, which were governed by membrane thickness,

resulted in an optimal membrane thickness of 45 μm for SFPAE under the conditions tested.

- Thicker membranes were observed to cause higher cell resistance while thinner membranes yielded larger vanadium crossover flux, both of which had negative impacts on the cell performance.
- The maximum power densities of the VRFBs assembled with 28 μm, 45 μm and 80 μm SFPAE membranes were 267 mW cm^{-2}, 311 mW cm^{-2} and 253 mW cm^{-2} respectively, much higher than that of the VRFB assembled with N212 membrane, which was 204 mW cm^{-2}.

6.1.2 Effects of Operating Conditions on Capacity Loss of a VRFB

6.1.2.1 Controlling Electrolyte Flow Rate

- The VRFB model was utilized to simulate several extended charge/discharge cycles with varying flow rates and electrolyte viscosities.
- The simulations indicated that osmotic and electro-osmotic convection in the membrane are major mechanisms contributing to species crossover.
- In addition, variations in electrolyte viscosity were observed to have a significant impact on the direction and magnitude of species crossover during VRFB operation.
- The simulations suggested that one potential approach to minimize the capacity loss in VRFBs would be to operate the system at constant pressure condition through the utilization of asymmetric flow rates (i.e. different flow rates in the positive and negative half-cells) to reduce the impact of osmotic convection.

6.1.2.2 Controlling Charge/Discharge Current

- The operation of a VRFB under asymmetric current conditions (i.e., different current densities during charge and discharge) was investigated as a technique to reduce the capacity loss in VRFBs.
- Two different membrane types with different modes of vanadium transport (a convection-dominated membrane and a diffusion-dominated membrane) were analyzed. In these analyses, the charging current density was varied while the discharging current was held constant.
- For both types of membranes, it was found that increasing the charging current decreases the net convective crossover of vanadium ions, which reduces the capacity loss of the battery.
- When the tested membranes are compared, the improvement in capacity retention was found to be larger for the diffusion-dominated membrane (12.4%) as compared to the convection-dominated membrane (7.1%) under asymmetric charge and discharge current.
- The higher capacity retention in the diffusion-dominated membrane was attributed to the reduction in the cycling time (and hence, suppressed contribution of diffusion) due to the increased charging current.
- While the asymmetric current operation is found to help reduce the capacity loss for both membrane types, it comes at the expense of reduction in the voltage efficiencies.

6.2 Recommendations for Future Work

Although a descriptive theoretical framework for multi-ionic species transport mechanisms through the membrane governing crossover and capacity loss has been developed, there are several phenomena still need to be understood in order to provide new strategies for mitigating the capacity loss of a VRFB. As a continuation of the present study, the following recommendation outlined below can be considered as the extension of this thesis work.

The observed trends indicated that hydraulic and electro-kinetic permeability of a membrane are equally as important as vanadium diffusion coefficients when evaluating new membranes. Currently, there is no measured data in the literature regarding these two parameters. For this reason, hydraulic and electro-kinetic permeability of several commercially available membranes (i.e., Nafion®, s-Radel… etc.) as a function of ion exchange capacity should be quantified experimentally. Then the results of this study can be incorporated into the formulated model as input parameters to develop a selectivity analysis that investigates which type of permeability property of the membrane contributes more to the crossover and related capacity fade. This work can enable us to obtain a broad range of data to accurately benchmark the design parameters of the VRFB membrane.

Furthermore, although experimental results indicated that AEM-based VRFB achieved 100 % coulombic efficiency, the effects of membrane properties on cell performance in terms of voltage efficiency for this type of membrane are not clear. Motivated by this, the current model formulation can be modified for AEMs in order

to determine the target membrane properties that yield desired voltage efficiency and free of capacity fade.

In terms of design, identification of optimized electrodes for VRFBs is more complicated than simply measuring or tuning certain properties, such as electrochemical activity or surface area. It also requires a systematic understanding of electrolyte flow mechanism and related transport losses due to the flow-assisted nature of these systems. This issue is further complicated by the variation of flow regimes that are employed in these systems. To date, two different flow configurations, namely flow-through and flow-by are commonly used. While one configuration might minimize a certain loss, it may increase other losses. For this reason, the effects of electrolyte flow type on system performance should be investigated in detail. Although the current model is formulated for flow-through configuration, it can be modified to the flow-by system to account for the effects of electrolyte flow type on the single-cycle and long-term performance of the VRFBs.

List of References

[1] Nguyen, T. V., Savinell, R. F., 2010, “Flow batteries,” Electrochemical Society Interface, 19 (3), pp. 54-56.

[2] Bartolozzi, M., 1989, “Development of redox flow batteries. A historical bibliography,” Journal of Power Sources, 27, pp. 219-234.

[3] Sum, E., Skyllas-Kazacos, M., 1985, “ A study of the V(II)/V(III) redox couple for redox flow cell applications,” Journal of Power Sources, 15, pp. 179-190.

[4] Sum, E., Rychcik, M., Skyllas-Kazacos, M., 1985, “Investigation of the V(IV)/V(V) system for use in the positive half-cell of a redox battery,” Journal of Power Sources, 16, pp. 85-95.

[5] Skyllas-Kazacos, M., Grossmith, F., 1987, “Efficiet vanadium redox flow cell,” Journal of Electrochemical Society, 134(12), pp. 2950-2953.

[6] Rychcik, M., Skyllas-Kazacos, M., 1988, “Characteristics of a new all-vanadium redox flow battery,” Journal of Power Sources, 22, pp. 59-67.

[7] Skyllas-Kazacos, M., Kasherman, D., Hong, D. R., Kazacos, M., 1991, “Characteristics and performance of 1kW UNSW vanadium redox battery,” Journal of Power Sources, 35, pp. 399-404.

[8] Kim, S., Yang, J., Schwenzer, B., Zhang, J., Li, L., Liu, J., Yang, Z., and Hickner, M., 2010, “Cycling performance and efficiency of sulfonated poly(sulfone) membranes in vanadium redox flow batteries,” Electrochemistry Communications, 12, pp. 1650-1653.

[9] Skyllas-Kazacos, M., 2009, "Secondary batteries: vanadium redox flow batteries," Encyclopedia of Electrochemical Power Sources, 2, pp. 444-453.

[10] Sun, C., Chen, J., Zhang, H., Han, X. Luo, Q., 2010, "Investigations on transfer of water and vanadium ions across Nafion membrane in an operating vanadium redox flow battery," Journal of Power Sources, 195, pp. 890-897.

[11] Ponce de Leon, C., Frias-Ferrer, A., Gonzalez-Garcia, J., Szanto, D., Walsh, F., 2006, "Redox flow cells for energy conversion," Journal of Power Sources, 189, pp. 1212-1219.

[12] Divya, K., Ostergaard, J., 2009, "Battery energy storage technology for power systems - an overview," Electric Power Systems Research, 79, pp. 511-520.

[13] Ibrahim, H., Ilinca, A., Perron, J., 2008, "Energy storage systems - characteristics and comparison," Renewable and Sustainable Energy Reviews, 12, pp. 1221-1250.

[14] Samms, S. R., Wasmus, S., Savinell, R. F., 1996, "Thermal stability of Nafion® in simulated fuel cell environments," Journal of Elelctrochemical Society, 143 (5), pp. 1498-1504.

[15] Hickner, M. A., Pivovar, B. S., 2005, "The chemical and structural nature of proton exchange membrane fuel cell properties," Fuel Cells, 5(2), pp. 213-228.

[16] Chen, D., Wang, S., Xiao, M., Meng, Y., 2010, "Preparation and properties of sulfonated poly(fluorenyl ether ketone) membrane for vanadium redox flow battery application," Journal of Power Sources, 195, pp. 2089-2095.

[17] Qiu, J., Zhai, M., Chen, J., Wang, Y., Peng, J., Xu, L., Li, J., Wei, G., 2009, "Performance of vanadium redox flow battery with a novel amphoteric ion exchange membrane synthesized by two-step grafting method," Journal of Membrane Science, 342, pp. 215-220.

[18] Qiu, J., Zhao, L., Zhai, M., Ni, J., Zhou, H., Peng, J., Li, J., Wei, G., 2008, "Pre-irradiation grafting of styrene and maleic anhydride onto PVDF membrane and subsequent sulfonation for application in vanadium redox batteries," Journal of Power Sources, 177, pp. 617-623.

[19] Jia, C., Liu, J., Yan, C., "A significantly improved membrane for vanadium redox flow battery," Journal of Power Sources, 195, pp. 4380-4383.

[20] Teng, X., Zhao, Y., Xi, J., Wu, Z., Qiu, X., Chen, L., 2009, "Nafion/organic silica modified TiO_2 composite membrane for vanadium redox flow battery via in situ sol-gel reactions," Journal of Membrane Science, 341, pp. 149-154.

[21] Luo, Q., Zhang, H., Chen, J., Qian, P., Zhai, Y., 2008, "Modification of Nafion membrane using interfacial polymerization for vanadium redox flow battery applications," Journal of Membrane Science, 311, pp. 98-103.

[22] S. Eckroad, Technical Report, EPRI-1014836, Electric Power Research Institute, Palo Alto, CA, USA, 2007.

[23] Kim, S., Tighe, T., Schwenzer, B., Yan, J., Zhang, J., Liu, J., Yang, Z., Hickner, M. A., 2011, "Chemical and mechanical degradation of sulfonated poly(sulfone) membranes in vanadium redox flow batteries," Journal of Applied Electrochemistry, 41, pp. 1201- 1213.

[24] You, D., Zhang, H., Sun, C., Ma, X., 2011, "Simulation of the self-discharge process in vanadium redox flow battery," Journal of Power Sources, 196, pp. 1578-1585.

[25] Li, M., Hikihara, T., 2008, "A coupled dynamic model of redox flow battery based on chemical reaction, fluid flow, and electrical circuit," IEICE Transections on Fundamentals of Electronics, Communications and Computer Science, E91-A, pp. 1741-1747.

[26] Shah, A., Watt-Smith, M., Walsh, F., 2008, "A dynamic performance model for redox-flow batteries involving soluble species," Electrochimica Acta, 53, pp. 8087-8100.

[27] Al-Fetlawi, H., Shah, A., Walsh, F., 2009, "Non-isothermal modeling of the all-vanadium redox flow battery," Electrochimica Acta, 55, pp. 78-89.

[28] Shah, A., Al-Fetlawi, H., Walsh, F., 2010, "Dynamic modeling of hydrogen evolution effects in the all-vanadium redox flow battery," Electrochimica Acta, 55, pp. 1125-1139.

[29] Al-Fetlawi, H., Shah, A., Walsh, F., 2010, "Modeling the effects of oxygen evolution in the all-vanadium redox flow battery," Electrochimica Acta, 55, pp. 3192-3205.

[30] You, D., Zhang, H., Chen, J., 2009, "A simple model for the vanadium redox battery," Electrochimica Acta, 54, pp. 6827-6836.

[31] Shah, A., Tangirala, R., Singh, R., Wills, R., Walsh, F., 2011, "A dynamic unit cell model for the all-vanadium flow battery," Journal of Electrochemical Society, 158, pp. A671-A677.

[32] Vynnycky, M., 2011, "Analysis of a model for the operation of a vanadium redox battery," Energy, 36, pp. 2242-2256.

[33] Ma, X., Zhang, H., Xing, F., 2011, "A three-dimensional model for negative half cell of the vanadium redox flow battery," Electrochimica Acta, 58, pp. 238-246.

[34] Tang, A, Ting, S., Bao, J., Skyllas-Kazacos, B., 2012, "Thermal modeling and simulation of the all-vanadium redox flow battery," Journal of Power Sources, 203, pp. 165-176.

[35] Skyllas-Kazacos, M., Goh, L., 2012, "Modeling of vanadium ion diffusion across the ion exchange membrane in the vanadium redox battery," 399, pp. 43-48.

[36] Yang, Z., Zhang, J., Kintner-Meyer, M., Lu, X., Choi, D., Lemmon, J. P., Liu, J., 2011, "Electrochemical energy storage for green grid," Chemical Reviews, 111, pp. 3577.

[37] Weber, A., Mench, M. M., Meyers, J., Ross, P. N., Gostick, J. T., Liu, Q., 2011, "Redox flow batteries: a review," Journal of Applied Electrochemistry, 41, pp. 1137-1164.

[38] Knehr, K. W., Kumbur, E. C., 2011, "Open circuit voltage of vanadium redox flow batteries: discrepancy between models and experiments," Electrochemistry Communications, 13, pp. 342-345.

[39] Kontturi, K., Murtomaki, L., Manzanares, J. A., 2008, "Ionic Transport Processes in Electrochemistry and Membrane Science, Oxford University Press, New York.

[40] Knopf, D. A., Luo, B. P., Krieger, U. K., Koop, T., 2003, "Thermodynamic dissociation constant of the bisulfate ion from raman and ion interaction modeling studies of aqueous sulfuric acid at low temperatures," Journal of Physical Chemistry A, 107, pp. 4322-4332.

[41] Verbrugge, M. W., Hill, R. F., 1990, "Ion and solvent transport in ion-exchange membranes I. A macrohomogeneous mathematical model," Journal of Electrochemical Society**,** 137 (3) pp. 886-893.

[42] Xu, P., Yu, B., 2008, "Developing a new form of permeability and Kozeny-Carman constant for homogenous porous media by means of fractal geometry," Advances in Water Resources, 31, pp. 74-81.

[43] Blanc, C., 2009, "Modeling of a vanadium redox flow battery electricity storage system," PhD thesis, EPFL, Switzerland.

[44] Orji, G, Katayama, Y., Miura, T., 2004, "Investigation on V(IV)/V(V) species in a vanadium redox flow battery," Electrochimica Acta, 49 (19), pp. 3091-3095.

[45] Munson, B., Young, D., Okiishi, T., Huebsch, W., 2009, "Fundamentals of Fluid Mechanics,"6th ed., John Wiley & Sons, Inc., Hoboken, New Jersey.

[46] Yamamura, T., Watanabe, N., Yano, T., Shiokawa, Y., 2005, "Electron-transfer kinetics of Np^{3+}/Np^{4+}, NpO_2^{+}/NpO_2^{2+}. V^{2+}/V^{3+}, and VO^{2+}/VO_2^{+} at carbon electrodes," Journal of Electrochemical Society, 152 (4), pp. A830-A836.

[47] Pourcelly, G., Lindheimer, A., Gavach, C., Hurwitz, H. D., 1991, " Electrical transport of sulphuric acid in nation perfluorosulphonic membranes," Journal of Electroanalytical Chemistry, 305 (1), pp. 97-113.

[48] Newman, T., Thomas-Alyea, K. E., 2004, "Electrochemical Systems," 3rd ed., John Wiley & Sons, Inc., Hoboken, New Jersey.

[49] DuPont. website: http://www2.dupont.com/FuelCells/en_US/products/literature.html (accessed 21-6-2011).

[50] Bernardi, D., Verbrugge, M., 1991, "Mathematical model of a gas diffusion electrode bonded to a polymer electrolyte," AIChE Journal, 37 (8), pp. 1151-1163.

[51] Xi, J., Wu, Z., Teng, X., Zhao, Y., Chen, L., Qiu, X., 2008, "Self-assembled polyelectrolyte multilayer modified Nafion membrane with suppressed vanadium ion crossover for vanadium redox flow batteries," Journal of Materials Chemistry, 18, pp. 1232-1238.

[52] Verbrugge, M. W., Hill, R. F., 1990, "Ion and solvent transport in ion-exchange membranes II. A radiotracer study of the sulfuric-acid, nafion-117 system," Journal of Electrochemical Society**,** 137 (3) pp. 893-899.

[53] Vafai, K., Tien, C., 1981, "Boundary and intertia effects on flow and heat transfer in porous media," International Journal of Heat and Mass Transfer, 24, pp. 195-203.

[54] Zhong, S., Padeste, C., Kazacos, M., Skyllas-Kazacos, M., 1993, "Comparison of the physical, chemical and electrochemical properties of rayon- and polyacrylonitrile-based graphite gelt electrodes," Journal of Power Sources, 46, pp. 29-41.

[55] Hwang, G-J., Ohya, H., 1996, “Preparation of cation exchange membrane as a separator for the all-vanadium redox flow battery,” Journal of Membrane Science, 120, pp. 55-67.

[56] Qiu, G., Joshi, A., Dennison, C. R., Knehr, K. W., Kumbur, E. C., Sun, Y., 2012, “3-D pore-scale resolved model for coupled species/charge/fluid transport in a vanadium redox flow battery,” Electrochimca Acta, 64, pp. 46-64.

[57] Wargo, E. A., Hanna, A. C., Cecen, A., Kalidindi, S. R., Kumbur E. C., 2012, “Selection of representative volume elements for pore scale analysis of transport in fuel cell materials,” Journal of Power Sources, 197, pp. 168-179.

[58] Cecen, A., Wargo, E. A., Hanna, A. C., Kalidindi, S. R., Kumbur, E. C., 2012, “3-D microstructure analysis of fuel cell materials: spatial distributions of tortuosity, void size and diffusivity,” Journal of Electrochemical Society, 159 (3), pp. B299-B307.

[59] Hamann, C., Hamnett, A., Vielstich, W., 2007, “Electrochemistry,” 2nd ed., Wiley-VCH, Germany.

[60] Wei, W., Zhang, H., Li, X., Mai, Z., Zhang, H., 2012, “Poly(tetrafluoroethylene) reinforced sulfonated poly(ether ether ketone) membranes for vanadium redox flow battery application,” Journal of Power Sources, 208, pp. 421-425.

[61] Luo, X., Lu, Z., Xi, J., Wu, Z., Zhu, W., Chen, L., Qiu, X., 2005, “Influences of permeation of vanadium ions through PVDF-g-PSSA membranes on performances of vanadium redox flow batteries,” Journal of Physical Chemistry B, 109, pp. 20310-20314.

[62] Chen, D., Hickner, M. A., Agar, E., Kumbur, E. C., 2013, "Selective anion exchange membranes for high coulombic efficiency vanadium redox flow batteries," Electrochemistry Communications, 26, pp 37-40.

[63] Xing, D., Zhang, S., Yin, C., Zhang, B., Jian, X., 2010, “Effect of amination agent on the properties of quaternized poly(phthalazinone ether sulfone) anion exchange membrane for vanadium redox flow battery application,” Journal of Membrane Science, 354, pp. 68-73.

[64] Zhang, F., Zhang, H., Qu, C., 2012, “Influence of solvent on polymer prequaternization toward anion-conductive membrane fabrication for all-vanadium flow battery,” Journal of Physical Chemistry B, 116, pp. 9016-9022.

[65] Zhang, H., Zhang, H., Li, X., Mai, Z., Wei, W., 2012, “Silica modified nanofiltration membranes with improved selectivity for redox flow battery application,” Energy & Enviromental Science, 5, pp. 6299-6303.

[66] Ma, J., Wang, Y., Peng, J., Qiu, J., Xu, L., Li, J., Zhai, M., 2012, “Designing a new process to prepare amphoteric ion exchange membrane with well-distributed grafted chains for vanadium redox flow battery,” Journal of Membrane Science, 419-420, pp. 1-8.

[67] Sasikumar, G., Ihm, J. W., Ryu, H., 2004, Optimum Nafion content in PEM fuel cell elelctrodes," Electrochimica Acta, 50, pp.601-605.

[68] Schwenzer, B., Zhang, J., Kim, S., Li, L., Liu, J., Yang, Z., 2011, "Membrane development for vanadium redox flow batteries," ChemSusChem, 4, pp.1388-1406.

[69] Kim, S., Tighe, T., Schwenzer, B., Yan, J., Zhang, J., Liu, J., Yang, Z., Hickner, M. A., 2011, "Chemical and mechanical degradation of sulfonated poly(sulfone) membranes in vanadium redox flow batteries," Journal of Applied Electrochemistry, 41, pp. 1201-1213.

[70] Chen, Y. L., Meng, Y. Z., Hay, A. S., 2005, "Novel synthesis of sulfonated poly(phthalazinone ether ketone) used as a proton exchange membrane via N-C coupling reaction," Macromolecules 38, pp. 3564-3566.

[71] Matsumura, S., Hill, A. R., Lepiller, C., Gaudet, J., Guay, D., Shi, Z. Q., Holdcroft, S., Hay, A. S., 2008, "Ionomers for proton exchange membrane fuel cells with sulfonic acid groups on the end groups: novel branched poly(ether–ketone)s," Macromolecules, 41, pp. 281-284.

[72] Shang, X., Tian, S., Kong, L., Meng, Y., 2005, "Synthesis and characterization of sulfonated fluorene-containing poly(arylene ether ketone) for proton exchange membrane," Journal of Membrane Science, 266, pp. 94-101.

[73] Miyatake, K., Chikashige, Y., Higuchi, E., Wantanabe, M., 2007, "Tuned polymer electrolyte membranes based on aromatic polyethers for fuel cell applications," Journal of American Chemical Society, 129 (13), pp. 3879-3887.

[74] Asano, N., Aoki, M., Suzuki, S., Miyatake, K., Uchida, H., Wantanabe, M., 2006, "Aliphatic/aromatic polymide ionomers as a proton conductive membrane for fuel cell applications," Journal of American Chemical Society, 128, pp. 1762-1769.

[75] Schuster, M., Kreuer, K. D., Andersen, H. T., Maier, J., 2007, "Sulfonated poly(phenylene sulfone) polymers as hydrolytically and thermooxidatively stable proton conducting ionomers," Macromolecules, 40, pp. 598-607.

[76] Bae, B, Miyatake, K., Wantanabe, M., 2008, "Sulfonated poly(arylene ether sulfone) ionomers containing fluorenyl groups for fuel cell applications," Journal of Membrane Science, 310, pp. 110-118.

[77] Chen, D., Kim, S., Li, L., Yang, G., Hickner, M. A., 2012, "Stable fluorinated sulfonated poly(arylene ether) membranes for vanadium redox flow batteries," RSC Advances, 2, pp. 8087-8094.

[78] Knehr, K. W. and Kumbur, E.C., 2012, "Role of convection and related effects on species crossover and capacity loss in vanadium flow batteries," Electrochemistry Communications, 23, pp 76-79.

[79] Sata, T., 2001, "Studies on anion exchange membranes having permselective for specific anions in electrodialysis – effect of hydrophilicity of anion exchange membranes on permselectivity of anions," Journal of Membrane Science,167, pp. 1-31.

[80] Zhang, S., Yin, C., Xing, D., Yang, D., Jian, X., 2010, "Preparation of chloromethylated/quaternized poly(phthalazinone ether ketone) anion exchange membrane materials for vanadium redox flow battery applications," Journal of Membrane Science, 363, pp. 243-249.

[81] Fang, J., Xu, H., Wei, X., Guo, M., Lu, X., Lan, C., Zhang, Y., Liu, Y., Peng, T., 2012, "Preparation and characterization of quaternized poly (2,2,2-trifluoroethyl methacrylate-co-N-vinylimidazole) membrane for vanadium redox flow battery," Polymers for Advanced Technologies, 24, pp. 168-173.

[82] Chen, D., Hickner, M. A., Wang, S., Pan, J., Xiao, M., Meng, Y., 2012, "Synthesis and characterization of quaternary ammonium functionalized fluorene-containing cardo polymers for potential anion exchange membrane water electrolyzer applications," International Journal of Hydrogen Energy, 37 (21), pp. 16168-16176.

[83] Fujimoto, C. H., Hickner, M. A., Cornelius, C. J., Loy, D. A., 2005, "Investigation of domain size in polymer membranes using double-quantum-filtered spin diffusion magic angle spinning NMR," Macromolecules, 38, pp. 1201-1206.

[84] Knehr, K. W., Agar, E., Dennison, C. R., Kalidindi, A. R., and Kumbur, E. C., 2012, "A transient vanadium flow battery model incorporating species crossover and water transport in the membrane Journal of Electrochemical Society, 159, (9) pp. A1446-A1459.

[85] Suarez, S. N., Jayakody, J. R. P., Greenbaum, S. G., Zawodzinski, T., Fontanella, J. J., 2010, "A fundamental study oft he transport properties of aqueous superacid solutions, " Journal of Physical Chemistry B, 114, pp. 8941-8947.

[86] Tang, Z., Keith, R., Aaron, D. S., Lawton, J. S., Papandrew, A. P., Zawodzinski, T. A., 2012, "Proton exchange membrane performance characterization in VRFB," ESC Transactions 41 (23), pp. 25-34.

[87] Teng, X., Zhao, Y., Xi, J., Wu, Z., Qiu, X., Chen, L., 2009, "Nafion/organically modified silicate hybrids membrane for vanadium redox flow battery," Journal of Power Sources, 189, pp. 1240-1246.

[88] Liu, H., Xu, Q., Yan, C., Qiao, Y., 2011, "Corrosion behavior of a positive graphite electrode in vanadium redox flow battery," Electrochimica Acta 56, pp. 8783-8790.

[89] Zhang, H., Zhang, H., Zhang, F., Li, X., Li, Y., Vankelecom, I., 2013, "Advanced charged membranes with highly symmetric spongy structures for vanadium flow battery application," Energy & Environmental Science, 6, 776-781.

[90] Seo, S., Kim, B., Sung, K., Shim, J., Jeon, J., Shin, K., Shin, S., Yun, S., Lee, J., Moon, S., 2013, "Electrochemical properties of pore-filled anion exchange membranes and their ionic transport phenomena for vanadium redox flow battery applications," Journal of Membrane Science, 428, pp. 17-23.

[91] Geise, G. M., Falcon, L. P., Freeman, B. D., Paul, D. R., 2012, "Sodium chloride sorption in sulfonated polymers for membrane applications," Journal of Membrane Science, 423-424, pp. 195-208.

[92] Hu, G., Wang, Y., Ma, J., Qiu, J., Peng, J., Li, J., Zhai, M., 2012, "A novel amphoteric ion exchange membrane synthesized by radiation-induced grafting α-methylstyrene and N,N-dimethylaminoethyl methacrylate for vanadium redox flow battery application, Journal of Membrane Science, 407-408, pp. 184-192.

[93] Chen, D., Hickner, M. A., Agar, E., and Kumbur, E. C., 2013, "Optimizing membrane thickness for vanadium flow batteries," Journal of Membrane Science, 437, pp 108-113.

[94] Chen, D., Wang, S., Xiao, M., Han, D., Meng, Y., 2010, "Preparation and properties of sulfonated poly(fluorenyl ether ketone) membrane for vanadium redox flow battery application," Journal of Power Sources, 195, pp. 7701-7708.

[95] Mai, Z., Zhang, H., Zhang, H., Xu, W., Wei, W., Na, H., Li, X., 2013, "Anion-conductive membranes with ultralow vanadium permeability and excellent performance in vanadium flow batteries," ChemSusChem, 6, pp. 328-335.

[96] Mai, Z., Zhang, H., Li, X., Xiao, S., Zhang, H., 2011, "Nafion/polyvinylidene fluoride blend membranes with improved ion selectivity for vanadium redox flow battery application," Journal of Power Sources 196, pp. 5737-5741.

[97] Fujimoto, C., Kim, S., Stains, R., Wei, X., Li, L., Yang, Z. G., 2012, "Vanadium redox flow battery efficiency and durability studies of sulfonated Diels-Alder poly(phenylene)s," Electrochemical Communications, 20, pp. 48-51.

[98] Luo, Q., Zhang, H., Chen, J., You, D., Sun, C., Zhang, Y., 2008, "Preparation and characterization of Nafion/SPEEK layered composite membrane and its application in vanadium redox flow battery Journal of Membrane Science, 325 (2), pp. 553-558.

[99] Agar, E., Knehr, K. W., Chen, D., Hickner, M. A., Kumbur, E. C., 2013, "Species transport mechanisms governing capacity loss in vanadium flow batteries: comparing Nafion® and sulfonated radel membranes," Electrochimica Acta, 98, pp. 66-74

[100] Agar, E., Knehr, K. W., Dennison, C. R., and Kumbur, E. C., 2013, "Identification of Performance Limiting Electrode using Asymmetric Cell Configuration in Vanadium Redox Flow Batteries," Journal of Power Sources, 225, pp 89-94.

[101] Aaron, D., Tang, Z., Papandrew, A. B., Zawodzinski, T. A., 2011, "Polarization curve analysis of all-vanadium redox flow batteries," Journal of Applied Electrochemistry, 41, pp. 1175-1182.

[102] Aaron, D., Liu, Q., Tang, Z., Grim, G. M., Papandrew, A. B., Turhan, A., Zawodzinski, T. A., Mench, M. M., 2012, "Dramatic performance gains in vanadium redox flow batteries through modified cell architecture," Journal of Power Sources, 206, pp. 450-453.

APPENDIX A. Nomenclature

Variables

a	specific surface area ($m^2\,m^{-3}$)
c	concentration (mol m^{-3})
C_{KC}	Kozeny-Carmen constant
d_f	fiber diameter (μm)
D	diffusion coefficient
E_0	open circuit voltage
E_0'	standard reduction potential
E	voltage (V)
F	Faraday's Constant
h	height
i	reaction current density
I	current
$\vec{j}$	current density
k	reaction rate/coefficient
K_ϕ	interfacial coefficient
L	component thickness (m)
M	molecular weight (g mol^{-1})
$\vec{n}$	outward normal vector
$\vec{N}$	flux (mol $m^{-3}\,s^{-1}$)
p	pressure
r_p	pore radius
R	universal gas constant
S	source/sink (mol $m^{-3}\,s^{-1}$)
t	time
T	temperature (K)
u	ion mobility
$\vec{v}$	velocity (m s^{-1})
V	volume (ml)
w	width
z	valence
P	permeability

Greek

α	transfer coefficient
β	degree of dissociation

δ	region thickness (m)
ε	porosity
η	overpotential (V)
κ	permeability (m^2)
μ	dynamic viscosity
ρ	density (g cm^{-3})
σ	conductivity
ϕ	potential (V)
ω	volumetric flow rate (m^3 s^{-1})

Subscripts

$-$	negative half-cell
$+$	positive half-cell
c	cation
cell	property of cell
f	fixed membrane structure
i	species: V^{2+}, V^{3+}, VO^{2+}, VO_2^+ H^+, HSO_4^-, and SO_4^{2-}
j	negative or positive half-cell (- or +, respectively)
l	liquid or ionic
s	solid or electronic
T	tank
w	water
act	activation
ohm	ohmic
trans	transport
cross	crossover
ch	charge
dis	discharge

Superscripts

0	initial condition
cc	current collector domain
e	electrode or electrolyte domain
eff	effective value
er	interfacial electrode region
in	inlet
junc	interfacial junction
m	membrane domain
mr	interfacial membrane region
out	outlet
s	surface

List of Publications

Journal Publications

1. **Agar, Ertan**, Benjamin, A., Dennison, C. R., Chen, D., Hickner, M. A., and Kumbur E. C. *Reducing Capacity Fade in Vanadium Redox Flow Batteries by Altering Charging and Discharging Currents*, Journal of Power Sources, 246, 2014, 767-774.

2. **Agar Ertan**, Knehr, K. W., Kumbur, E. C., Chen, D., and Hickner, M. A. *Species Transport Mechanisms Governing Capacity Loss in Vanadium Redox Flow Batteries: Comparing Nafion® and Sulfonated Radel Membranes,* Electrochimica Acta, 98, 2013, 66-74.

3. **Agar, Ertan**, Dennison, C. R., Knehr, K. W., and Kumbur, E. C. *Identification of Performance Limiting Electrode using Asymmetric Cell Configuration in Vanadium Redox Flow Batteries*, Journal of Power Sources, 225, 2013, 89-94.

4. Benjamin, A., **Agar, Ertan**, Dennison, C. R., and Kumbur, E. C. *On the Computation of Coulombic Efficiency for Vanadium Redox Flow Batteries: Cutoff Voltages vs. State of Charge Limits*, Electrochemistry Communications, 35, 2013, 42-44.

5. Chen, D., Hickner, M. A., **Agar, Ertan**, and Kumbur, E. C. *Optimized Anion Exchange Membranes for Vanadium Redox Flow Batteries,* ACS Applied Materials & Interfaces, 5, 2013, 7559-7566.

6. Chen, D., Hickner, M. A., **Agar, Ertan**, and Kumbur E. C. *Optimizing Membrane Thickness for Vanadium Redox Flow Batteries*, Journal of Membrane Science, 437, 2013, 108-113.

7. Chen, D., Hickner, M. A., **Agar, Ertan**, and Kumbur E. C. *Selective Anion Exchange Membrane for High Coulombic Efficiency Vanadium Redox Flow Batteries*, Electrochemistry Communications, 26, 2013, 37-40.

8. Knehr, K. W., **Agar Ertan**, Dennison, C. R., Kalidindi, A. R., and Kumbur, E. C. *A Transient Vanadium Flow Battery Model Incorporating Vanadium Crossover and Water Transport through the Membrane*, Journal of Electrochemical Society, 159, 2012, A1146-A1159.

9. Baker, D., and **Agar, Ertan**, *International Summer Engineering Program on Fuel Cells for Undergraduate Engineering Students*, International Journal of Hydrogen Energy, 36, 2011, 3712-3725.

Peer-Reviewed Conference Proceedings

1. Chen, D., Hickner, M. A., **Agar, Ertan**, and Kumbur, E. C. *Anion Exchange Membranes for Vanadium Redox Flow Batteries*, Electrochemical Society Transactions, 53 (7), 2013, 83-89.

2. **Agar, Ertan**, Dennison, C. R., Knehr, K. W., and Kumbur, E. C. *Asymmetric Performance Testing of Carbon Felt Electrodes to Identify the Limiting Electrode in Vanadium Redox Flow Batteries*, Electrochemical Society Transactions, 53 (7), 2013, 69-73.

Conference Presentations, Abstracts and Posters

1. **Agar, Ertan**, Benjamin, A., Dennison, C. R., Chen, D., Hickner, M. A., and Kumbur, E. C. *Mitigating Capacity Fade in Vanadium Redox Flow Batteries Using Asymmetric Currents During Cycling*, 224th ECS Meeting, October, 27 - November, 1, 2013 San Francisco, CA.

2. Benjamin, A., **Agar, Ertan**, Dennison, C. R., and Kumbur, E. C. *On the Determination of Coulombic Efficiency for Vanadium Redox Flow Batteries: Cutoff Voltage vs. State of Charge Limits*, 224th ECS Meeting, October, 27 - November 1, 2013, San Francisco CA.

3. **Agar, Ertan**, Knehr, K. W., Dennison, C. R., and Kumbur, E. C. *Investigation of Reaction Mechanisms in Vanadium Redox Flow Batteries via Asymmetric Performance Tests,* ASME 7th International Conference on Energy Sustainability, July, 14 – 19, 2013 Minneapolis, MN.

4. **Agar, Ertan**, Benjamin, A., Knehr, K. W., Dennison, C. R., and Kumbur, E. C. *Prediction and Mitigation of Capacity Fade in Vanadium Redox Flow Batteries*, AIChE Massive Energy Storage for Broader Use of Renewable Energy Sources, June, 23 – 26, 2013 Newport Beach, CA.

5. **Agar, Ertan**, Chen, D., Hickner, M. A., and Kumbur, E. C. *Effects of Membrane Thickness on the Performance of Vanadium Redox Flow Batteries*, 223rd ECS Meeting, May, 12 - 17, 2013 Toronto, ON.

6. Knehr, K. W., **Agar, Ertan**, Dennison, C. R., Kalidindi, A. R., and Kumbur, E. C. *Reducing Capacity Loss in Vanadium Redox Flow Batteries by Controlling Convective Transport Across the Membrane*, MRS Fall Meeting, November, 25 - 30, 2012 Boston, MA.

7. **Agar, Ertan**, Dennison, C. R., Kalidindi, A. R., Knehr, K. W., and Kumbur, E. C. *Investigation of Functionalized Electrode Performance in Vanadium Redox Flow Batteries*, MRS Fall Meeting, November, 25 - 30, 2012 Boston, MA.

8. Knehr, K. W., **Agar, Ertan**, Dennison, C. R., Kalidindi, A. R., Chen, D., Hickner, M. A., and Kumbur, E. C. *Role of Membrane Properties on Species Crossover and Capacity Loss of a Vanadium Redox Flow Battery*, 221st ECS Meeting, October, 7 - 12, 2012 Honolulu, Hawaii.

9. **Agar, Ertan**, Dennison, C. R., Kalidindi, A. R., Knehr, K. W., and Kumbur, E. C. *Reaction Kinetics of Vanadium Species on Functionalized Carbon-Felt Electrodes of Vanadium Redox Flow Batteries*, 244th ACS National Meeting and Exposition, August, 19 - 23, 2012 Philadelphia, PA.

10. Knehr, K. W., **Agar, Ertan**, Dennison, C. R., Kalidindi, A. R., and Kumbur, E. C. *Performance Modeling of Redox Flow Batteries*, 244th ACS National Meeting and Exposition, August, 19 - 23, 2012 Philadelphia, PA.

11. **Agar, Ertan**, Knehr, K. W., Kalidindi, A. R., Dennison, C. R., and Kumbur, E. C. *Multi-ionic Transport and Effects of Crossover in Vanadium Redox Flow Batteries*, 221st ECS Meeting, May, 6 - 10, 2012 Seattle, WA.

12. Knehr, K. W., **Agar, Ertan**, Kalidindi, A. R., Dennison, C. R., and Kumbur, E. C. *A Computational Model for Quantification of Species Crossover and Related Losses in Vanadium Redox Flow Batteries*, ASME 6th Conference of Energy Sustainability, July, 23 - 26, 2012 San Diego, CA.

13. Kalidindi, A. R., **Agar, Ertan**, Dennison, C. R., and Kumbur, E. C. *Investigation of Positive Electrode Kinetics for Vanadium Redox Flow Batteries*, Drexel Research Day, April, 19, 2012 Philadelphia, PA (Poster) - **Awarded Best Poster in Physical Sciences and Engineering.**

14. Kalidindi, A. R., Dennison, C. R., **Agar, Ertan**, and Kumbur, E. C. *Investigation of Electrolyte Crossover in Vanadium redox Flow Batteries*, National Conference for Undergraduate Research, March, 29 - 31, 2012 Ogden, UT (Presentation only).

15. Kalidindi, A. R., **Agar, Ertan**, Dennison, C. R., and Kumbur, E. C. *Reaction Kinetics of Vanadium Species on Carbon Felt Electrodes*, National Collegiate Research Conference, January, 19 - 21, 2012 Cambridge, MA (Poster) - **Awarded Most Interdisciplinary Poster.**

16. Dennison, C. R., Kalidindi, A. R., Biel-Gobel, J. J., Commons, W., **Agar, Ertan**, Knehr, K. W., and Kumbur, E. C. *Ionic Transport and Kinetic Processes in Vanadium Redox Flow Batteries*, The Forth International Forum on Multidisciplinary Education and Research for Energy Science, December, 17 - 21, 2011 Honolulu, Hawaii.

17. Knehr, K. W., **Agar, Ertan**, Dennison, C. R., Kalidindi, A. R., and Kumbur, E. C. *Modeling Species Crossover and Related Effects on the Performance of a Vanadium Redox Flow Battery*, The Forth International Forum on Multidisciplinary Education and Research for Energy Science, December, 17 - 21, 2011 Honolulu, Hawaii.

18. Dennison, C. R., Knehr, K. W., **Agar, Ertan**, and Kumbur E. C. *Component and Performance Analysis of Vanadium Redox Flow Batteries: Experimental and Modeling Studies*, 2011 AIChE Annual Meeting, October, 16 - 21, 2011 Minneapolis, MN.

19. **Agar, Ertan**, Knehr, K. W., and Kumbur, E. C. *Simulating Performance and Species Crossover in a Vanadium Redox Flow Battery Using COMSOL Multiphysics*, COMSOL Conference 2011, October, 13 - 15, 2011 Boston, MA.

20. **Agar, Ertan**, Knehr, K. W., Dennison, C. R., and Kumbur, E. C. *Investigation of the Performance of Vanadium Redox Flow Batteries: A Macroscopic Modeling Approach,* 220th ECS Meeting and Electrochemical Energy Summit, October, 9 - 14, 2011 Boston, MA.

21. **Agar, Ertan**, Knehr, K. W., and Kumbur, E. C. *Effects of Crossover on the Performance of a Vanadium Redox Flow Battery*, 5th International Conference on Energy Sustainability, August, 7 - 10, 2011 Washington, DC.

22. Knehr, K. W., **Agar, Ertan**, and Kumbur, E. C. *Modeling the Performance of a Vanadium Redox Flow Battery*, Research Experience for Undergraduates Poster Session, August, 11, 2011 Philadelphia, PA (Poster).

23. Knehr, K. W., **Agar, Ertan**, and Kumbur, E. C. *Modeling a Vanadium Redox Flow Battery*, Research Experience for Undergraduates Poster Session, August, 12, 2010 Philadelphia, PA (Poster).

24. Baker, D., **Agar, Ertan**, Yeralan, S. *International Summer Engineering Program at METU: A Bridge to Global Competency*, 39th ASEE/IEEE Frontiers in Education Conference, October, 18 - 21, 2009 San Antonio, TX.

Vita

Ertan Agar was born in Ankara, Turkey. He received his BS and MS degrees in Mechanical Engineering from the Middle East Technical University, Ankara, Turkey in 2007 and 2010 respectively. His research interests include electrochemical energy conversion and storage, mathematical modeling of electrochemical systems, redox flow batteries, ionic transport in membranes, electrochemical reaction kinetics, and proton exchange membrane fuel cells. His MS study focused on multiphysical performance modeling of proton exchange membrane fuel cells (PEMFCs). Through these years, he worked as a research assistant for a PEMFC project coordinated by TOBB University of Economics and Technology. In March 2010, he joined the Electrochemical Energy Systems Laboratory (ECSL) at Drexel University, Philadelphia. Since then, he has worked as a research assistant at ECSL under the supervision of Dr. Caglan Kumbur. For his Ph.D. dissertation, Ertan focused on developing a fundamental understanding of the capacity fade for vanadium redox flow batteries. He is a member of The Electrochemical Society (ECS), American Chemical Society (ACS), International Association of Hydrogen Energy (IAHE), and American Society of Mechanical Engineers (ASME).